



**UNIVERSITÀ DEGLI STUDI DI MILANO**  
**FACOLTÀ DI SCIENZE MATEMATICHE,**  
**FISICHE E NATURALI**

**Interfacial layering of ionic  
liquids on solid surfaces**

Advisor: Dr. Nicola Manini  
Co-Advisor: Prof. Pietro Ballone

Daniele Dragoni  
Matricola n° 736939  
A.A. 2009/2010

Codice PACS: 68.18.Fg



# Interfacial layering of ionic liquids on solid surfaces

Daniele Dragoni

Dipartimento di Fisica, Università degli Studi di Milano,  
Via Celoria 16, 20133 Milano, Italia

February 15, 2011

We investigate the layering properties of a few-nanometer-thick layer of a common room-temperature ionic liquid deposited on mica. We use classical molecular dynamics with a AMBER-type force field to simulate its equilibrium properties, which we analyze as a function of the distance  $z$  from the mica surface. We then simulate the experiments where a nanometer-sized atomic-force-microscope tip pushes its way into this layer, and evaluate the resulting dynamical forces acting on the tip itself. The computed forces exhibit less evident signs of layering than in experiment, except very near to the mica surface.

Advisor: *Dr. Nicola Manini*  
Co-Advisor: *Prof. Pietro Ballone*



## Contents

Chapter 1. Ionic Liquid: an Introduction	7
1.1. Lowering the melting point/Why RTIL's are liquid at room temperature?	7
1.2. The dialkymidazolium cation family and the bistriflimide anion	8
Chapter 2. The mica substrate	13
2.1. Ideal muscovite mica	13
2.2. Actual muscovite mica	15
2.3. Muscovite primitive cell	17
2.4. Muscovite substrate	18
Chapter 3. The simulation model	25
3.1. Molecular dynamics: an overview	25
3.2. The simulation model: implementing the computational apparatus	27
3.3. The adopted force field	32
3.4. The model scheme	43
3.5. System preparation	44
Chapter 4. Physical observables	49
4.1. Average densities	49
4.2. Electric field and electric potential	49
4.3. Evaluating the local electric field	51
Chapter 5. Data processing and analysis	57
5.1. IL number and charge densities	57
5.2. The macroscopic Electric field	67
5.3. The AFM tip nanoindentation	68
5.4. Local Electric field	78
Chapter 6. Discussion and Conclusion	81
6.1. Acknowledgment	82
Appendix A. Computer and parallel implementation	83
Bibliography	85
Ringraziamenti	87



## CHAPTER 1

### Ionic Liquid: an Introduction

Ordinary liquids, such as for example water and ethanol, are predominantly composed of electrically neutral molecules. Pure ionic liquids (ILs) instead are salts in liquid state, entirely made up of ionic species. Due to this generic definition, it is important to set and underline a difference between the room temperature ILs (RTILs) and the, so called, “*molten salts*”. Indeed, one usually refers to *molten salts* by considering compounds which are solid at room temperature, as NaCl, and melt in the 1000 K temperature region. Unlike them, RTILs are ionic organic compounds which remain fluid down to, and often below, 373 K. Due to the ionic nature of its molecules, RTILs have also a low vapor pressure and a negligible volatility making them suitable for vacuum and space applications. If an ion tends to escape from the RTIL/vacuum interface, a local unbalanced charge produces a strong attractive interaction which calls the ion back to restore the global neutrality of the system.

RTILs have been studied in these years for their interesting properties and potential industrial applications. They are mainly investigated as powerful novel solvents [1, 2, 3, 4], electrolytes [5], sealants, lubricant [6, 7, 8], and as media for a wide range of applications in electrochemistry [9, 10, 11], green energy [12], green chemistry [13, 14], catalysis [15, 16, 17, 18, 19], photovoltaic [20, 21]. Thanks to their features is not indeed unusual to refer to these substances with terms like *liquid electrolytes*, *ionic fluids*, *liquid salts* or *ionic glasses*. Despite their growing importance in green industry and clean technology, the understanding of their interaction with solid surfaces of common matter is still far from complete. For this reason many efforts of researchers are addressed to study how RTILs behave at interfaces with different classes of solids. Many articles have been published to report important experimental discoveries and smart theoretical models to describe different RTIL behavior types when interacting with metals or insulating materials. In this introductory chapter we intend to provide a brief overview on the nature and properties of this promising class of compounds, For a more detailed analysis of this field the reader can refer to the reviews [22, 23, 24].

#### 1.1. Lowering the melting point/Why RTIL's are liquid at room temperature?

Molten salts and, more in general, several inorganic and organic ionic compounds are solid at room temperature. The inorganic salts are often composed of mono-atomic ions with a typical minimum distance between particles of opposite charge of the order of 2-3 Å. These ionic equilibrium positions generally generate a strongly bonded rigid crystalline structure typically in one of a few, poorly coordinated lattice structures.

System	Mole %	Melting Point [°C]
LiCl	100	610
NaCl	100	803
KCl	100	772
CsCl	100	646
LiCl-CsCl	60-40	355
NaCl-KCl	50-50	658
CsCl-KCl	35-65	610

TABLE 1.1. Melting points of selected Group 1 chlorides.

“Traditional” salts have a large cohesive energy per ion pairs and, as a consequence, relatively high melting temperature in the 10<sup>3</sup> K region. Table 1.1 reports the melting points of some Group 1 chlorides and mixtures [23]. These are significantly above room temperature. An intermediate class of molten salts whose melting point is lower than the traditional molten salts is given by the tetrachloroaluminate(III) salts. Few examples of compounds, and the corresponding melting temperatures, of this class are reported in Tab. 1.2. From these tables one can notice that the characteristic complexity of the compounds plays an important role in the lowering of the melting temperature. Despite an important decrease of the melting points of these salts, we are still above the room-temperature range.

An approximated estimation of the lattice energy  $U_L$  per unit formula for a ionic crystal is given by the Kapustinskii equation [25]:

$$(1) \quad U_L = -K \cdot \frac{\nu |z^+||z^-|}{r^+ + r^-} \left( 1 - \frac{d}{r^+ + r^-} \right)$$

where  $K = 1.2025 \cdot 10^4$  kJ Å mol<sup>-1</sup> (124.63 Å eV per particle),  $d = 3.45 \cdot 10^{-1}$  Å,  $\nu$  is the number of ions in the empirical formula, while  $r^+$ ,  $r^-$ ,  $z^+$  and  $z^-$  are the radii and the elementary charges on the cation and anion respectively. Effectively, applying the understanding of lattice energies gained from this equation, and the rough proportionality of melting temperature to  $U_L/\nu$ , one can assert that the melting point can be lowered by increasing the size and complexity of the cations. By replacing the simple inorganic cations with unsymmetrical organic cations increases the lattice spacing of the solid, and accordingly depresses the melting point close to the room temperature range. This is the path followed by the researchers in the last decades which has yielded to the discovery of the first modern RTILs such as 1-butylpyridinium chloride-aluminium chloride (BPC-AlCl<sub>3</sub>) [26, 27] and the class based on the 1,3-dialkylimidazolium [28, 29, 30].

## 1.2. The dialkylimidazolium cation family and the bis(triflimide) anion

The earliest molten salts with a low melting point, that are the precursors of the modern RTILs, were discovered and studied since the early 20-th century. In the past years many efforts have been made to discover and produce different classes of ILs;

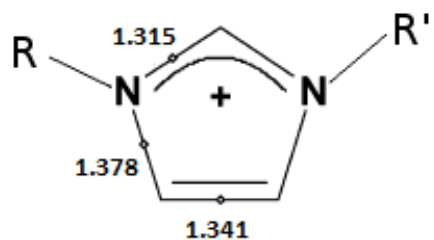


FIGURE 1.1. The imidazolium 5-membered ring with marked equilibrium distances in Å, from Ref. [31]; typical  $\pi$ -electrons shared among nitrogen N and apical carbon sites. R- and R'- are typically alkylic radicals.

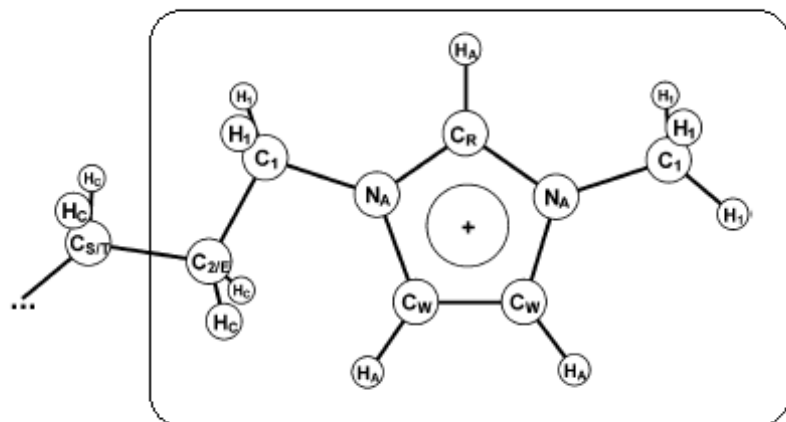


FIGURE 1.2. The 1-alkyl,3-methylimidazolium, often shortened to 1,3-dialkylimidazolium, cation skeleton structure. Atoms are labeled by the AMBER-type notation [31]. C<sub>R</sub> and C<sub>W</sub> are the carbon atoms of the imidazolium ring, C<sub>1</sub> refers to the first carbon atom in any side chain, C<sub>E</sub> is the second carbon atom in the ethyl side chain of 1-ethyl,3-methylimidazolium, C<sub>2</sub> is the second atom in alkyl side chain with more than 2 carbon atoms; C<sub>S</sub> refers to any secondary carbon of the alkyl side chain that is removed at least 2 bonds from the ring, and C<sub>T</sub> is the terminal carbon atom of longer than ethyl side chains. H<sub>A</sub>, H<sub>1</sub>, and H<sub>C</sub> refer to hydrogen atoms attached to the aromatic ring, to the first carbon atom on the side chains, and to carbon atoms on the side chain further removed from the ring, respectively. Abbreviations used for 1-alkyl,3-methylimidazolium cations are [\*mim]<sup>+</sup>=methylimidazolium, with prefixes a=alkyl, m=methyl, e=ethyl, b=butyl, h=hexyl, dd=dodecyl replacing the '\*' symbol. The rounded box encloses the large amount of unbalanced charge of the cation.

System	Mole %	Melting Point [°C]
AlCl <sub>3</sub>	100	192
LiCl-AlCl <sub>3</sub>	50-50	144
NaCl-AlCl <sub>3</sub>	50-50	151
KCl-AlCl <sub>3</sub>	50-50	256

TABLE 1.2. Melting points of selected tetrachloroaluminate(III) salts.

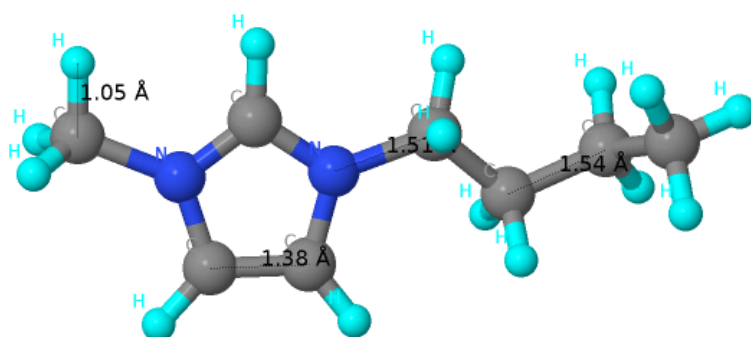
**Jmol**

FIGURE 1.3. The ball-and-stick model structure of the 1-butyl,3-methylimidazolium [bmim]<sup>+</sup> molecular cation frozen in a non-equilibrium instantaneous configuration (fixed a generic snapshot). H, C, N correspond to hydrogen, carbon, and nitrogen atoms respectively. The positive charge is mainly localized on the imidazolium ring (see also Table 3.1 in Sec. 3.3.3 below). The raw chemical formula is [C<sub>8</sub>H<sub>15</sub>N<sub>2</sub>]<sup>+</sup>.

nowadays the researchers are still studying and looking for new possible cationic and anionic species to create innovative RTILs.

Systems made up of alkane-substituted imidazolium cations ([C<sub>n</sub>mim]<sup>+</sup>), paired to a variety of anions (X<sup>-</sup>), such as Cl<sup>-</sup>, PF<sub>6</sub><sup>-</sup>, BF<sub>4</sub><sup>-</sup>, etc., are today the typical examples of RTILs. Imidazolium-based cations stand out as excellent candidates for the creation of a RTIL thanks to its wide window in electrochemical stability compared to other families of ILs, like the alkylpyridinium family. Imidazoles are a class of organic compounds based on the C<sub>3</sub>H<sub>4</sub>N<sub>2</sub> imidazole ring. They are aromatic heterocyclic alkaloids with a similar 5-membered ring structure but varying alkyl substituents R-, R'- at nitrogen sites (see Fig. 1.1), commonly known as 1, 3 sites. Salts of imidazole, where the imidazole ring is in the cation, are known as imidazolium salts. The imidazolium ring is somewhat deformed with respect to a regular pentagon, due to the different length of

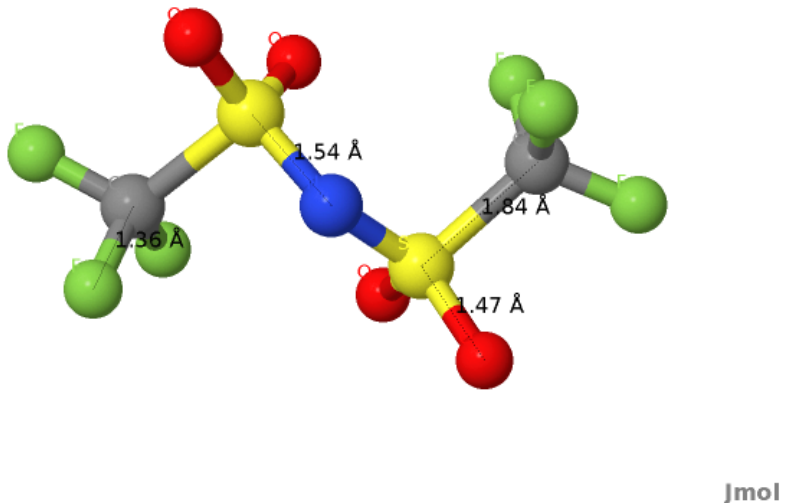


FIGURE 1.4. The ball-and-stick model structure of the bistriflimide  $[\text{Tf}_2\text{N}]^-$ ,  $[(\text{CF}_3\text{SO}_2)_2\text{N}]^-$  molecular anion in a non-equilibrium instantaneous configuration. Chemical symbols for the atoms are indicated. The net negative charge is mainly localized around the central nitrogen atom (see also Table 3.2 in Sec. 3.3.3 below). The atomic charges of sulfur and oxygen neutralize each other to a large extent.

the N-C bonds and to the different substituents. The distortion of the ring caused by different alkyl substituents is however so small that the use of a symmetrical ring geometry, with respect to the axis passing through the apical carbon and half of the distance between the basal carbon atoms in the ring, represents a good approximation [31]. The biggest distortions of the ring are due to the presence of double and single bonds among N and C atoms which make the pentagon sides unequal. In particular we can underline the presence of 4  $\pi$ -electrons predominantly shared between  $\text{C}_R$  and the two  $\text{N}_A$  nitrogen sites, as we can infer from Fig. 1.1 (see 1.2 for atom-nomenclature). On the other hand, the geometry of the alkyl chains are similar to those found in normal aliphatic chains. Because of the substituents ( $\text{R}$ ,  $\text{R}'$ ) at 1, 3 nitrogen sites, by using the IUPAC conventions, the imidazolium-based cations are also known as 1,3-dialkylimidazolium cations. Different alkyl substituents produce 1,3-dialkylimidazolium-based RTILs with different physical, chemical, and electrochemical properties. The most studied RTILs in the 1980's were those containing the 1-ethyl,3-methylimidazolium cation, indicated in brief by  $[\text{emim}]^+$ , while, in the present work, we focus our attention on the 1-butyl,3-methylimidazolium cation, or  $[\text{bmim}]^+$  shown in Fig. 1.2, and in Fig. 1.3. As expressed by its name, this cation has got one butyl and one methyl as residues respectively at 1 and 3 (nitrogen) positions along the imidazolium ring. Butyl is an alkylic substituent chain composed of 4 carbons and raw formula  $\text{C}_4\text{H}_9$ , while methyl is the  $\text{CH}_3$  radical.

The two most important features of the  $[\text{bmim}]^+$  molecule is that its unbalanced positive charge is mainly localized on the imidazolium ring, or on the atoms of the alkylic chain nearest to the ring, and that the two different approximatively neutral alkyl tails make the geometric molecular configuration strongly asymmetric. On the basis of the issues reported above, these are the main reasons for the low melting point of the IL containing this cation species. The pyridinium- and the imidazolium-based ILs share the disadvantage of being reactive with water. This surely marks a limit in the possibility to study these RTILs and in their applicability. To overcome this difficulty, researchers have tried to analyze salts based on dialkylimidazolium cations, but with water stable anions like tetrafluoroborate  $[\text{BF}_4]^-$ , hexafluorophosphate  $[\text{PF}_6]^-$ , nitrate  $[\text{NO}_3]^-$ , sulfate  $[\text{SO}_4]^{2-}$ , acetate  $[\text{CH}_3\text{COO}]^-$ , and many others.

In the early 1990's, the production of water-and air-resistant RTILs has opened the way to a new series of promising chances of application. In this framework we can, indeed, understand how one can tune the physical-chemical properties of these salts. The large number of available modern ionic families, the possibility of an "easy" modification of the alkyl substituent-chains of the cation and the possibility of a simple replacement in the inorganic anion, allow a detailed tailoring of the ILs to fit the industrial requirements.

In this work, for the anion, we consider the bistriflimide anion shown in Fig. 1.4. Its extended name is bis(trifluoromethane)sulfonimide, and can be written with the shorthand  $[\text{Tf}_2\text{N}]^-$ , or with the raw formula  $[(\text{CF}_3\text{SO}_2)_2\text{N}]^-$ . The  $[\text{Tf}_2\text{N}]^-$  ion is a non-coordinating anion widely used in RTILs since it is less toxic and more stable than "traditional" anions.

In addition to water stability, and low toxicity, the choice of the  $[\text{bmim}]^+[\text{Tf}_2\text{N}]^-$  ionic liquid for the present work has been suggested by the fact that it is considered one of the archetype systems by the ILs scientific community and, therefore, many studies have been reported. Moreover, this RTIL is being studied by P. Milani's experimental group at University of Milan, in collaboration with QUILL (Queen's University Ionic Liquids Laboratories) at the Queen's University of Belfast.

## CHAPTER 2

### The mica substrate

Mica minerals are phyllosilicates with a common basic crystal structure, platy morphology and perfect basal, i.e. (001), cleavage. The mineral group is composed by some 41 species but its most familiar representatives among the important rock-forming minerals are muscovite and biotite.

This mica minerals have the general formula  $AR_{2-3}\square_{1-0}T_4O_{10}X_2$ , where A is an interlayer cation ( $K^+$ ,  $Na^+$ ,  $Ca^+$ ,  $Ba^+$ ,  $Cs^+$ ,  $NH_4^+$ ); R is an octahedral layer cation ( $Al^{3+}$ ,  $Mg^{2+}$ ,  $Fe^{2+}$ ,  $Fe^{3+}$ ,  $Li^+$ ,  $Ti^{2+}$ ,  $Mn^{2+}$ ,  $Zn^{2+}$ ,  $Cr^{3+}$ ,  $Na^+$ );  $\square$  is a vacancy in the octahedral layer; T is a tetrahedral layer cation ( $Si^{4+}$ ,  $Al^{3+}$ ,  $Fe^{2+}$ ,  $Fe^{3+}$ ,  $Be^{2+}$ ,  $B^{3+}$ ); and X is an anion (ligand) not bonded to T ( $OH^-$ ,  $F^-$ ,  $Cl^-$ ,  $O^{2-}$ ,  $S^{2-}$ ). Micas can be catalogued in many different ways on the base of their structural properties, and one important way consists in splitting and organizing them into two big families; dioctahedral and trioctahedral micas. Formally a mica is dioctahedral if contains  $< 2.5$  octahedral (R) cations per formula unit (pfu), and trioctahedral with  $\geq 2.5$  octahedral cations pfu.

Micas are chemically and geochemically complex. In particular, muscovite [ $KAl_2AlSi_3O_{10}(OH)_2$ ] is an aluminosilicate mineral with compositional affinity to feldspar, feldspathoids and quartz, whereas biotite [ $K(Mg,Fe^{2+})_{3-2}Al_{0-1}Al_{1-2}Si_{3-2}O_{10}(OH)_2$ ] is essentially a ferromagnesian mineral series. Also, the common micas are important host minerals for Li, Rb, Cs, Ba, V, Cr, Be, B,  $H_2O$ , F, and Cl ions. This compositional diversity and exotic minor and trace element chemistry of micas reflect both an accommodating crystal structure and an extremely wide range in mineral stability. In the years, muscovite and phlogopite have become of considerable economic importance. The combined properties of perfect cleavage, elasticity, flexibility, high dielectric constant, electrical resistivity, good capacitance stability [32], low thermal conductivity, excellent thermal stability, incombustibility, and non-flammability made cleavage sheets of muscovite and Mg-rich phlogopite ideal for many electrical, electronic and thermal insulation purposes. Mica sheets are indeed used in equipment like capacitor, transformers, radio, radar circuits. Natural mica sheets, however, are not always available in the required size as demanded by the industry. Great progress has been achieved in making artificial mica called micanite. Mica films are placed with alternate layers of binding materials like shellac, alkyl, or silicon resin and then pressed and baked. It is then possible to cut or punch micanite according to requirements.

#### 2.1. Ideal muscovite mica

We focus our attention on muscovite [ $KAl_2AlSi_3O_{10}(OH)_2$ ] which is a dioctahedral mica and the second most common mica mineral in nature. The ideal structure of

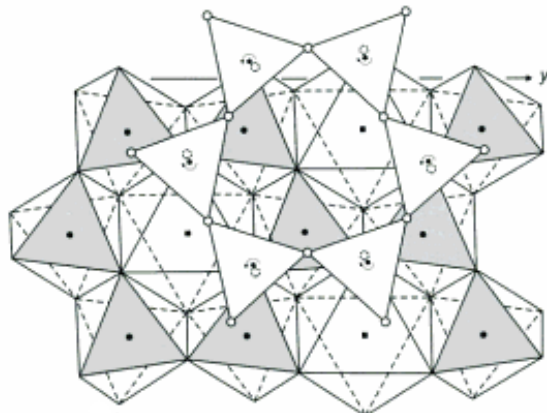


FIGURE 2.1. The octahedral layer and part of the attached tetrahedral upper layer of muscovite 2M<sub>1</sub>. Small full circles are Si, Al atoms. Apical oxygens (dotted circles) of the downward pointing SiO<sub>4</sub> tetrahedra are shared with the octahedral layer.

muscovite is a sandwich assembled from layers of cations in:

- (1) tetrahedral coordination with oxygen (tetrahedral layer: T=Al-Si cations);
- (2) octahedral coordination with apical oxygen and X=OH anions (octahedral layer: R=Al cations);
- (3) 12-fold coordination with basal oxygen (interlayer: A=K cations).

The tetrahedral layer unit is the most strongly bonded and, therefore, the most fundamental in defining the structure. The T=Al-SiO<sub>4</sub> tetrahedra share the 3 basal oxygens into a two dimensional sheet, resulting in a strongly bonded aluminosilicate anion complex of [AlSi<sub>3</sub>O<sub>10</sub>]<sup>5-</sup> formula. The two-dimensional oxygen net is composed of six-membered hexagonal rings. The unshared apical oxygens are all on the same side of the sheet, see Fig. 2.1.

The octahedral layer is sandwiched between two tetrahedral layers. The upper one points downward, while the lower one points upward. Its construction is best envisaged by first adding the X=OH anions, which are functionally part of the octahedral layer, to the tetrahedral layer unit. The OH anions are located at the center of each hexagon ring at the same height as the apical oxygens. Thus, in the ideal structure, the apical oxygens and OH anions form a closed-packed layer. When a tetrahedral layer with downward pointing tetrahedra is positioned on top of an upward pointing tetrahedral layer and displaced by an opportune amount, related to the typical T=Al-Si cation distance [33], the two layers of apical oxygens and X=OH anions form a single stacking unit. The enclosed tetrahedral and octahedral interstices in this unit are potential cation positions. The 6 potential tetrahedral positions pfu are not occupied in micas, nor in phyllosilicates in general. The 3 potential octahedral positions pfu are occupied differentially in micas. In dioctahedral micas, and, more in detail, in ideal muscovite,

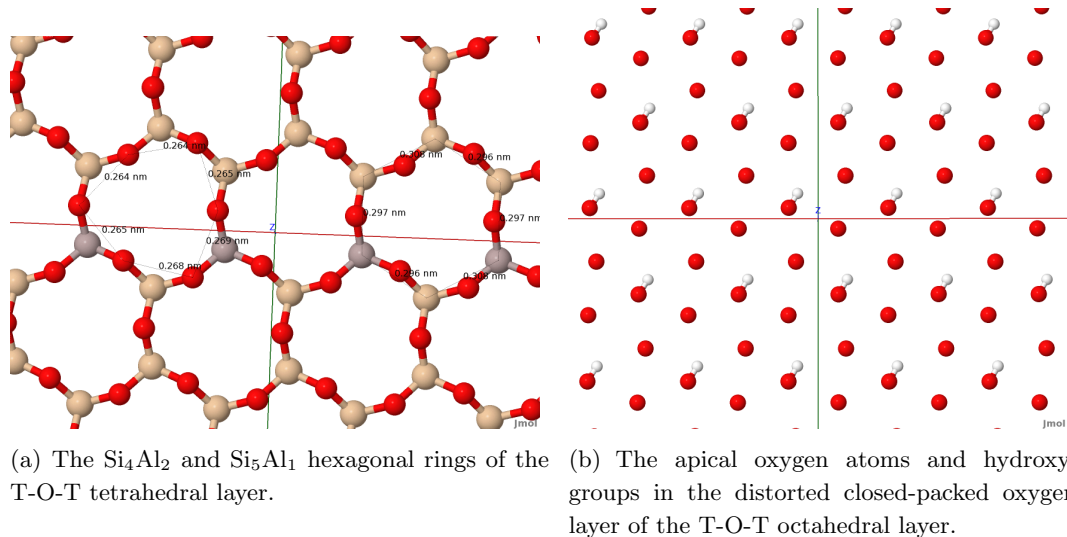


FIGURE 2.2

two positions (M2 site) are occupied by R=Al and one (M1) is vacant. The three-layer (tetrahedral-octahedral-tetrahedral) sandwich unit which are now conceptually assembled is referred to variously as the *t-o-t* or T-O-T unit or 2:1 layer unit.

Due to the long-range-ordered (ideal) tetrahedral Al substitution for Si, with characteristic 3:1 Si:Al ratio, muscovite is characterized by a significant excess negative charge on the 2:1 layer unit, which is compensated by a large number of, positively charged interlayer cations. In the ideal structure the interlayer cation  $\text{K}^+$  is in 12-fold coordination with the basal oxygen atoms. It is centered in the cavity formed by back-to-back hexagon rings of  $\text{TO}_4$  tetrahedra, superimposed with the X anion in normal projection, and coordinated to six basal (bridging) oxygens of the upward-pointing tetrahedral layer above it and six basal (bridging) oxygens of the downward-pointing tetrahedral layer below it.

The 2:1 T-O-T layer units are bonded together by relatively weak A(=K)-O bonds; this structural feature readily accounts for the characteristic perfect basal (001) cleavage and defines the fundamental layering of the muscovite.

## 2.2. Actual muscovite mica

Actual muscovite differs significantly from the ideal one in chemical and structural complexity, that arises variously from atomic substitutions mainly in A, T, and X sites, distortion of the six-membered rings of  $\text{TO}_4$  tetrahedra, short-ranged cation ordering and polytypism. As an instance, actual samples differ in chemical composition because of the presence of relatively small quantities of substituents such as Ca, Si, Mg, Fe, Mn, F, Cl as in the raw formulae  $[(\text{K}_{0.94}\text{Si}_{0.08}\text{Ca}_{0.01})(\text{Mg}_{0.01}\text{Fe}_{0.16}\text{Mn}_{0.01}\text{Al}_{1.83})(\text{Al}_{0.90}\text{Si}_{3.10})\text{O}_{10}(\text{OH}_{1.83}\text{F}_{0.17})]$ ,  $[(\text{K}_{0.89}\text{Na}_{0.09})(\text{Mg}_{0.01}\text{Fe}_{0.14}\text{Al}_{1.88})(\text{Al}_{0.96}\text{Si}_{3.04})\text{O}_{10}(\text{OH}_{1.80}\text{F}_{0.20})]$  [33], where experimental percentages of atomic substituent species are reported. The presence of substituents and, simultaneously, the relative non-perfect degree of fit between the ideal size of the isolated tetrahedral and octahedral sheets

## 2. THE MICA SUBSTRATE

Muscovite- $2M_1$  C2/c primitive cell;  
 $a = 5.1918 \text{ \AA}$   $b = 9.0153 \text{ \AA}$   $c = 20.0457 \text{ \AA}$ ,  $\alpha = 90.0^\circ$   $\beta = 95.735^\circ$   $\gamma = 90.0^\circ$

Site-Element	Symmetry	<i>x</i>	<i>y</i>	<i>z</i>
A-K	4e	0	0.0980	0.25000
M2-Al	8f	0.2502	0.0835	0.00008
T1-(Si:Al, 3:1)	8f	0.4646	0.9291	0.13553
T2-(Si:Al, 3:1)	8f	0.4516	0.2581	0.13559
O1	8f	0.4167	0.0927	0.16829
O2	8f	0.2505	0.8107	0.15783
O3	8f	0.2505	0.3703	0.16869
O4	8f	0.4610	0.9432	0.05343
O5	8f	0.3859	0.2515	0.05348
OH	8f	0.4566	0.5627	0.05018
H	8f	0.3727	0.6499	0.05990

TABLE 2.1. Atomic C2/c symmetry Wyckoff positions in internal units for muscovite  $2M_1$  in its primitive cell [33].

causes a distortion in the layer structures including a rotation of the adjacent  $TO_4$  tetrahedra in the six membered-rings, about their vertical axis. The local symmetry of individual six-membered rings is now reduced to ditrigonal as in Figs.2.1, 2.2(a). The tetrahedral-octahedral layer misfit is also partially accommodated by distortion of the octahedral sheet, through stretching and thinning. The closed-packed layer of OH and apical oxygen atoms is slightly distorted as visible in Fig. 2.2(b).

Polytypism also contributes to increase the differences between real and ideal muscovite strucutres. A polytype is a structural modification of a layered structure arising from a different stacking arrangement. It is characterized by a structural lattice spacing in the stacking direction that is an integer multiple of the thickness of the fundamental layer. Mica polytypes can be generated by invoking regular rotations between layers or regular translations of successive layers. Interestingly, there are two possible inequivalent surfaces for a change in stacking in micas: the interlayer plane and the octahedral cation plane. The structures of real micas suggest that the interlayer plane is a surface for stacking changes in polytypes. It can be shown that there are only six standard mica polytypes [33] commonly labeled 1M,  $2M_1$ , 3T, 2O,  $2M_2$ , and 6H in the shorthand polytype notation of Ramsdell, where the first symbol gives the number of layers in the repeated primitive cell, the second the crystal system, and the subscript distinguishes polytypes of the same repeated unit and symmetry. The  $2M_1$  polytype is predominant for dioctahedral muscovite and, therefore, it is the polytype we chose for our substrate. Henceforth we refer to it when talking generically about muscovite.

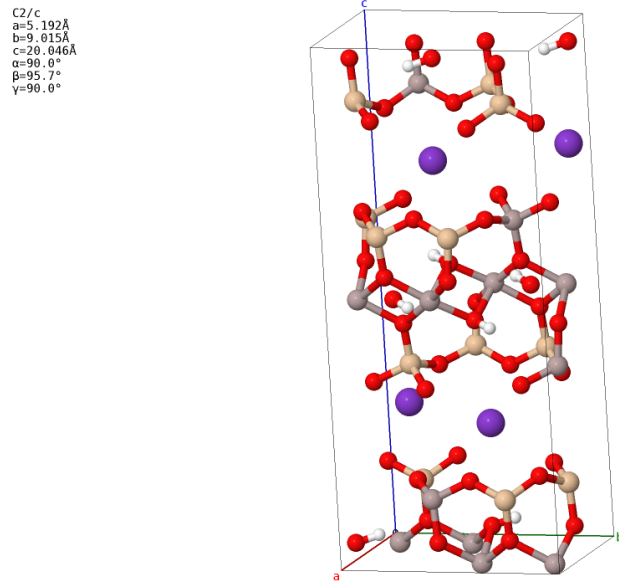


FIGURE 2.3. The complete bulk monoclinic primitive cell of the 2M<sub>1</sub> muscovite C2/c substrate, with approximate cell parameters.

### 2.3. Muscovite primitive cell

The muscovite-2M<sub>1</sub> has got a monoclinic primitive cell which belongs, from the crystallographic point of view, to the C2/c space group [33]. To create our model substrate layer we consider, as reference, the detailed structure data found by Rothbauer using single-crystal neutron diffraction, reported in Table 2.1. Here are reported all the geometrical parameters of the primitive cell, and starting from these parameters we are also able to reconstruct all the atomic equilibrium positions in the cell by using the space group transformations which account for its internal symmetry. This can be done easily by a useful free utility available at Bilbao crystallographic server [34]. The utility “WPASSING” identifies the Wyckoff positions of an atomic site reported in the second column of Table 2.1, and assigns the corresponding complete set of atomic positions for the species which occupies that site. In this passage we consider the different cationic sites as occupied by one single type of atomic species without considering impurity substitutions. In particular we take A=K as interlayer cations, Al as octahedral cations in site M2, while only Si as tetrahedral-coordinated cations in sites T1 and T2. We then replace 1/4 of the Si cations with Al cations, to obtain a 3:1 Si:Al ratio accounting for the characteristic presence of Al substitution in the ditrigonal rings of T-O-T as mentioned above and as we can infer from the raw formula of muscovite [KAl<sub>2</sub>AlSi<sub>3</sub>O<sub>10</sub>(OH)<sub>2</sub>]. In our model we do this substitution regularly for each primitive cell, while in nature a certain degree of disorder is present. This way, we obtain a hybrid muscovite primitive cell of ideal chemical purity (no impurity substitutions) and a realistic geometrical structure which accounts for distortions and Al substitutions. This construction generates a primitive cell containing 84 atoms (4 K, 12 Si, 12 Al, 48 O, 8 H), which is represented in Fig. 2.3, with a list of the cell parameters.

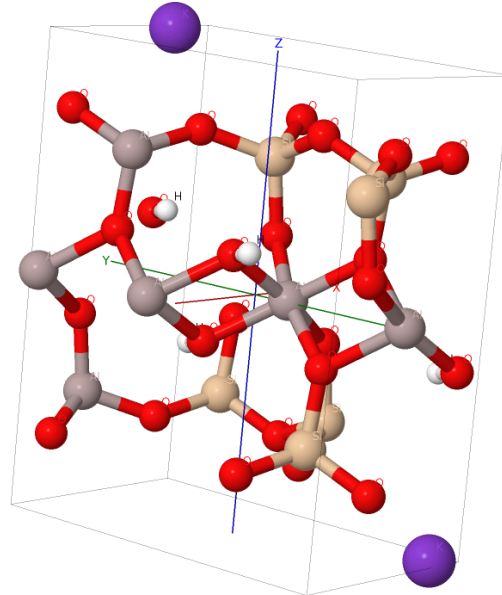


FIGURE 2.4. The muscovite fundamental single-layer orthorombic cell.

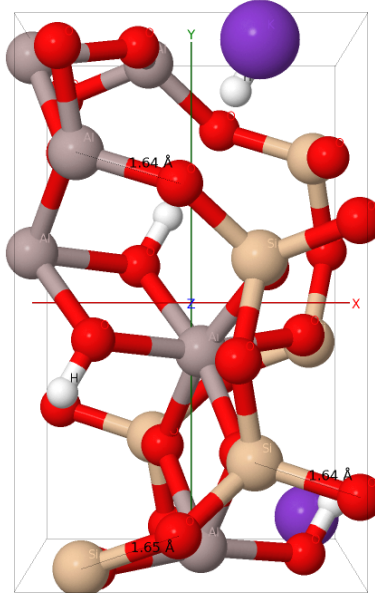


FIGURE 2.5. The muscovite fundamental single-layer orthorombic cell seen from the  $\hat{z}$  axis, with the indications of a few characteristic bond lengths.

#### 2.4. Muscovite substrate

Starting from the bulk monoclinic primitive cell of idealized muscovite we construct a 2-D periodic slab geometry to represent the mica (001) surface. We obtain

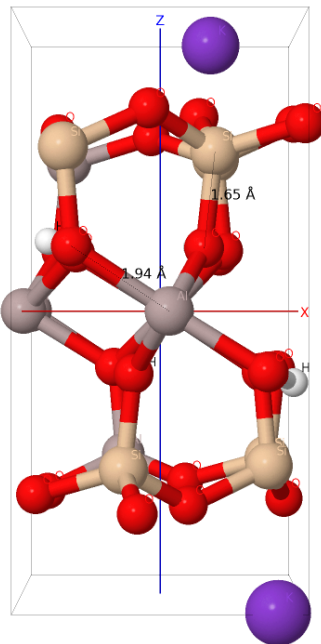


FIGURE 2.6. The muscovite fundamental single-layer orthorombic cell seen from the  $\hat{y}$  axis, with a few characteristic bond lengths.

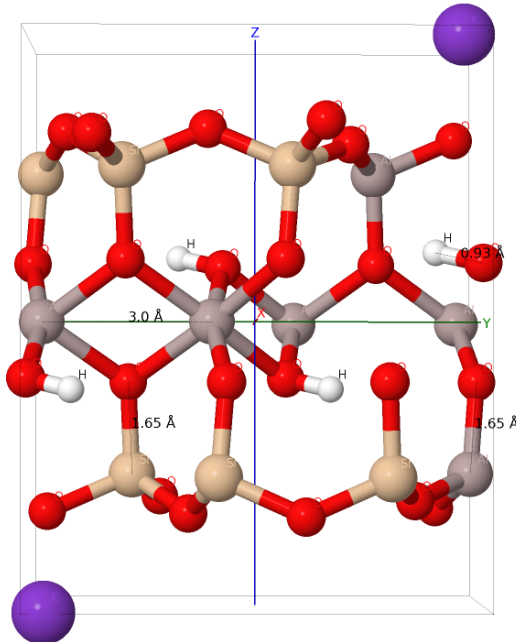


FIGURE 2.7. The muscovite fundamental single-layer orthorombic cell seen from the  $\hat{x}$  axis, with a few characteristic bond lengths.

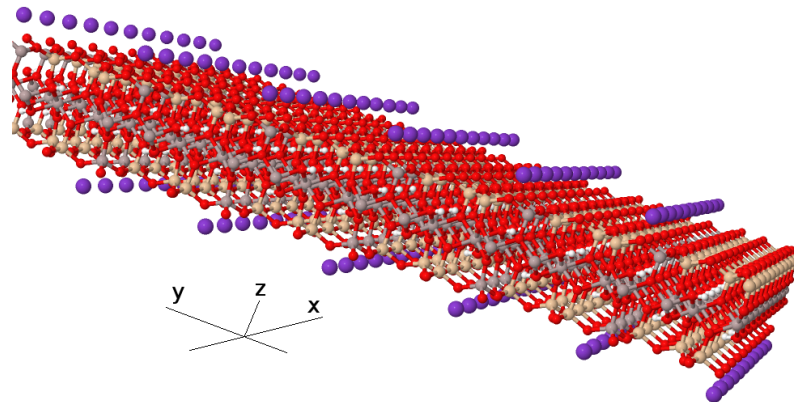


FIGURE 2.8. Fully relaxed muscovite neutral substrate in a repeated-all geometry.

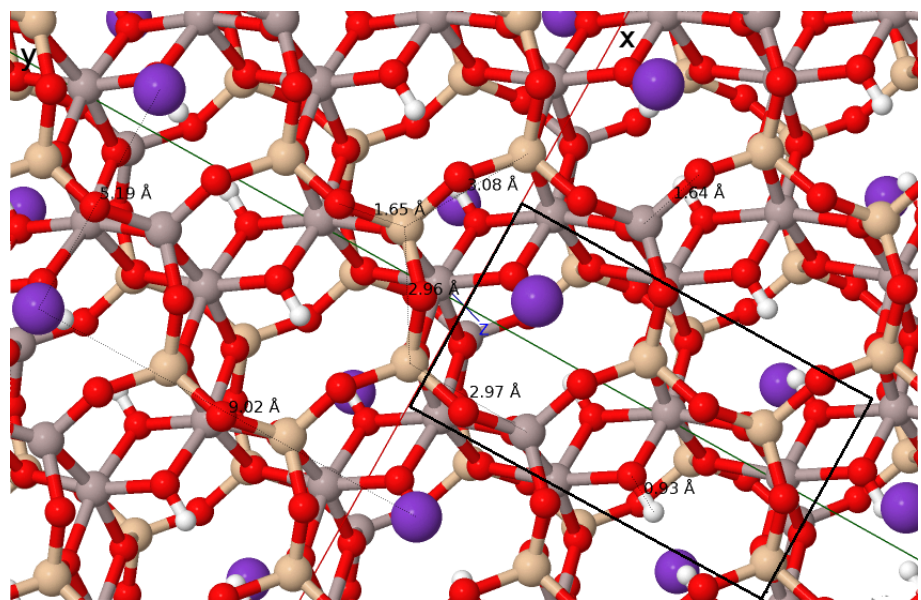


FIGURE 2.9. The detailed upper side of Muscovite neutral substrate with atomic equilibrium positions. Here are visible typical  $(\text{Si}_4\text{Al}_2)$  and  $(\text{Si}_5\text{Al}_1)$  ditrigonal rings with K cations in 6-fold coordination with the underlying basal oxygens. The fundamental cell is highlighted and a few equilibrium bond lengths are also reported.

it by cutting ideally a bulk muscovite structure along a T-O-T interlayer plane. For reasons of electro-neutrality of the system, as starting point, we retain only half of the  $\text{K}^+$  cations belonging to the cut interlayer, namely those which are placed above the

Muscovite surface fundamental cell;  
 $a = 5.1918 \text{ \AA}$   $b = 9.0153 \text{ \AA}$ ,  $\alpha = 90.0^\circ$   $\beta = 90.0^\circ$   $\gamma = 90.0^\circ$

Element	number of atoms	$m$ [amu]
K	2	39.0983
Si	6	28.0800
Al	6	26.9815
O	24	15.9949
H	4	1.0078
Total	42	-

TABLE 2.2. Type, number of atoms and atomic masses in our fundamental surface cell.

ditrigonal rings with a double Al substitution for Si. It is, indeed, well known [35] that these sites are energetically favorite with respect to those placed above ditrigonal rings with a single Al substitution (Figs. 2.4- 2.9). This fact can be explained in the way that each  $K^+$  interlayer cation is ideally shared between a double Al substitution ditrigonal ring  $Si_4Al_2$  and a single Al substitution ditrigonal ring  $Si_5Al_1$ , which belong to two superimposed-adjacent T-O-T layers. Moreover in the tetrahedral cation plane of a single T-O-T layer, we have ideally as many ditrigonal ( $Si_4Al_2$ ) rings as ditrigonal ( $Si_5Al_1$ ) rings, see Fig. 2.2 (a). Within this ideal framework it is clear that, when the two T-O-T units are separated along the interlayer plane, the  $K^+$  cations are subdivided following mostly the more energetically favorable sites. It is clear that a muscovite (001) surface cannot be described simply as an ideal truncated bulk structure with half of the interlayer cations, but it should be necessary to allow for the atomic displacements and ensuing structural modifications. Muscovite surfaces do not suffer a particularly radical modification; the truncation induces mostly a relatively small inward (toward the bulk) displacement of the exposed cations and small rearrangements of the first atomic layers close to the interface [35].

An important issue to consider for the simulations, is that we also must match the necessity of a limited number of parameters and degrees of freedom (related to the number of atoms) to save CPU-time, with at the same time, the contrasting need of an adequate number of atoms in order to simulate realistically the behavior of the substrate at the interface. A good compromise, which accounts for these points, is to create a smaller fundamental cell, containing a limited number of atoms left free to move. We create the new fundamental cell by taking half of the primitive monoclinic cell in the  $c$  direction with a cut along interlayer planes of the real primitive cell and a splitting procedure which take care of the problems mentioned above. In practice we are now considering a cell composed of one T-O-T unit layer with one half of the  $K^+$  cations at each surface. This scheme leads to a halving of the total number of atoms in the new 2-D cell. This cell halving also allows for a simplification of its geometry to an orthorhombic one as depicted in Figs. 2.4– 2.7. The basic cell properties are reported in Table 2.2.

$$a=57.1098 \quad b=54.0918, \quad \alpha=90.0^\circ \quad \beta=90.0^\circ \quad \gamma=90.0^\circ$$

Element	Neutral super-cell	Charged super-cell
	num. atoms	num. atoms
K	132	116
Si	396	396
Al	396	396
O	1584	1584
H	264	264
Total	2772	2756

TABLE 2.3. Super-cells properties of the muscovite layer.

We are thus ready to generate complete substrates of any size multiple of the  $ab$  rectangle, defined in Tab. 2.2. For the interaction with a RTIL fluid we generate a conventional super-cell used for all successive simulations (Figs. 2.8, 2.9). The 2-D super-cell is composed by  $11 \times 6$  fundamental cells. Its properties are reported in Tab. 2.3

We have prepared two different kinds of substrate, which are different only in the number of  $\text{K}^+$  cations on the super-cell side which we are going to use as interface with RTIL. The first case corresponds to the simple repetition of the fundamental cell created above. This first case represents a neutral surface. The total number of atoms of each species is listed in the left column of Table 2.3. The second considered case corresponds to a charged surface where a strong negative charge is located at surface [36]. We obtain this by removing 16  $\text{K}^+$  cations in the super-cell (about 24.2% of the mobile cations exposed to the external environment) in a asymmetric way, as indicated by Fig. 2.10. This charge unbalance produces a mean surface charge of  $\sim 0.5 \text{ e/nm}^2$ . As we shall see in Sec. 3.5 below, in the simulations we will compensate the negative surface charge by means of an equal opposite positive charge in the interacting RTIL. Table 2.3 represents the atom list of this charged surface.

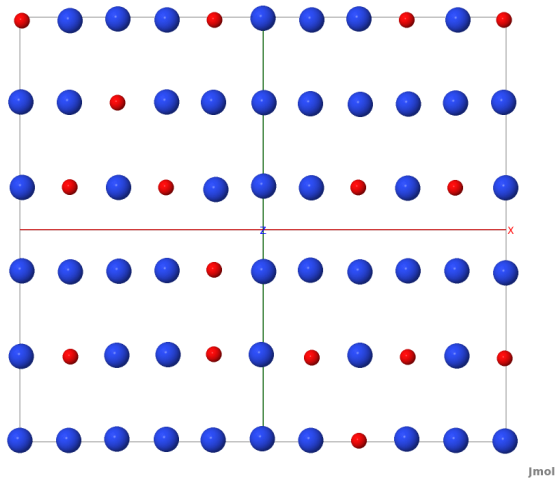


FIGURE 2.10. Differences in surface- $\text{K}^+$  between charged and neutral super-cells. The smallest dots represent the locations where  $\text{K}^+$  is present only in the neutral surface, but not in the charged one.



## CHAPTER 3

# The simulation model

## 3.1. Molecular dynamics: an overview

Molecular dynamics (MD) is a computer simulation technique based on the integration of the equations of motion of a many body system of known initial configurational condition. In MD classical mechanics defines the atomic motions, and, in the adiabatic approximation [37], the quantum Schröedinger's equation is replaced by Newton's law:

$$(2) \quad \mathbf{F}_i = m_i \mathbf{a}_i,$$

where the subscript  $i$  identifies to the  $i$ -th atom/ion of the system,  $m_i$  is its mass,  $\mathbf{a}_i = d^2\mathbf{r}_i/dt^2$  its acceleration and  $\mathbf{F}_i$  the force acting upon it, due to interaction with the environment. Atoms interact with each other and, simultaneously, with external potentials. In practice, these interactions are defined by a suitable potential energy function with appropriate parameters; this function is in turn constructed by means of a set of suitably combined parametrized functions generally known as "force-field" which implicitly contains the electronic motion. As the atoms move, their relative or absolute positions change and forces change accordingly. In practice, the essential ingredient containing the physics is constituted by the forces, which are obtained as the gradient of the potential energy function. A simulation is realistic only to the extent that inter-atomic forces are similar to those that real atoms would experience when arranged in the same configuration. The realism of the simulation is therefore governed in large part by the ability of the potentials chosen to reproduce the behaviour of the material under the conditions at which the simulation is run. This is not an easy task, especially for systems with strong correlations. Moreover in this approach electrons enter only indirectly in defining the potentials and, therefore, the difficulty in considering explicitly the electronic polarization produces systematic deviations from real systems.

In contrast with Monte Carlo method, MD is, in principle, a completely deterministic technique. In practice, the finiteness of the integration time step and arithmetic rounding errors will eventually cause the computed trajectory to deviate from the true trajectory. Typically one has the configurational starting state of a system of  $N$  atoms, and after the integration of the classical equations of motion, obtains the final configurational state. The computer calculates a trajectory in a  $6N$ -dimensional phase space ( $3N$  positions and  $3N$  momenta). However, such trajectory is usually not particular relevant by itself since the initial condition is just a "typical" situation, and does not represent any specific configuration which could be accessed experimentally.

MD is a statistical mechanics method. Like Monte Carlo techniques it is a way to obtain a set of configurations distributed accordingly to some statistical ensemble. According to statistical physics, physical quantities are represented by averages over configurations distributed according to an appropriate statistical ensemble. A trajectory obtained by molecular dynamics provides such a set of configurations. Therefore, a measurement of a physical quantity by simulation is simply obtained as an arithmetic average of the various instantaneous values assumed by that quantity during the MD run. In the limit of very long simulation times, one could hope that the phase space is fully sampled, and in that ergodic limit this averaging process would yield correct thermodynamic properties. In practice the runs are always of finite length, and one should exert caution to estimate whether the sampling is good or biased. MD can be considered as a valid method which allows us to simulate atomic or molecular systems with a reasonable precision, with a relatively high number of particles, and target times of several tens of ns. It is a very powerful technique but has -of course- its limits as we will point out in the next sections.

**3.1.1. The classical approximation.** It is well established, for example by spectroscopical observations, that, in principle, at the atomistic level matter obeys quantum laws rather than classical laws. Accordingly, Newton's equation should be replaced by Schröedinger's equation. Under suitable conditions, the classical approximation is sufficiently detailed to describe reasonably our atomistic system. A simple test for its validity is based on the de Broglie thermal wavelength [38], defined as:

$$(3) \quad \Lambda = \sqrt{\frac{2\pi\hbar^2}{mk_B T}},$$

where  $m$  is the lightest atomic mass and  $T$  is temperature. The classical approximation is justified if  $\Lambda/a \ll 1$ , where  $a$  is the mean nearest-neighbor separation. The classical approximation tends to fail for very light systems such as H<sub>2</sub>, He, and occasionally Ne, and quantum effects increase in importance when  $T$  is sufficiently lowered. Even if we are studying a molecular system with different atomic species, we can apply this quick test. In our calculations the lightest atomic species involved is H, with mass  $m_H = 1.008$  amu (see Tab. 3.1); the next is C, with mass  $m_C = 12.011$  amu. It is possible to extract a raw estimation of  $a$  for an arbitrary atomic species of IL using the formula  $a \approx n^{-\frac{1}{3}}$ , where  $n$  is the average number atomic density of the order of  $8 \cdot 10^{-2}$  Å<sup>-3</sup> in our calculations. At the minimum temperature used in our simulation,  $T = 300$  K, we have therefore:

$$\begin{aligned} \frac{\Lambda_C}{a} &\approx \frac{0.29 \text{ \AA}}{2.3 \text{ \AA}} \approx 0.12, \\ \frac{\Lambda_H}{a} &\approx \frac{1.00 \text{ \AA}}{2.3 \text{ \AA}} \approx 0.43. \end{aligned}$$

It should be clear therefore that the hydrogen dynamics must be considered a border limit of the approximation and that the resulting detailed trajectories must be interpreted with extreme caution. The errors induced by the classical approximation are believed to be of smaller or comparable importance to the inaccuracies of the force field.

Essentially, the classical approximation for the description of atomic-molecular systems with a large number of atoms is unavoidable at the present. Within the framework of this classical approximation however quantum effects are not totally neglected how we will see in the next sections.

**3.1.2. Time and size limitations; PBCs.** Typical MD simulations can be performed on systems composed of thousands of atoms, and for simulation times ranging from a few picoseconds to hundreds of nanoseconds, depending also on the computer power available. While these numbers are certainly respectable, they are completely negligible relative to macroscopic and/or slow phenomena. It may happen to run into conditions where time and/or size limitations become important.

A simulation is “safe”, from the point of view of its duration, when the simulation time is much longer than the relaxation time of all local and global quantities we are interested in. Even if the relaxation time is often unknown and, in practice, difficult to estimate, it is not uncommon to find cases where the relaxation time of a physical property is orders of magnitude larger than times achievable by simulation (this occurs typically near a phase transition). In such case MD is most likely not the best approach.

Moreover, it is in practice impossible to simulate a number  $N$  of atoms usually contained in a real extended system ( $\sim 10^{23}$ ). To represent an extended system by means of a rather small ( $N \sim 10^3, 10^4$ ) number of particles, it is customary to use periodic boundary conditions (PBCs). Particles are, indeed, enclosed in a MD simulation box, or supercell, and this box is replicated infinite times with the rigid translations of a Bravais lattice. The replicated boxes are also known as image boxes or image cells. PBCs mitigate strongly the finite-size effects that a truncated cluster would induce. However, a limited system size with PBCs can induce unphysical and undesired artifacts. It is necessary to compare the size of MD cell with the correlation lengths of the spatial correlation function of interest, and it is clear, that all the oscillation phenomena with a characteristic length larger than the characteristic MD box size cannot occur. For all these reasons, when setting up an MD simulation, it is important to define carefully the MD box size accordingly to the system properties we wish to address.

### 3.2. The simulation model: implementing the computational apparatus

The creation of a reliable theoretical-computational model which simulates a real physical system depends, as we have said above, on the implementation of the chosen simulation method with suitable computational tools, on the generation of a theoretical apparatus pointing to the best realism as possible to mimic real phenomena, and on the optimization of the connection between these two logic structures. In the present chapter we intend to describe the main features of the model.

As we pointed out in the previous section, MD is a deterministic technique which provides the trajectories of a set of atoms given an initial configuration. These trajectories are mainly governed by the parametrized potential functions which better suit and model the system under consideration. We consider a system composed by  $N$  atoms in a classical conservative approximation. The Hamiltonian  $H$  can be written as the sum

of the kinetic and potential energy functions:

$$(4) \quad H(\mathbf{r}, \mathbf{p}) = K(\mathbf{p}) + V(\mathbf{r}),$$

where

$$(5) \quad \mathbf{r} = \{\mathbf{r}_1, \mathbf{r}_2, \dots, \mathbf{r}_N\}$$

$$(6) \quad \mathbf{p} = \{\mathbf{p}_1, \mathbf{p}_2, \dots, \mathbf{p}_N\}$$

represent the coordinates in the position-momentum phase space of the  $N$  particles. The kinetic term can be written in the usual form

$$(7) \quad K = \frac{1}{2} \sum_{i=1}^N \sum_{\alpha=x,y,z} \frac{p_{i\alpha}^2}{m_i},$$

where  $m_i$  is the atomic mass of atom  $i$ . The potential function is globally translationally and rotationally invariant, and is usually composed of terms depending on the relative positions of the atoms with respect to each other, plus possible terms representing external fields which depend instead on their absolute positions. It has been recognized that the two-body approximation is very poor for most condensed systems. For this reason we can infer that the potential  $V(\mathbf{r}) \equiv V(\mathbf{r}_1, \dots, \mathbf{r}_N)$  is composed by many-body terms so that we can write it as

$$(8) \quad V(\mathbf{r}) = \sum_i v_1(\mathbf{r}_i) + \sum_i \sum_{j>i} v_2(\mathbf{r}_i, \mathbf{r}_j) + \sum_i \sum_{j>i} \sum_{k>j} v_3(\mathbf{r}_i, \mathbf{r}_j, \mathbf{r}_k) + \dots.$$

Here the first term  $v_1(\mathbf{r}_i)$ , represents the effect of an external field acting on a single particle of the system; the remaining terms represent inter-particle interactions. Besides the subdivision into many-body terms, another useful distinction among the contributions of the potential, involves the distinction between the intra-molecular and inter-molecular (if one deals with molecular structures) parts, which reflects the different nature of bonded and non-bonded interactions. We defer the detailed explanation of the force field used in our system to Secs. 3.3.3, 3.3.4. According to classical mechanics, the force on the  $i$ -th atom is derived as the gradient of the total potential with respect to atomic displacement:

$$(9) \quad \mathbf{F}_i = -\nabla_{\mathbf{r}_i} V(\mathbf{r}_1, \dots, \mathbf{r}_N).$$

Once we know the starting positions and the forces which act upon the atoms we can integrate the Newton's equations of motion

$$(10) \quad m_i \ddot{\mathbf{r}}_i = \mathbf{F}_i(\mathbf{r}_1, \mathbf{r}_2, \dots, \mathbf{r}_N)$$

to reconstruct the trajectories of the particles over, in principle arbitrarily long, space-time paths. The engine of a MD program is its time integrator algorithm which allows to follow step by step positions, velocities and forces in time; we discuss an example in Sec. 3.2.1 below. Typically an integrator-algorithm is based on a backbone scheme of the type:

- **step 1** : start with an initial atomic configuration and initial velocities;
- **step 2** : compute the inter-atomic forces for the current configuration;

- **step 3** : update the atomic positions and velocities according to the integration algorithm;
- **step 4** : iterate **step 2** and **step 3**  $N_{step}$  times, until  $N_{step} \cdot \Delta t$  equals the desired total simulation time.

In a MD calculation, most computer time is usually spent in computing the forces, i.e. for **step 2**. Since we usually deal with a rather large number of particles, it is certainly feasible to compute the force acting upon an atom produced by all other particles. The first procedure developed to overcome this problem, is to truncate short-ranged and long-ranged (two-body term) interactions at a cutoff value  $r_{cut}$ , see Sec. 3.3. This way all faraway particles do not contribute to the net force acting on the  $j$ -th atom, but only those contained within a sphere of radius  $r_{cut}$ . Moreover, to minimize the number of distance evaluation in a MD loop, one can take advantage of the so called Verlet list algorithm [39]. The cutoff sphere is now surrounded by another spherical crown of width  $\Delta r$ , so that the arbitrary  $j$ -th atom is itself surrounded by a sphere of radius  $r_{cut} + \Delta r$ . All the particles contained there, are stored as a list of neighbors of particle  $j$ . The inter-particle contributions to  $\mathbf{F}_j$  are computed only for atoms in the present list. If the difference  $\Delta r$  is chosen properly, for quite a few time steps there is no need to refresh the neighboring list, an operation whose CPU workload scales as  $O(N)^2$ : this method saves substantial computer time.

Temperature is an important quantity for a generic system, it is indeed crucial to be able to measure and control it. The measurements of the physical quantities for a system of point charges in motion is a characteristic problem of statistical physics. To evaluate the thermodynamic temperature we use the equipartition principle of classical mechanics which states

$$(11) \quad \langle K \rangle = \frac{1}{2} \left\langle \sum_{i=1}^N \frac{\mathbf{p}_i^2}{m_i} \right\rangle = \frac{1}{2} g k_B T$$

where  $T$  is the desired thermodynamic temperature,  $k_B$  is the Boltzmann constant,  $g$  is the number of degrees of freedom, i.e.  $3N - N_c$ , where  $N$  is the number of atoms free to move in the system, and  $N_c$  is the total number of independent internal constraints. It is thus convenient to define an instantaneous “kinetic temperature” function:

$$(12) \quad T(t) = \frac{2K(t)}{gk_B} = \frac{1}{gk_B} \sum_{i=1}^N \frac{\mathbf{p}_i^2(t)}{m_i}.$$

These relations represent the basic link between classical dynamics and thermodynamics.

It is thus clear how the mechanical formulation of MD can be recast in a statistical-mechanic formulation. The set of instantaneous particle positions  $\{\mathbf{r}_1, \mathbf{r}_2, \dots, \mathbf{r}_N\}$  and momenta  $\{\mathbf{p}_1, \mathbf{p}_2, \dots, \mathbf{p}_N\}$  defines a unique microstate  $\Gamma(t)$  in the  $6N$ -dimensional phase space of the system. Generating trajectories is therefore equivalent to generate the time evolution of the microstate  $\Gamma(t)$  in the corresponding phase space. Statistical mechanics tells us how to relate a macroscopic physical property to the instantaneous values that the observables experience during the evolution of the system. Indeed, as we have already said, we can compute the value  $A(t) = A(\mathbf{r}(t), \mathbf{p}(t))$  assumed by an observable

$A$  when the system is in a given microstate  $\Gamma(t)$ , and define the macroscopic value  $A_{macro}$  to be the time average  $\langle A(t) \rangle_t$ , assuming ergodicity [39]. In a MD run at constant time step  $\Delta t$  we thus have

$$(13) \quad A_{macro} = \langle A(t) \rangle_t \simeq \frac{1}{N_t} \sum_{k=1}^{N_t} A(t_k)$$

where  $k$  is an index running over the  $N_t$  equally spaced time steps. We have discussed so far the standard MD scheme, where simulations are performed in the microcanonical ensemble, or NVE ensemble, where the number of particles, the volume and the total energy are conserved and are constant quantities.

It is sometimes more appropriate to consider a situation where the system is in contact with a “heat-bath” environment, which exchanges heat and establishes temperature to an external fixed value  $T$ . In the limit of infinite size this approach environment and the NVE ensemble would yield equal results, but for the relatively small number of particles involved in current MD simulations, and in particular for time-dependent external potentials as the one considered in the present thesis, a control of temperature is highly desirable. We will therefore use a fixed temperature thermodynamical ensemble. We use an implementation of fixed-temperature MD scheme, involving extra dynamical variables, which causes the modification of the Newton’s equation of motion as discussed in Sec. 3.2.2. From a statistical point of view, we are dealing with the canonical ensemble, or NTV ensemble, where the number of particles, the volume, and the temperature are conserved quantities.

**3.2.1. The Verlet-leapfrog integrator algorithm.** The engine of a MD program is its time integrator algorithm. Time integration algorithms are developed for finite discrete integration techniques. These methods, which are usually known as finite-difference methods, are based on the discretization of the time continuum into a point grid where the points are separated by a fixed or variable reciprocal time distance  $\Delta t$ . In principle, knowing the position and velocities at time  $t$ , one is able to recreate the same quantities at time  $t + \Delta t$ . Time evolution is ensured by the iteration of this procedure. For sure, all these methods are approximate, and do not reconstruct the exact trajectories of the particles in a MD simulation because of the finite- $\Delta t$  and round-off errors; however, it is possible to minimize at least the discrete-time errors with appropriate tricks which mark the difference among the various algorithms. In our simulations we use the *leapfrog* (LF) algorithm [40, 41] which is an implementation of the Verlet algorithm [42, 41], which is an algorithm based on a fixed  $\Delta t$ . It requires values of the positions  $\mathbf{r}$  and forces  $\mathbf{f}$  at time  $t_i$ , while the velocities  $\mathbf{v}$  at half a time-step  $\Delta t$  behind. The output velocities are evaluated always at half-integer time-steps  $t_i + \frac{1}{2}\Delta t$ ,

$$(14) \quad \mathbf{v}(t_i + \frac{1}{2}\Delta t) = \mathbf{v}(t_i - \frac{1}{2}\Delta t) + \frac{\mathbf{F}(t_i)}{m}\Delta t$$

and are used to compute new positions at integer time-steps  $t_i + \Delta t$ ,

$$(15) \quad \mathbf{r}(t_i + \Delta t) = \mathbf{r}(t_i) + \mathbf{v}(t_i + \frac{1}{2}\Delta t)\Delta t.$$

A problem with this version of the Verlet algorithm is that velocities are not evaluated at the same time  $t$  of the positions and forces. The evaluation at the same times of velocities, positions and forces is necessary to compute the kinetic energy  $K$ , which is necessary to test, for example, the conservation of the total energy  $U = K + V$ , or other velocity-dependent quantities. The velocity at time  $t_i$  is thus obtained from average of the velocities half a time-step on either side of time  $t_i$ :

$$(16) \quad \mathbf{v}(t_i) = \frac{1}{2} \left[ \mathbf{v}(t_i - \frac{1}{2}\Delta t) + \mathbf{v}(t_i + \frac{1}{2}\Delta t) \right].$$

Since the leapfrog algorithm is derived from the Verlet algorithm, it gives rise to identical trajectories with the same order  $O(\Delta t^4)$  in the finite-step (truncation) local error of the positions; on the other hand, the local error on the velocities is improved from  $O(\Delta t^2)$  to  $O(\Delta t^3)$ . In MD simulations, the global error is the cumulative error over an arbitrary interval of time  $T = n\Delta t$ , and it is typically more important than the local error. The Verlet (basic and leapfrog) integrator has got a global error in position and velocity which is a  $O(\Delta t^2)$ , and is, therefore, known as a second-order integrator.

**3.2.2. Nosé - Hoover thermostat.** In our work, we simulate a canonical (NVT) ensemble which allows energy exchanges with the external environment and in which the number  $N$  of particles, the volume  $V$  of the fundamental box, and the temperature  $T$  of the system are fixed. In order to ensure that the average temperature is maintained close to the requested one, we couple our system to a heat bath. When this is done, the equations of motion are modified, and the trajectories too. The production of NVT trajectories is done by introducing in our model a suitable thermostat which consists in an implementation of the integration LF algorithm introduced above [43]. In the present work, we adopt the Nosé-Hoover algorithm [44], which is capable of generating smooth, deterministic and time-reversible trajectories in the canonical NVT ensemble. In this scheme the Newton's equation of motion are modified to read:

$$(17) \quad \begin{aligned} \frac{d\mathbf{r}(t)}{dt} &= \mathbf{v}(t) \\ \frac{d\mathbf{v}(t)}{dt} &= \frac{\mathbf{F}(t)}{m} - \chi(t)\mathbf{v}(t), \end{aligned}$$

where  $\chi$  is an opportune friction coefficient, whose value is controlled by the first order differential equation:

$$(18) \quad \frac{d\chi(t)}{dt} = \frac{N_f k_B}{Q} (T(t) - T_{ext}).$$

Here  $Q = N_f k_B T_{ext} \tau_T^2$  is the effective inertia of the heat exchanges to the thermostat,  $\tau_T$  is a specified time constant related to the relaxation time towards the desired temperature,  $N_f$  is the number of degrees of freedom,  $T(t)$  is the instantaneous temperature of the system and is given by Eq. (12), and  $T_{ext}$  is the environment temperature, which is a controllable parameter. Nosé-Hoover thermostat with  $Q \rightarrow \infty$  generates a microcanonical ensemble, according to the vanishing of the friction coefficient in Eq. 17. Too large values of  $Q$  (loose coupling) cause a poor temperature control On the other hand, too small values (tight coupling) yields to a slow exchange of kinetic energy. In the present work we fixe  $Q$  by setting  $\tau_T = 0.1$  ps.

The Nosé-Hoover dynamics involves a conserved quantity derived from the extended Hamiltonian of the system, which, to within a constant, equals the Helmholtz free energy:

$$(19) \quad H_{NVT} = V + K + \frac{1}{2}Q\chi(t)^2 + \frac{Q}{\tau_T^2} \int_0^t \chi(s)ds.$$

In simulation one can verify how well conserved this quantity really is to check for the appropriateness of the value of  $\Delta t$  adopted in simulation.

### 3.3. The adopted force field

In this section we intend to describe in some detail the force field used in our simulations for the mica substrate and RTIL under consideration. In addition we introduce the potential function which mimics the presence of a spherical AFM tip.

As we have anticipated in Sec. 3.2, for a system of  $N$  particles with strong interactions, no two-body approximation is possible for the mutual interaction potential and many-body terms must be considered in the definition of a physical reliable potential function  $V(\mathbf{r}_1, \dots, \mathbf{r}_N)$ . Of course, suitable two-body terms  $v_2(\mathbf{r}_i, \mathbf{r}_j)$  represent an important contribution to the total potential. Van der Waals (VdW) and Coulomb interactions are non-bonded terms which belong to this class, depending on the relative distances of pairs of particles. In a virtually infinite system generated by the repetition of a super cell containing  $N$  objects, all the atoms should, in principle, interact with each other (and with the periodic repetition of themselves) in pairs to arbitrarily large distance. This implies the calculation of an infinite set of pairwise terms. It is therefore common use to treat all interactions as if their range of action were finite. In what follows we analyze how, and when, this is possible.

**3.3.1. Short-ranged interaction.** Significant differences exist between VdW and Coulomb interactions, indeed, while the VdW term is effectively short-ranged, the Coulomb term is long-ranged. Short-ranged interactions decay rapidly to 0 when the relative distance between the interacting particles goes to infinity, that is, fall faster than  $r^{-d}$  where  $d$  is the dimensionality of the system. This allows us to truncate the VdW interactions beyond an appropriate inter-atomic distance, that is, a spherical cut-off value usually indicated by  $r_{cut}$ . Even if the truncation error can be made arbitrary small by choosing a sufficiently large  $r_{cut}$ , the truncation of the potential must be done with care [41]. Since a lot of time is spent in calculating mutual forces, this procedure clearly saves a large amount of CPU time. Moreover, if we opportunely choose the dimensions of our simulation supercell so that  $r_{cut} < L_{box}/2$  in all the directions where PBCs are used, we satisfy the so-called *minimum image criterion*. This criterion sets that each atom in a simulation interacts at most with one closest image of the remaining particles in the system.

**3.3.2. Long-ranged interactions and Ewald sums.** Coulomb electrostatic interactions among atoms are of great importance. Unlike the non-bonded short-ranged VdW potential, this type of interaction is long-ranged, in the sense that its potential function decays very slowly as  $\propto r^{-1}$ . This fact rules out the possibility to adopt the

same treatment protocol, based on the minimum image criterion and on the direct truncation at a cut-off radius  $r_{cut} < L_{box}/2$  used for the short-ranged interactions, without introducing an unacceptable error. As a consequence, for an infinite periodic system, one cannot handle naively the calculation of the electrostatic energy via direct summation of Coulomb terms. It is quickly understandable how the need to evaluate the sum on infinite slowly decaying terms, with alternating signs, forces us to deal with a conditionally convergent series. The difficulty of these kind of series consists in their poor and slow convergence (assuming the hypothesis of convergence) plus the additional problem of a varying limit of convergence, depending on the rearrangement of the terms of the series, as demonstrated by the Riemann series theorem. The best approach for calculating the electrostatic interactions in a periodic system is the Ewald sum method [39, 41, 45]. The basic model for a neutral ( $\sum_i q_i = 0$ ) periodic system is a system of charged point ions mutually interacting via the Coulomb potential and repelling one another at short distances. The particles are assumed to be  $N$  located in a simulation box with volume  $V_0$ . Let us first consider a system with 3-D periodicity. We wish to compute the Coulomb contribution to the potential energy of the system,

$$(20) \quad U_{Coulomb} = \frac{1}{2} \sum_{i=1}^N q_i \phi(r_i),$$

where  $\phi(r_i)$  is the electrostatic potential at the position of ion  $i$ ,

$$(21) \quad \phi(r_i) = \sum'_{j, \mathbf{R}} \frac{1}{4\pi\varepsilon_0} \frac{q_j}{|\mathbf{r}_{ij} + \mathbf{R}|},$$

where the prime on the summation indicates that the sum runs over all periodic images and over all particles  $j$ , except  $j = i$  if the Bravais lattice vector  $\mathbf{R} = 0$ . The Ewald method deals with a Coulombic series by means of two amendments to the simple model described above.

Firstly each ion-atom  $i$  is effectively neutralized (at long range) by the superposition of a spherical Gaussian cloud of opposite charge centered on the ion;  $\rho_{Gauss}(r) = -\frac{q_i}{4\pi\varepsilon_0} \left(\frac{\alpha}{\pi}\right)^{\frac{3}{2}} e^{-\alpha r^2}$ . Here  $\sqrt{2\alpha}$  defines the Gaussian width and the choice of  $\alpha$  is determined by considerations of computational efficiency. The combined assembly of point ions and Gaussian charges produce a *real-space* contribution of the Ewald sum, which is now short ranged and treatable by the methods of short range interactions. How rapidly this term goes to zero depends on the value of  $\alpha$  in the screening charge distribution. We then correct for the introduction of the smearing Gaussian by adding a second set of Gaussian charges, this time with the same charges as the original point ions and again centered on the point ions, in order to nullify the effect of the first set of screening Gaussians. If we wish to compute the electrostatic energy at site of an arbitrary ion  $i$ , we should exclude the contribution of the charge  $q_i$  to the potential, of course. However, it is convenient to add the screening charge around ion  $i$  to the compensating charge distribution that we must subtract, because if we do so, the compensating charge distribution becomes a smoothly varying periodic function. In this way, the potential due to these Gaussians, can be obtained from Poisson's equation and can be solved as a Fourier series in *reciprocal space*. The complete Ewald sum requires

an additional correction, known as the self-energy correction, which arises from the inclusion of the compensating Gaussian acting at its own center, and which is a constant. In conclusion, Ewald's method replaces a poorly convergent series in real space by few rapidly converging series: one in real space and one in reciprocal space, plus a constant self energy correction.

For molecular systems, as opposed to systems simply made up of point ions, additional modifications are necessary if the force field excludes intra-molecular Coulomb interactions. In real space, the easiest way to account these corrections, is to omit these interactions. More difficult is the approach in the reciprocal space, where the effect of individual Gaussian charges cannot easily be extracted; as a consequence the correction is properly made in real space. It amounts to removing terms corresponding to the potential energy of an ion  $\ell$  due to the Gaussian charge on a neighboring charge  $m$  (or *vice versa*).

We are now ready to rewrite the Coulombic potential energy (20) in Ewald form:

$$(22) \quad U_{Coul} = \frac{1}{2V_o\epsilon_0} \sum_{\mathbf{k} \neq 0}^{\infty} \frac{e^{-k^2/4\alpha^2}}{k^2} \left| \sum_j^N q_j e^{-i\mathbf{k} \cdot \mathbf{r}_j} \right|^2$$

$$(23) \quad + \frac{1}{4\pi\epsilon_0} \sum_{n \leq j}^N c_{jn} \frac{q_j q_n}{r_{nj}} \text{erfc}(\alpha r_{nj})$$

$$(24) \quad - \frac{1}{4\pi\epsilon_0} \sum_{\text{molecules}} \sum_{\ell \leq m}^M (1 - c_{\ell m}) q_\ell q_m \left\{ \delta_{\ell m} \frac{\alpha}{\sqrt{\pi}} + \frac{\text{erf}(\alpha r_{\ell m})}{r_{\ell m}^{1-\delta_{\ell m}}} \right\},$$

where  $\text{erf}(t) = \frac{2}{\sqrt{\pi}} \int_0^t \exp(-u^2) du$  is the error function, and  $\text{erfc}(t) = 1 - \text{erf}(t)$  is the complementary error function. The term in row (22) is the Fourier series, the one in row (23) is the real-space term, the  $\delta_{\ell m}$  term in row (24) is the self-interaction term, and the final term accounts for the removal of intra-molecular interactions.  $N$  is the number of charges in the system,  $M$  is the number of atoms in a given molecule, while  $c_{\ell m}$  factor accounts for the excluded intra-molecular interactions, that is the atoms belonging to the excluded list, plus the rescaling for the dihedral inter-molecular interaction (see Sec. 3.3.3):

$$c_{\ell m} = \begin{cases} 0.0 & \text{if } n_b = 0, 1 \text{ or } 2 \\ 0.5 & n_b = 3 \\ 1.0 & n_b > 3 \end{cases}$$

where  $n_b$  is the number of bonds connecting the  $\ell$ -th and  $m$ -th atoms in the molecule. Moreover in Eq. (22)  $\mathbf{k}$  is a reciprocal-lattice vector defined as:

$$(25) \quad \mathbf{k} = k_1 \mathbf{u} + k_2 \mathbf{v} + k_3 \mathbf{w},$$

where  $k_1, k_2, k_3$  are integers, and  $\mathbf{u}, \mathbf{v}, \mathbf{w}$  are the reciprocal-space basis vectors. By following the rules which connect the real space and the reciprocal space, we have:

$$(26) \quad \mathbf{u} = 2\pi \frac{\mathbf{b} \times \mathbf{c}}{\mathbf{a} \cdot \mathbf{b} \times \mathbf{c}}$$

$$(27) \quad \mathbf{v} = 2\pi \frac{\mathbf{c} \times \mathbf{a}}{\mathbf{a} \cdot \mathbf{b} \times \mathbf{c}}$$

$$(28) \quad \mathbf{w} = 2\pi \frac{\mathbf{a} \times \mathbf{b}}{\mathbf{a} \cdot \mathbf{b} \times \mathbf{c}}$$

and

$$(29) \quad V_o = |\mathbf{a} \cdot \mathbf{b} \times \mathbf{c}|$$

where  $\mathbf{a}, \mathbf{b}, \mathbf{c}$  are the vectors defining the real space super-cell periodicity  $\mathbf{R} = n_1\mathbf{a} + n_2\mathbf{b} + n_3\mathbf{c}$ .

Till now, we have briefly exposed the Ewald procedure to transform a conditionally convergent series into two rapidly converging series plus a constant correction term. The detailed rate of convergence of both series is governed by the  $\alpha$  factor. We can understand the great advantage to deal with these objects when we have to run our calculations. The fast convergence of the two series allow us to reintroduce the short ranged potential protocol, based on the truncation of the series at a suitable cut-off radius both in real space series and in reciprocal space. Evaluation of the two sums is indeed truncated at  $r \leq r_{cut}^{ewald}$  and  $|k_1| \leq k_{max1}, |k_2| \leq k_{max2}, |k_3| \leq k_{max3}$  (in reciprocal space each direction acquires an appropriate cut off value); it is thus important that  $\alpha$  is chosen so that the contributions to the real space, and reciprocal space series are negligible for terms with  $r > r_{cut}^{ewald}$  and  $k > k_{max}$ . In the present work we always consider the cut-off value for the Ewald sum equal to the cut-off value for the short-ranged truncation. It is therefore possible to set  $r_{cut} = r_{cut}^{ewald}$ . Moreover, here  $k_{max}$  represents the cut off value of a chosen direction in the reciprocal space, replacing, for simplicity of the notation,  $k_{max1}, k_{max2}$ , and  $k_{max3}$ .

In practice, in order to control simultaneously the errors committed during the truncation in both the two spaces, it can be found that  $\alpha, r_{cut}, k_{max}$  are not independent. It is usual to regard one of them as pre-determined and adjust the two others accordingly. In the present work we always assume that  $r_{cut}$  is fixed for the given system. This also allows us to chose  $r_{cut}$  in order to take advantage of the minimum image criterion in real space, while infinite-range contributions are computed by the reciprocal-space sum. To benefit of the good efficiency of three-dimensional Ewald sum, we apply PBCs in all three directions, even when the system is intrinsically two-dimensional. The best way to do this, is to introduce PBCs along the third dimension by using a cell size, in the same direction, large enough so that the interactions between different images of the (intrinsically two-dimensional) system are negligible, but also not to large to spoil the convergence in reciprocal space. A thin liquid film onto a thin solid slab, with suitable super-cell parameters, suits well this kind of approach.

**3.3.3. Ionic liquid; AMBER, OPLS-AA based force field.** The choice of the theoretical model for the inter-atomic potential which governs the dynamics of the RTIL's atoms is of the greatest importance. The behaviour of the system is, indeed,

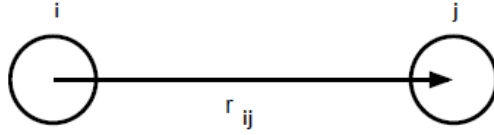


FIGURE 3.1. Two-body  $v_2(r_{ij})$  (bond) term of the total potential energy  $U_{12}$  (30)

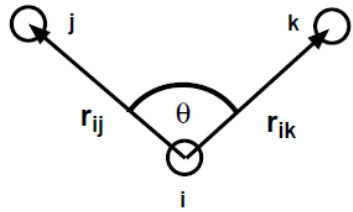


FIGURE 3.2. Three body  $v_3(r_i, r_j, r_k)$  (angular) term of the total potential energy  $U_{12}$  (31)

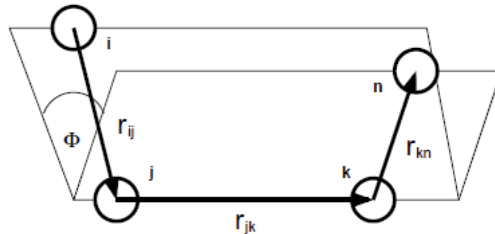


FIGURE 3.3. Four body  $v_4(r_i, \dots)$  (dihedral) term of the total potential energy  $U_{12}$  (32)

strongly dependent on this choice. In the molecular systems, interactions and bonding properties, are described in term of a number of appropriate analytical functions parametrized with different quantities in order to account for the specific properties of individual species considered. Typically the analytical forms and the parameter values have basis in chemical physics. As anticipated, this set of functions needed to define interactions and bonds is commonly known as force-field. Once marked its limits, a correct force field, allows to mimic the real systems as well as possible.

In this work we have decided to make use of the force-field which Pádua *et al.* have introduced to describe the behavior of compounds of the dialkylimidazolium cation family [31] and the bistriflimide anion family [46]. In these works, Pádua *et al.* have employed *ab initio* quantum-chemical calculations to obtain several parameters of the force-field that were not yet defined in literature, including molecular geometry, torsional energy profiles, and partial charge distributions. Their model is based on the OPLS-AA/AMBER general framework [47]. The total potential energy  $U_{12}$  of a pair

of molecular ions permits to understand fully which kind of bonds and interactions are considered in this force-field:

$$(30) \quad U_{12} = \sum_{b=1}^{N_{bonds}} \frac{k_b^r}{2} (r_b - r_b^{eq})^2$$

$$(31) \quad + \sum_{a=1}^{N_{angles}} \frac{k_a^\theta}{2} (\theta_a - \theta_a^{eq})^2$$

$$(32) \quad + \sum_{d=1}^{N_{dihedrals}} \sum_{m=1}^3 \frac{V_{m,d}}{2} [1 + (-1)^{m+1} \cos(m\phi_d)]$$

$$(33) \quad + \sum_i \sum_{j < i} \left\{ 4\varepsilon_{ij} \left[ \left( \frac{\sigma_{ij}}{r_{ij}} \right)^{12} - \left( \frac{\sigma_{ij}}{r_{ij}} \right)^6 \right] + \frac{1}{4\pi\varepsilon_0} \frac{q_i q_j}{r_{ij}} \right\} c_{ij}$$

where the first, the second, and the third contributions are the harmonic bond stretching, the harmonic bond bending, and the triple-cosine bond torsion intra-molecular terms respectively, while the last composite contribution represents the non-bonded VdW (Lennard-Jones form) and Coulombic terms. Moreover  $r_b = |\mathbf{r}_n - \mathbf{r}_m|$  ( $\mathbf{r}_n, \mathbf{r}_m$  are the positions of the two atoms involved in the bond  $b$ ),  $\theta_a$ , and  $\phi_d$  represent the intra-molecular bond length, bond valence angle and dihedral angle,  $r_b^{eq}, \theta_a^{eq}$  are the analogous equilibrium values, and  $k_b^r, k_a^\theta, V_{m,d}$  the corresponding energy parameters. We underline here that the harmonic constants  $k..$  for bond stretching and bending of the (30, 31) adopted in our work differ from corresponding constants in the OPLS-AA framework for a scale factor 2 (in OPLS-AA  $k..$  are used in place of  $k../2$ ), which is therefore compensated in the numerical values of the  $k..$  parameters. Finally,  $r_{ij} = |\mathbf{r}_i - \mathbf{r}_j|$  represents the inter-atomic distance for generic pairs of atoms,  $\varepsilon_{ij}$  and  $\sigma_{ij}$  the Lennard-Jones parameters, while  $q_i, q_j$  are the atomic charges.

The interaction between non-bonded atoms consists of a hard-core repulsion plus dispersive interaction terms represented by the Lennard-Jones 12-6 potential, plus an electrostatic term of partial point charges located at each atom center. The atomic partial charges are obtained from *ab initio* quantum calculations. These last contributions act between atoms in different molecules, but also between atoms within the same molecule separated by three bonds, i.e. for atoms interacting also via a torsion dihedral angle, and between sites separated by more than three bonds. We have therefore:

$$c_{ij} = \begin{cases} 0.0 & \text{for } i, j \text{ intra-molecular atoms separated by less than 3 bonds;} \\ 0.5 & \text{for } i, j \text{ intra-molecular atoms in 1,4-interaction;} \\ 1.0 & \text{for all atomic intermolecular interactions and remaining intra-molecular interactions.} \end{cases}$$

It has been found that the scale factor  $c_{ij}$  for the non-bonded interactions, which also compares in Eq. (24), is necessary to permit the use of the same parameters for inter- and intra-molecular interactions [47], and not to pervert the nature of the bonded interactions mimicked by the harmonic potentials. The summation of the non-bonded contributions extends over all pairs of atoms ( $i < j$ ) that satisfy the cutoff criteria

atoms	$m$ [amu]	$q$ [ $e$ ]	$\sigma_{ii}$ [\AA]	$\varepsilon_{ii}$ [kJ mol $^{-1}$ ]
C <sub>1</sub>	12.0110	-0.17	3.50	0.27614
C <sub>2</sub>	12.0110	+0.01	3.50	0.27614
C <sub>E</sub>	12.0110	-0.05	3.50	0.27614
C <sub>R</sub>	12.0110	-0.11	3.55	0.29288
C <sub>S</sub>	12.0110	-0.12	3.50	0.27614
C <sub>T</sub>	12.0110	-0.18	3.50	0.27614
C <sub>W</sub>	12.0110	-0.13	3.55	0.29288
H <sub>A</sub>	1.0080	+0.21	2.42	0.12552
H <sub>C</sub>	1.0080	+0.06	2.50	0.12552
H <sub>1</sub>	1.0080	+0.13	2.50	0.12552
N <sub>A</sub>	14.0070	+0.15	3.25	0.71128

TABLE 3.1. Atomic masses, partial charges, and LJ 12-6 parameters for the 1-butyl,3-methylimidazolium cation [bmim] $^+$ .

specified in the simulation algorithm as described in Sec. 3.3. The Lennard-Jones interactions between atoms of different type are parameterized using the geometric mean of the values reported in Table 3.1 and 3.2 for each single species. Thus, the distance and energy parameters for two atoms  $i$  and  $j$  are given by the mixing rule,

$$(34) \quad \sigma_{ij} = \sqrt{\sigma_i \sigma_j}$$

$$(35) \quad \varepsilon_{ij} = \sqrt{\varepsilon_i \varepsilon_j}.$$

We remark here that these formulae do not coincide with the more conventional Lorentz-Berthelot mixing rules (arithmetic and geometric mean rules for  $\sigma$  and  $\varepsilon$ , respectively).

Making use of the Pádua labeling of Fig. 1.2, in Tables 3.1, 3.2, 3.3, 3.4, 3.5, 3.6, 3.7, and 3.8 we summarize the parameters that we use in our simulations and which define completely the generic Eq. (30–33) for two molecules (and its extension for  $n$  molecules). The values reported are essentially those given in [31] and [46] for the 1-alkyl,3-methylimidazolium cation family (see Fig. 1.3) and for the bistriflimide anion (see Fig. 1.4). The main difference is that the cation C-H bonds are here considered with a harmonic parametrization taken from the AMBER force-field, while Pádua *et al.* keep the bond length constrained. The reason to treat those bonds as flexible is to avoid complications with the convergence of the constraints; anyway, this small detail will not affect our results appreciably.

**3.3.4. CLAYFF Force Field.** The choice of the theoretical model for the interatomic potential which governs the dynamics of substrate atoms, is at least as important as the RTIL case because, together with the RTIL force field, it is clearly responsible of the system behavior at the interface.

We have decided to make use of CLAYFF force field [48] which describes well the behavior of a wide range of clay minerals, including muscovite mica, and their interfaces with fluid phases. Moreover it is formally compatible with the AMBER force field for the RTIL. CLAYFF is based on ionic (non-bonded) description of the

atoms	$m$ [amu]	$q$ [ $e$ ]	$\sigma_{ii}$ [ $\text{\AA}$ ]	$\varepsilon_{ii}$ [kJ mol $^{-1}$ ]
C	12.1070	+0.35	3.50	0.27614
F	19.0000	-0.16	2.95	0.27614
N	14.0067	-0.66	3.25	0.27614
O	15.9994	-0.53	2.96	0.29288
S	32.0600	+1.02	3.55	0.27614

TABLE 3.2. Atomic masses, partial charges, and LJ 12-6 parameters for the bistriflimide anion  $[\text{Tf}_2\text{N}]^-$ .

bonds	$r^{eq}$ [ $\text{\AA}$ ]	$k^r$ [kJ mol $^{-1}$ $\text{\AA}^{-2}$ ]
$\text{C}_{R/W}\text{-H}_A$	1.080	1422.5
$\text{C}^*\text{-H}^*$	1.090	1422.5
$\text{C}_R\text{-N}_A$	1.315	3992.0
$\text{C}_W\text{-N}_A$	1.378	3574.0
$\text{C}_W\text{-C}_W$	1.341	4352.0
$\text{N}_A\text{-C}_1$	1.466	2820.0
$\text{C}^*\text{-C}^*$	1.529	2242.0

TABLE 3.3. Inter-molecular stretching parameters to substitute in Eq. (30), for the 1-butyl,3-methylimidazolium cation  $[\text{bmim}]^+$ .

bonds	$r^{eq}$ [ $\text{\AA}$ ]	$k^r$ [kJ mol $^{-1}$ $\text{\AA}^{-2}$ ]
C-F	1.323	3697
C-S	1.818	1970
S-O	1.442	5331
N-S	1.570	3113

TABLE 3.4. Inter-molecular stretching parameters to substitute in Eq. (30), for the bistriflimide anion  $[\text{Tf}_2\text{N}]^-$ .

metal-oxygen interactions associated with hydrated phases. All atoms are represented as point charges and are, in principle, allowed complete translational freedom within this force field framework. Metal-oxygen interaction are based on a simple, short range Lennard-Jones (12-6) potential

$$(36) \quad U_{LJ}(r) = 4\varepsilon \left[ \left( \frac{\sigma}{r} \right)^{12} - \left( \frac{\sigma}{r} \right)^6 \right],$$

where  $\sigma$  ( $= r_{min}/2^{\frac{1}{6}}$ ),  $\varepsilon$ , and  $r$  are, respectively, the zero, the depth of the function  $U_{LJ}$ , and the relative distance between two atoms, combined with the long range Coulomb potential with suitable empirical parameters, optimized on the basis of known mineral structures, and partial charges for all the atomic/ionic species. Partial charge assignment to the different atoms of interest, is extrapolated from detailed DFT quantum chemical calculations. VdW parameters and partial charges of each muscovite atomic

## 3. THE SIMULATION MODEL

angles	$\theta^{eq}$ [deg]	$k^\theta$ [kJ mol <sup>-1</sup> rad <sup>-2</sup> ]
C <sub>W</sub> -N <sub>A</sub> -C <sub>R</sub>	108.0	585.2
C <sub>W</sub> -N <sub>A</sub> -C <sub>1</sub>	125.6	585.2
C <sub>R</sub> -N <sub>A</sub> -C <sub>1</sub>	126.4	585.2
N <sub>A</sub> -C <sub>R</sub> -H <sub>A</sub>	125.1	292.6
N <sub>A</sub> -C <sub>R</sub> -N <sub>A</sub>	109.8	585.2
N <sub>A</sub> -C <sub>W</sub> -C <sub>W</sub>	107.1	585.2
N <sub>A</sub> -C <sub>W</sub> -H <sub>A</sub>	122.0	292.6
C <sub>W</sub> -C <sub>W</sub> -H <sub>A</sub>	130.9	292.6
N <sub>A</sub> /C <sup>*</sup> -C <sup>*</sup> -H <sup>*</sup>	110.7	313.2
N <sub>A</sub> /C <sup>*</sup> -C <sup>*</sup> -C <sup>*</sup>	112.7	418.4
H <sup>*</sup> -C <sup>*</sup> -H <sup>*</sup>	107.8	276.2

TABLE 3.5. Inter-molecular bending parameters to substitute in Eq. (31), for the 1-butyl,3-methylimidazolium cation [bmim]<sup>+</sup>.

angles	$\theta^{eq}$ [deg]	$k^\theta$ [kJ mol <sup>-1</sup> rad <sup>-2</sup> ]
F-C-F	107.1	781
S-C-F	111.8	694
C-S-O	102.6	870
O-S-O	118.5	969
O-S-N	113.6	789
C-S-N	100.2	816
S-N-S	125.6	671

TABLE 3.6. Inter-molecular bending parameters to substitute in Eq. (31), for the bistriflimide anion [Tf<sub>2</sub>N]<sup>-</sup>.

species are reported in Table 3.9. The non-bonded Lennard-Jones parameters are presented in term of a single atomic species to be combined in one of several ways to avoid the explicit definition for every possible atom-atom interaction in a simulation. The interaction parameters between unlike atoms are calculated according to the arithmetic mean rule for the distance parameter  $\sigma$  and to the geometric mean rule for the energy parameter  $\varepsilon$ ;

$$(37) \quad \sigma_{ij} = \frac{1}{2}(\sigma_i + \sigma_j)$$

$$(38) \quad \varepsilon_{ij} = \sqrt{\varepsilon_i \varepsilon_j}.$$

Oxygen charges vary, depending on their occurrence in bridging and substitution environments, from -0.95 e for hydroxyl oxygen (OH), to -1.05 e for a bridging oxygens (OB), to -1.1675 e for a bridging oxygen coordinated to tetrahedral substituted sites (OBTS). Here we consider tetrahedral aluminum (ALT) as the only substituent species in the T-O-T structure. The term bridging oxygen is here used to represent an edge-sharing polyhedra oxygen that is not part of a hydroxyl group.

dihedrals	$V_1$ [kJ mol $^{-1}$ ]	$V_2$ [kJ mol $^{-1}$ ]	$V_3$ [kJ mol $^{-1}$ ]
X-N <sub>A</sub> -C <sub>R</sub> -X	0.000	19.460	0.000
X-C <sub>W</sub> -C <sub>W</sub> -X	0.000	44.980	0.000
X-N <sub>A</sub> -C <sub>W</sub> -X	0.000	12.550	0.000
C <sub>W</sub> -N <sub>A</sub> -C <sub>1</sub> -H <sub>1</sub>	0.000	0.000	0.519
C <sub>R</sub> -N <sub>A</sub> -C <sub>1</sub> -X <sub>1</sub>	0.000	0.000	0.000
C <sub>W</sub> -N <sub>A</sub> -C <sub>1</sub> -C <sub>2/E</sub>	-7.154	6.106	0.794
C <sub>R</sub> -N <sub>A</sub> -C <sub>1</sub> -C <sub>2/E</sub>	-5.269	0.000	0.000
N <sub>A</sub> -C <sub>1</sub> -C <sub>2</sub> -C <sub>S/T</sub>	-7.480	3.164	-1.203
N <sub>A</sub> -C <sub>1</sub> -C <sub>2/E</sub> -H <sub>C</sub>	0.000	0.000	0.000
C*-C*-C*-H*	0.000	0.000	1.531
H*-C*-C*-H*	0.000	0.000	1.331
C*-C*-C*-C*	7.280	-0.657	1.168
X-N <sub>A</sub> -X-X	0.000	8.370	0.000
X-C <sub>W/R</sub> -X-X	0.000	9.200	0.000

TABLE 3.7. Inter-molecular torsional parameters to substitute in Eq. (32), for the 1-butyl,3-methylimidazolium cation  $[\text{bmim}]^+$ . C\* represents a generic aliphatic carbon: C<sub>1</sub>, C<sub>2</sub>, C<sub>E</sub>, C<sub>S</sub>, C<sub>T</sub>. H\* represents either H<sub>1</sub> or H<sub>C</sub>. Note that 1 kJ/mol=10.3643 meV =  $1.66054 \cdot 10^{21}$  J and 1 kJ/(mol · Å $^2$ )= $1.03643 \cdot 10^{-4}$  eV/Å $^2$ =0.166054 N/m.

dihedrals	$V_1$ [kJ mol $^{-1}$ ]	$V_2$ [kJ mol $^{-1}$ ]	$V_3$ [kJ mol $^{-1}$ ]
F-C-S-O	0.0000	0.0000	1.4520
S-N-S-O	0.0000	0.0000	-0.0150
F-C-S-N	0.0000	0.0000	1.3220
S-N-S-C	7.8327	-2.4904	-3.1950

TABLE 3.8. Inter-molecular torsional parameters to substitute in Eq. (32), for the bis triflimide anion  $[\text{Tf}_2\text{N}]^-$ . Note that 1 kJ/mol=10.3643 meV =  $1.66054 \cdot 10^{21}$  J and 1 kJ/(mol · Å $^2$ )= $1.03643 \cdot 10^{-4}$  eV/Å $^2$ =0.166054 N/m.

Species	Symbol	charge [e]	$\varepsilon$ [kJ/mol]	$\sigma$ [Å]
hydroxyl hydrogen	H	0.42500	-	-
hydroxyl oxygen	OH	-0.95000	-	-
bridging oxygen	OB	-1.05000	0.650182	3.165541
bridg. ox. tetrahedral substitution	OBTS	-1.16875	0.650182	3.165541
tetrahedral silicon	Si	2.1000	$7.700514 \cdot 10^{-6}$	3.302027
tetrahedral aluminium	AlT	1.57500	$7.700514 \cdot 10^{-6}$	3.302027
octahedral aluminium	AlO	1.57500	$5.563783 \cdot 10^{-6}$	4.271235
potassium	K	1.00000	0.418392	3.334010

TABLE 3.9. CLAYFF force field non-bonding Parameters

Harmonic-bonded terms are included explicitly in the force field to describe the bond stretch associated with hydroxyl groups. VdW interactions are excluded for bonded interactions; as consequence hydroxyl group species do not have got VdW parameters.

Nevertheless, in order to mimic a semi-infinite substrate which develops in  $z$  direction, we have decided to prepare our substrate by leaving free to move the most superficial atomic layers. K cations, O tetrahedral-basal oxygens, and Al-Si tetrahedral cations in the upper portion of the super-cell are indeed not fixed to account for the relaxation due to the abrupt truncation of the bulk periodicity in  $z$  direction and the interaction with the RTIL. On the other hand, we freeze the lowest muscovite layers at the side opposite to the RTIL, with the aim to simulate the presence of semi-infinite bulk below the surface, which imposes a relative rigidity and an overall periodicity to the whole structure. This simplification elides the problem of H atomic species of hydroxyl groups which are, therefore, kept fixed. This choice, reflects the necessity to mimic a semi-infinite structure maintaining as small as possible the number of degrees of freedom.

**3.3.5. The tip potential function.** In addition to the force field which governs the interactions among the atoms and the molecules of the system, we introduce an external potential in order to simulate a probing tip. In our intentions this probe should reproduce the tip of an atomic force microscopy (AFM) apparatus that “taps” into a RTIL layer deposited on a mica surface. We are interested in the analysis of the forces felt by this same probe along the  $z$  direction as an indicator of possible IL layering near the surface. We intend to compare the results with experiments [49, 36, 50]. It is clear that to simulate quantitatively a realistic AFM probe, a refined model including the microscopic structure of the tip would be needed. However the number of involved parameters should be very large, together with the fact that the detailed structure is not known in practice. As a first approximation, a probing tip characterized by an high symmetry, infinite mass and a small number of parameters such as a spherical geometry, guarantees an adequate starting point for our purposes. The functional form of the potential function for a spherical tip can be defined as:

$$(39) \quad V_{sphp}(r) = \frac{4\epsilon}{\alpha^2} \left\{ \frac{1}{\left[ (\frac{r}{\sigma})^2 - 1 \right]^6} - \alpha \frac{1}{\left[ (\frac{r}{\sigma})^2 - 1 \right]^3} \right\}, \quad r > \sigma,$$

where  $\epsilon$  is the energy parameter,  $\alpha$  is a pure number, and  $\sigma$  is the characteristic length which can be considered as the sphere radius. The resulting short-ranged interaction is weakly attractive in a thin region beyond the characteristic length  $\sigma$ , while rapidly acquires a repulsive-wall behaviour approaching  $\sigma$ , thus describing a nanometric excluded volume. In particular,  $\alpha$  governs the position of the minimum, its depth, and parametrizes also the range of action of the field. The range of the attractive part of  $V_{sphp}(r)$  decreases with increasing  $\alpha$ .

The size of the sphere is obviously restricted by the MD box. Indeed, due to PBCs the presence of the probing tip in the MD box under examination is repeated in all the other cells. For this reason we must avoid that each sphere overlap with the

others, and make sure that the minimum distance between two adjacent spheres is large enough thus these two spheres can be considered approximately as non-interacting. In our simulations  $\sigma$  is fixed at 1.6 nm, while  $\alpha = 10$  and  $\epsilon = 0.7$  kJ/mol are chosen so that we describe a spheric excluded volume with a thin attractive region outside it.

### 3.4. The model scheme

In the present study we investigate the interfacial layering of a  $\sim 4$  nm thick  $[\text{bmim}]^+[\text{Tf}_2\text{N}]^-$  film (see Sec.1.2) deposited onto a bulk-terminated muscovite substrate represented by a rectangular slab of area  $\sim 30.8$  nm<sup>2</sup> repeated in the  $xy$ -plane  $\sim 1$  nm thick. We simulate temperatures  $T = 300$  K and  $T = 350$  K by means of a Nosé-Hoover thermostat in the MD framework. Thanks to previous computational and experimental works [51, 49, 36] we expect some degree of structural organization of the RTIL near the substrate surface. In those works RTIL layering was found near the interface with several flat materials, with different degree of organization. In particular mica has been recognized as a substrate favorable to the creation of a layered-structure thanks to its easy cleavage, to the smoothness of the (001) plane, and to its low chemical reactivity. It has been also pointed out that steric effects, or excluded space regions for the motion of the ions, play an important role in the layering process. Unlike other works [52], in which steric effects are detailed investigated, here we focus on the electrostatic effects. This is done by replacing a generic wall potential, which should mimic the effects of the excluded region, with a more detailed atomistic description of the substrate. RTIL and muscovite substrate interact now via a microscopic atomic force field (see Sec. 3.3.3, 3.3.4). Here we couple the substrate and RTIL force fields by adopting the conventional Lorentz-Berthelot mixing rules (37) and (38). Layering is investigated through (i) a number and charge density analysis at the equilibrium, (ii) analysis of the produced average macroscopic fields, (iii) AFM probing.

We carry out MD simulations of a spherical tip of radius 1.6 nm penetrating the RTIL film with different approach velocities, as depicted in Fig. 3.4. The infinite mass spherical tip interacts with the atoms of the system via a simple wall potential described in Sec. 3.3.5, and is made descend into the RTIL film in small steps of 0.05 nm or 0.025 nm followed by suitable relaxations.

All simulations are performed in parallel using the DL\_POLY package ver. 2.20 after an appropriate scaling analysis of the simulation time as a function of the number of CPUs (see Appendix A). Calculations are always run through the Verlet-leapfrog integration algorithm (Sec. 3.2.1), by exploiting 3-D PBCs in a NVT ensemble with Nosé-Hoover thermostat (Sec. 3.2.2). Short- and long-ranged interactions are appropriately truncated with a cutoff value small enough to fulfill the minimum image criterion (see Sec.3.3.1). In particular, we adopt the Ewald approach, representing the electrostatic energy as the sum of real and reciprocal space contribution. The reciprocal space term consists of a sum over reciprocal lattice vectors  $\mathbf{k}$ , whose convergence is controlled by a Gaussian weight  $\frac{\exp -k/4\alpha^2}{k^2}$ . Terms are included up to a  $k_{max}$  such that the weight is lower than a set value (Sec. 3.3.2). A Verlet neighboring list is also used (see Sec. 3.2). The integration time-step is generally fixed at 1 fs, except where explicitly mentioned. All these generally fixed working conditions with the corresponding parameters are

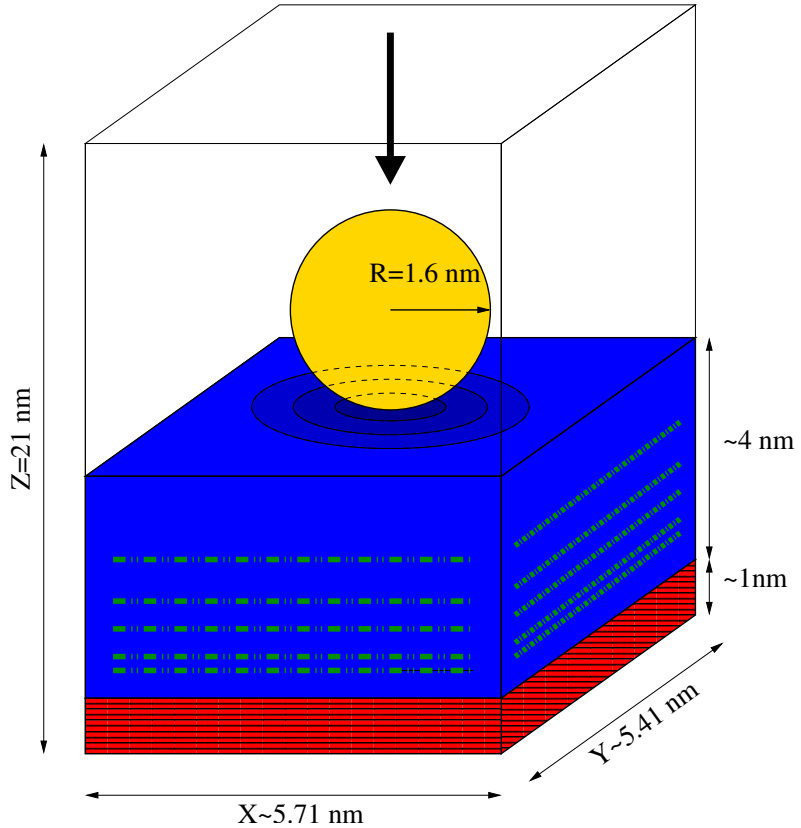


FIGURE 3.4. The scheme of the model system under consideration.

Integration algorithm	Verlet-leapfrog
PBCs	3-D
Thermodynamic ensemble	NVT
Thermostat	Nosé-Hoover ( $\tau_T = 0.1$ ps)
2-body interaction $r_{cut}$	12.0 Å
Ewald precision	$10^{-5}$
Verlet $\Delta r$	1.5 Å
integration time-step	1 fs

TABLE 3.10. Fixed working-environment conditions

summarized in Table 3.10. On the contrary, variable parameters, such as temperature and simulation time, are specified, where relevant, in the text.

### 3.5. System preparation

The starting RTIL of the present work is derived directly from a previous study in which the layering of a thin film onto a silica surface is investigated [51]. On the other hand, for the substrate, we build up a model muscovite structure as described in Chapter 2. First we prepare the isolated substrate.

We relax the mobile substrate layers with NVT simulations of approximately 4.5 ns at  $T = 350$  K. We are now ready to add in the RTIL film.

For the coupling process we follow two slightly different approaches for the neutral and charged substrate cases. In the first case we use a neutral RTIL whose initial configuration is taken from previous study and which is composed by 250  $[\text{bmim}]^+$ ,  $[\text{Tf}_2\text{N}]^-$  ion pairs from [51], while in the second case we use the same RTIL system with a random erasing of part of its anions so that it is now composed by 250  $[\text{bmim}]^+$ , and 234  $[\text{Tf}_2\text{N}]^-$  ions. The positions of the erased anions are chosen with a distribution as homogeneous as possible, in order to minimize the stress and the subsequent relaxation time; the number of erased anions equals the number of missing  $\text{K}^+$  in the muscovite layer thus to make the system RTIL-substrate globally neutral. The global neutralization, that in reality is achieved by ion exchanges with the system environment, cannot occur spontaneously in our canonical simulation. Removing ions by hands is apparently an ad-hoc procedure, but it achieves the aim of charge neutrality, a condition that is naturally enforced (see “perfect screening conditions”, Stillinger and Lovett) in every real system. Even though both the RTIL-substrate compound systems are globally neutral, we distinguish them with the names “charged”, and “neutral” referring to the net partial charge of the substrate.

The substrate  $xy$  super-cell is chosen slightly wider than the RTIL  $xy$  starting box which was appropriate for a silica substrate [51], but, at the same time, as similar as possible to it. The percentage difference among the in-plane sides of the two cells is  $a = 3.9\%$  for the  $x$  component, and  $b = 2.4\%$  for the  $y$  component. To get rid of the ensuing “trenches”, and to let the RTIL adapt to the mica surface, we place RTIL above the substrate surface with mobile atoms at a distance of  $\sim 4$  Å, and then perform an appropriate set of simulations at 350 K, within the MD box defined by the mica  $xy$  lateral size and  $z$  side  $c = 210$  Å. The RTIL fits the substrate lateral size by a rapid expansion in the  $xy$  plane.

Moreover, thanks to the relative small percentage difference between the incommensurate cells, the thickness of the RTIL layer, after this relaxation process, is only slightly reduced with respect to Ref. [51], and remains in the order of  $\sim 4$  nm. The basic MD box used for the present and subsequent simulations is replicated in 3-D with periodicity  $\approx 5.7 \times 5.4 \times 21.0$  nm<sup>3</sup>.

Since all these initial set of simulations follow important manipulations of the system, and since they are crucial for its subsequent relaxations, particular attention is paid in the choice of the time-step of the integration algorithm. Initially these simulations are carried out with a time-step which increases from 0.01 fs to 1 fs. This is necessary to allow the DL\_POLY package to integrate correctly the equations of motion of the particles which could experience strong forces due to important non-equilibrium conditions. Short simulations with short time-step are useful for a rapid and stable quenching of these forces. This can be verified by monitoring the accurate conservation of the conserved quantity (19) and the control of the temperature in an initial 1 ps long simulation, with time-step 0.1 fs, as reported in Fig. 3.5.

To reach a fairly well equilibrated liquid configuration, long simulations are then carried out with a regular  $\Delta t = 1$  fs. The conservation of the conserved quantity is

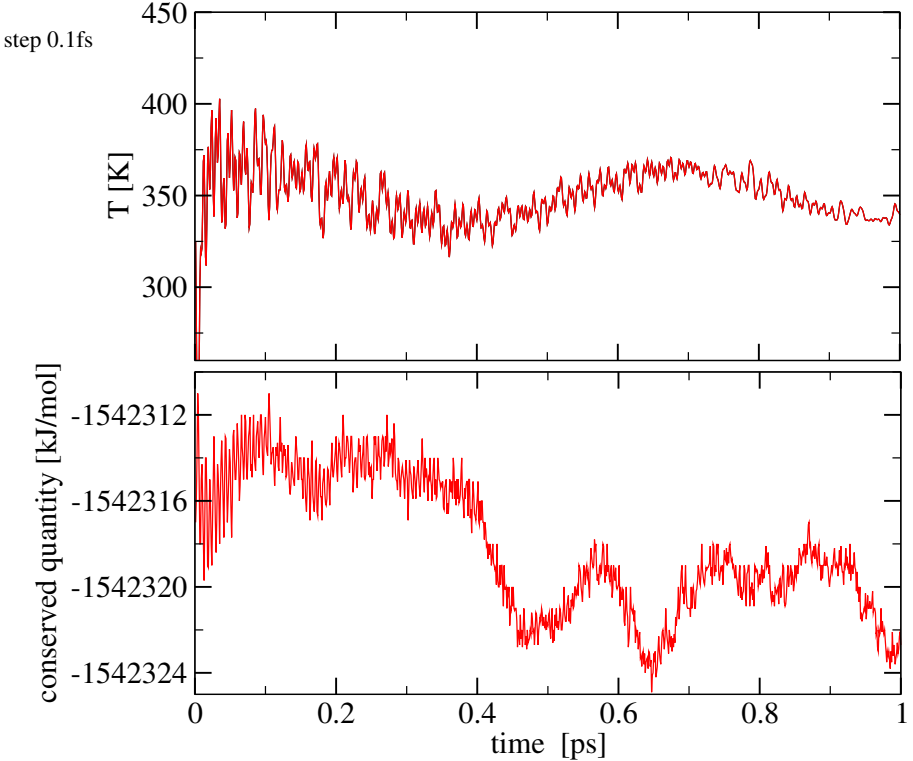


FIGURE 3.5. The transient condition of temperature  $T$  and of the Nosé-Hoover conserved quantity of Eq. (19) in the first picosecond of a relaxing simulation, with a reduced integration time-step of 0.1 fs.

now slightly worse as expected (see Fig. 3.6). The RTIL films onto the neutral- and charged-muscovite layers just created are then relaxed for a total length of 10 ns at 350 K. After this relaxation procedure, we run several consecutive simulations both in the neutral and in the charged cases. We thus create different starting configurations to generate independent samples. Two samples, whose starting configuration is obtained from the same simulation, are considered as independent if they are re-started as a “new” simulation (all previous statistical informations set to zero), and their starting configurations are separated in time by an appropriate interval, which is set to several hundreds of ps at  $T = 350$  K. This way we can suppose that the final sample is completely uncorrelated and carries little memory of the initial one. In the neutral case the total time covered by these consecutive simulations of data acquisition is of 20 ns, while in the charged case it is of 15 ns always at  $T = 350$  K.

We have carried out all the preparatory simulations at the temperature of 350 K, but we are eventually interested in the room-temperature properties of the RTIL film. Despite this,  $T = 350$  K is important because it can give us a useful comparison with room temperature properties, and also because all relaxation processes are faster at  $T = 350$  K than at  $T = 300$  K, thanks to the increased mobility for higher  $T$ . Starting from each independent samples we produce independent sample at  $T = 300$  K, by means of an appropriate “slow” cooling procedure. This procedure consists in performing

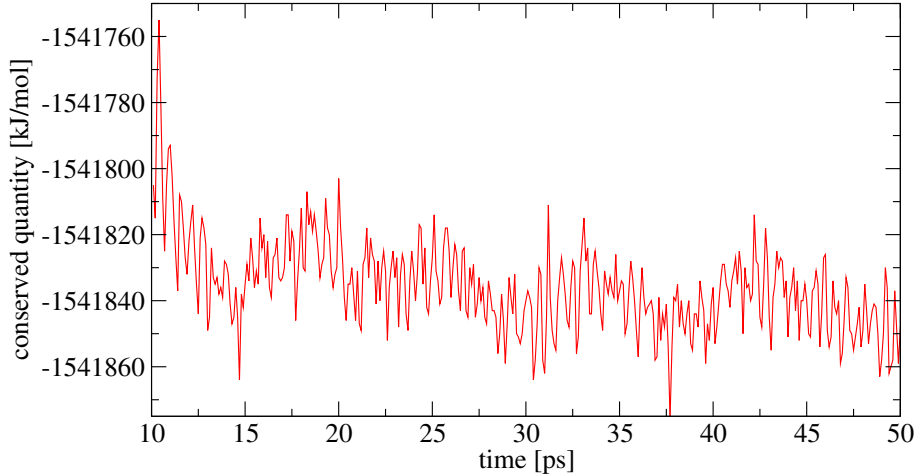


FIGURE 3.6. The transient condition of the Nosé-Hoover conserved quantity of Eq. (19) in few tens of ps during a relaxing simulation with a integration time-step of 1 fs.

Sample	intermediate $T$ [K]	simulation time [ns]
neutral 1	330	0.5
	310	1
	300	2
neutral 2	330	2
	310	3
	300	5
charged	340	2
	330	3
	320	3
	310	4
	300	10

TABLE 3.11. Annealing procedure from  $T = 350$  K to  $T = 300$  K.

successive simulations of the chosen starting sample at  $T = 350$  K with a decreased temperature and an increasing simulation time to allow for a correct relaxation of the system by compensating the decreasing mobility of the particles. In the neutral case this annealing procedure is carried out as reported in Tab. 3.11. This same Table also contains the gentler procedure used for the charged case. Here a greater number of intermediate temperatures are used with longer relaxation times. Due to the cost of the computation, while in the neutral case the procedure has been performed for two different independent samples at  $T = 350$  K, only one single sample has been produced in the charged case.



## CHAPTER 4

# Physical observables

In this section we provide the basic theoretical background about how we obtain several physical quantities and properties of interest, from the raw trajectories of the atoms in the system evaluated over appropriate time intervals. The data processing has required the development of specific scripts which use the output trajectories of the DL\_POLY package as input files. The detailed analysis and processed data is then described in the following chapter.

### 4.1. Average densities

In all surface phenomena, layering effects are crucial and can be detected by studying the  $z$ -dependence of the average number and charge densities of the particles in the system. Here we calculate the atomic number density  $n_{atom}(z)$ , the atomic charge density  $\rho_{atom}(z)$ , the number density of the ionic charge-centers  $n_{ion}(z)$ , and the charge density of the ionic charge-centers  $\rho_{ion}(z)$  for each ion species.  $\rho(z)$  is calculated like a number density with the single atomic partial charge used as statistical weight.

Since ions are in fact molecular units and not point charges, and since we deal with a finite MD box, special care must be paid when calculating the charge-center of the molecules placed across contiguous boxes, in order to avoid the problem of a fictitious “breaking” of these border molecules. The maximum distance between atoms in the same ions,  $\sim 10 \text{ \AA}$  for  $[\text{bmim}]^+$  and  $\sim 6 \text{ \AA}$  for  $[\text{Tf}_2\text{N}]^-$ , is small if compared with the box size, so it can be taken as a reference to “reconstruct” the correct relative positions of the atoms of a given ion. Indeed, if the distance between two atoms in the same molecule happens to be longer than this reference distance, one of them is translated to the proper adjacent box, so that the center of charge of the ion is restored correctly.

We are now able to obtain the average densities described above. We divide the simulation box into thin slabs of height  $\Delta h = 0.3 \text{ \AA}$  and volume  $\Delta V = \Delta h \cdot A$ , where  $A$  is the  $xy$  in-plane area of the box. For each  $i$ -th thin slab positioned at height  $z = \Delta h(i - 1/2)$  we compute the number of particles contained at each simulation time step. We then obtain the average density  $n(z)$  at discrete heights  $z$  by dividing these quantities by  $\Delta V$  and the number of time frames in the simulation. The charge density  $\rho(z)$  is computed like the number density with the atomic or ionic partial charge used as weights in the computation of the histograms.

### 4.2. Electric field and electric potential

We are interested in the electrical field and electrical potential across the layer generated by the average atomic charge density of the system as one moves along the  $z$

axis, focusing our attention in particular to the mica-RTIL interface. To obtain these quantities we proceed by solving the Poisson equation

$$(40) \quad \nabla^2 \phi(xyz) = -\frac{\rho(xyz)}{\varepsilon_0},$$

or alternatively the Maxwell equation

$$(41) \quad \nabla \cdot \mathbf{E}(xyz) = \frac{\rho(xyz)}{\varepsilon_0},$$

where  $\varepsilon_0$  is the vacuum permittivity,  $\rho(xyz)$  the charge density,  $\phi(xyz)$  the electric potential, and  $\mathbf{E}(xyz)$  the electric field. We can now make some useful approximations to transform this 3-dimensional differential equation into a 1-dimensional equation. We firstly take advantage of the 3-D periodic boundary conditions (PBCs) of our finite system. Simultaneously we solve Eq. (40) by using the average atomic charge density introduced in the previous section. We are in practice smearing out the charge dependency on  $x$  and  $y$  or, equivalently, replacing the atomic point charges  $q_i$  with 2-D charge planes  $q_i \delta(z - z_i)$  extending infinitely in the horizontal plane. This way, the investigated system acquires an effective translational invariance along the  $xy$  plane. From the physical point of view, we are indeed assuming that the electric field and potential depend only on the  $z$  coordinate. Equations (40, 41) become:

$$(42) \quad \frac{d^2 \phi(z)}{dz^2} = -\frac{\rho(z)}{\varepsilon_0},$$

$$(43) \quad \frac{dE_z(z)}{dz} = \frac{\rho(z)}{\varepsilon_0},$$

where  $\rho(z)$  is the atomic average density  $\phi(z)$  is the average potential,  $E_z(z)$  the average electrical field all evaluated in the  $\hat{z}$  direction of the cell.

If we consider  $z_{min}$  as the minimum  $z$  value, and  $z_{max}$  as the maximum  $z$  value for a super-cell, remembering that  $E_z(z) = -\frac{d\phi}{dz'} \Big|_z$ , then the generic solutions for the two equations (43, 42), are:

$$(44) \quad E_z(z) = \int_{z_{min}}^z \frac{\rho(z')}{\varepsilon_0} dz' + E(z_{min})$$

$$(45) \quad \phi(z) = \phi(z_{min}) + (z - z_{min}) \frac{d\phi}{dz'} \Big|_{z_{min}} + \int_{z_{min}}^z \int_{z_{min}}^{z'} -\frac{\rho(z'')}{\varepsilon_0} dz'' dz'.$$

Using the integral properties (integration by parts), we can also rewrite the last term of the (45) in a more compact way so that the entire (45) equation can be written in the simpler form:

$$(46) \quad \phi(z) = C + (z - z_{min})D + \int_{z_{min}}^{z_{max}} (z' - z_{max}) \frac{\rho(z')}{\varepsilon_0} dz',$$

where,  $C = \phi(z_{min})$ , and  $D = \left. \frac{d\phi}{dz'} \right|_{z_{min}}$ . PBCs implies that the physical quantities are equal at the super-cell boundary:

$$(47) \quad E(z_{min}) = E(z_{max}),$$

$$(48) \quad \phi(z_{min}) = \phi(z_{max}).$$

Relation (47) implies the equality between the first derivatives of the potential evaluated at the boundary and establishes the condition of charge neutrality within the super-cell. Relation (48) instead, determines the exact coefficient of the linear term of the electric potential (i.e. a global macroscopic electric field) for the case of PBCs along  $z$  axis,

$$(49) \quad (47, 48) \implies D = \left. \frac{d\phi}{dz'} \right|_{z_{min}} = \left. \frac{d\phi}{dz'} \right|_{z_{max}} = \frac{1}{(z_{min} - z_{max})} \int_{z_{min}}^{z_{max}} (z' - z_{max}) \frac{\rho(z')}{\varepsilon_o} dz'.$$

This choice is of course arbitrarily, since it depends explicitly on the size of the super-cell in the direction perpendicular to the substrate. It is probably better to consider the limit  $D = 0$  (i.e.  $z_{max} - z_{min} \rightarrow +\infty$ ).

In summary, the exact solutions (44), (46) of equations (41), (40) allow us to compute the  $z$  dependence of the electric field  $E_z$  given the charge density distribution  $\rho(z)$ . The potential is determined up to an arbitrary constant  $C$ , which can be put equal to 0 for simplicity.

In the next chapter, the  $E_z(z)$  field and  $\phi(z)$  potential functions are computed by numerical integration of the averaged atomic charge density  $\rho(z)$  by means of a script written in python language.

The potential drop across the film measures the interface average dipole. It is well known that an IL in contact with a solid substrate can form a charged double layer. This structure is responsible for a net electrostatic potential drop, since a charged particle would experience a finite electric force while crossing it.

### 4.3. Evaluating the local electric field

In the present work we are interested in evaluating the force acting on a spherical tip immersed in a ionic liquid due to the steric effects imposed by the tip itself on the moving ions in the liquid. Compared to ordinary liquids, ILs are composed of free ions which, in principle, could create a non-negligible electric field in the region of the tip. How strong the local field is depends on the configuration of the system analyzed. In Sec. 4.2 we have discussed a means to compute the mean  $E_z$  field for the RTIL film at equilibrium. Here we intend to study and evaluate its possible value in the region occupied by the tip while it penetrates inside the film. This calculation allows us to estimate the effects of electric forces on an hypothetical charged tip. In our system, indeed, the tip is simply described by a continuous, spherically symmetric potential (“wall potential”) which excludes RTIL atoms from a mesoscopic region of space. We are aware, however, that in reality any actual tip is very far from this idealized structureless description. First of all, a real tip is composed of real massive atoms structured as a solid. Moreover the tip is usually grounded or electrically connected so that it is

likely to carry a small unbalanced charge. It is not evident how the presence of this charge could eventually modify the total force felt by the tip immersed in the charged molecules. The best way to evaluate the combined effect of the wall- and electrostatic-potentials on this force, it would be to perform a complete simulation, for example with an added fixed charge at the center of the tip, to interact, with the ions of the liquid, via the Coulomb potential. That one would obviously be a poor approximation which would ignore all inhomogeneities, and all time variations of the charge on the surface of the probe, but can be thought as a fair starting point.

There is an even simpler approach, which allows us to avoid any new simulation. We evaluate the first-order approximation electrostatic effects on the “tip-force” by neglecting the effect of the tip charge on the RTIL dynamics. The first order approximation consists in evaluating the electrostatic field at the center of the tip, produced by the ions. Formally, this approximation is acceptable when the charge used is small enough to be considered as an infinitesimal test charge, so that linear response applies. The perturbing effects of the tip charge on the RTIL dynamics would produce a second-order effect, which we neglect.

The only difficulty in this approach is the evaluation of the point electric field. As we have already seen in section 3.3, the best way to evaluate the electrostatic field produced by a infinite set of point charges with 3-D PBCs, is the Ewald sum. We are however able to extract the  $z$  component of the electric field via a direct summation of Coulombic terms truncated at a suitable distance. First of all we neglect the  $z$  repetitions altogether, since they are unphysical in this intrinsically 2-D system. We then evaluate the approximate value of the  $z$  component of electric field, at an arbitrary point  $P$  in the liquid, by means of a real space summation of Coulombic terms in a single slab system with 2-D periodicity. As consequence we deal with a potential conditionally convergent series. We remind that, due to the Riemann series theorem, in order to guarantee a physical meaning to the numerical value obtained from this direct summation, it is necessary to verify that this series is unconditionally convergent. This can be done by demonstrating the absolute convergence of the series itself, which is a necessary and sufficient condition. Thanks to the fact that the series of the absolute values has no alternating signs, the order of summation is not determinant; we are therefore allowed to subdivide this total series into a finite number of different sub-series which can be studied separately. Each of these sub-series is constructed as the sum of the electric field produced by each point charge of the simulation box repeated in the  $xy$  plane with the 2-D PBCs. Indeed, each atom in the box produces a periodic grid in the  $xy$  plane constructed by the periodic images of itself. The images are positioned at each cross of the grid. To evaluate the field in the point  $P$  placed at a distance  $z$  from the infinite plane of the periodically repeated charges, the sub-series can be written as:

$$(50) \quad E(z) = \frac{q}{4\pi\varepsilon_0} \sum_{i,j}^{\infty} \frac{z}{((ia - x_p)^2 + (jb - y_p)^2 + z^2)^{\frac{3}{2}}},$$

where  $a$  and  $b$  are the lateral size of the repeated box in  $x$  and  $y$  directions,  $i$  and  $j$  here represent the index which take all integer values,  $x_p$  and  $y_p$  represent the coordinates of the evaluation point. Since the number of atoms in the box is finite, the last issue

to overcome, is to demonstrate the convergence of the sub-series just considered. Each of these sub-series converges to a finite value for  $E_z$ , not much different from the electric field generated, at the same point  $P$ , by an infinite homogeneous 2-D charge distribution. We can, therefore, subdivide each of our sub-series in two parts. The first term is a finite sum over a given number of atoms, typically those inside a circle of radius  $R_{cut}$  from the evaluation point. Thanks to the fact that this sum is finite, and the evaluation point  $P$  never coincides with a point charge position, this first contribution is finite. The second term is the sum over the other infinite point charges at a distance greater than  $R_{cut}$  from the evaluation point. We approximate this last contribution with the field generated by an infinite 2-D charge plane with an equivalent homogeneous superficial charge density  $\sigma = q/(ab)$ , and with a hole of radius  $R_{cut}$  centered on the vertical of the evaluation point  $P$ . It is clear that this approximation acts better and better when  $R_{cut} \gg \max(a, b, \tilde{z})$  so that, the integrand function has little changes over a 2-D cell with dimensions  $a \cdot b$ . The  $z$  component of the electric field of this last term can be obtained by means of the following convergent integral

$$(51) \quad \begin{aligned} E_z(\mathbf{r}_p) &= \frac{1}{4\pi\epsilon_0} \int_{xy\text{plane}} \sigma(\mathbf{r}') \frac{(\mathbf{r}_p - \mathbf{r}') \cdot \hat{\mathbf{z}}}{\|\mathbf{r}_p - \mathbf{r}'\|^3} d\mathbf{r}' = \frac{\sigma}{4\pi\epsilon_0} \int_0^{2\pi} \int_{R_{cut}}^{+\infty} \frac{zr}{(z^2 + r^2)^{\frac{3}{2}}} dr d\phi \\ &= \frac{\sigma}{2\epsilon_0} \frac{z}{\sqrt{z^2 + R_{cut}^2}} \end{aligned}$$

We have indeed demonstrated the convergence of the sub-series and, simultaneously, the absolute convergence of the starting series. This implies the unconditional convergence of the starting series, i.e., the independence of its limit of convergence from the arrangement of the summation terms.

Once established the unconditional convergence of the global series, we can compute its value of convergence by the sum of terms within a suitable cut-off value  $R_{cut}$ . As Eq. (51) suggests that the convergence properties of the truncated sum is rather poor, we can improve convergence of the total series, by means of an appropriate fitting of the sequence of the partial sums, as a function of the increasing number  $N_c \propto R_{cut}^2$  of image-cells considered around the fundamental box, Fig. 4.1. To do this, we assume implicitly a steady decay (that is, a fixed proportionality) of the truncation error after an adequate number of initial terms. Once again, we can justify this assumption on the basis of the partial sum sequence of the sub-series cited above. It is clear, indeed, that each partial sum sequence, in the limit of large  $N_c$ , is monotonically convergent to its limit of convergence. The details of the convergence depend clearly on the exact geometrical configuration of the charges with respect to the evaluation point, but it can be demonstrated that the residual error is approximatively proportional to  $R_{cut}^{-1} \propto N_c^{-\frac{1}{2}}$ . By using a fitting function of the type

$$(52) \quad f_{\alpha_i, \beta_i, \chi_i}(N_c) = \alpha_i + \frac{\beta_i}{\sqrt{N_c + \chi_i}},$$

where  $i$  identifies one atom in the box, and  $\alpha_i, \beta_i, \chi_i$  are free parameters, we have obtained that the sequences of the partial sums (as a function of the increasing number of the repeated cells around the box) converge, as expected, proportionally to the inverse square root; see Fig. 4.2. It can be useful to underline that the limit of convergence

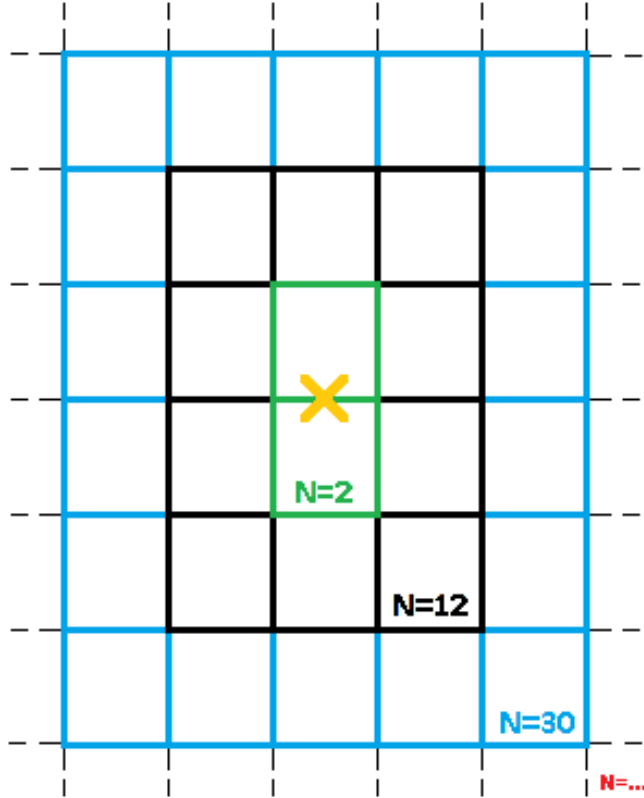


FIGURE 4.1. The scheme for increasing cells number around the seed cell in  $x$ - $y$  plane. The central “ $\times$ ” establishes the point of evaluation of the  $z$  component of the electric field. Since the evaluating point is located on the edge of our MD box, for reasons of symmetry on  $x$ - $y$  directions, we consider a double box as the seed for the step by step increasing of the image cells. Each step consists in the introduction of one new external belt of image cells, which surrounds the seed-cell already generated.

$\alpha_i$ , i.e. the extrapolated field, is of course positive or negative, depending on the sign of the atomic charge considered. It is then clear that the sum of terms with, stable asymptotic behaviors and similar degrees of convergence - in the limit of large  $N_c$  -

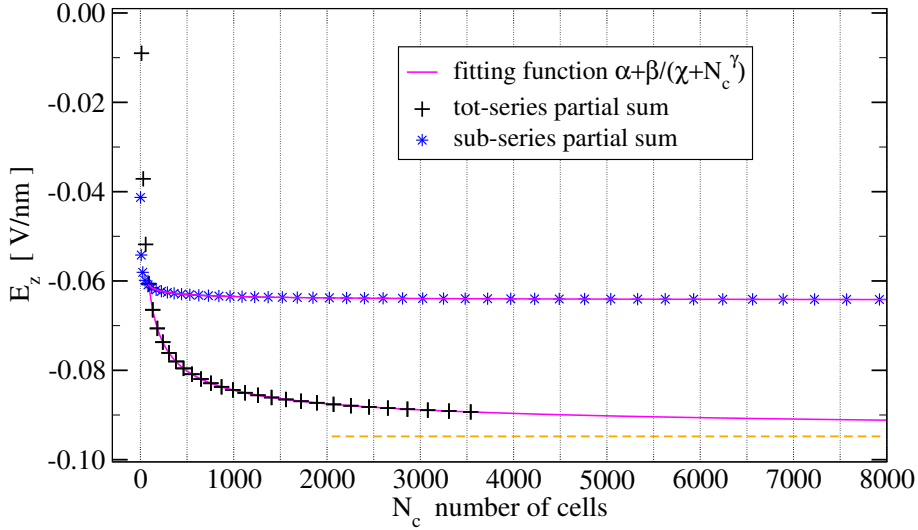


FIGURE 4.2. A double set of numerically computed values of the electric field at the center of a spherical tip positioned 36.5 Å above the mica surface at 300 K. Each point of both the two set of data represents the value of the electric field assumed by the partial sums of an infinite direct Coulomb summation at an increasing number of image cells around the tip center. Stars: the  $z$  component of the electric field obtained by a truncated sub-series generated by a single charge of  $q = -15e$  in the repeated box. The charge-value used here is chosen thus to give a direct visual comparison between the two set of data. Crosses: the  $z$  component of the electric field obtained by the truncated total series generated by the images of all the charged-atoms of a RTIL + mica configuration. Both sets of data converge with  $\gamma \approx 0.5$ . The bold lines represent the best fit function 52. The fit involves only data with  $N_c \geq 90$ . The dotted line defines the value of convergence for the fitting function of the plus-point data, here  $\alpha = -0.0947791$  V/nm.

reflects the proportionality of its terms as we can see from the following relation:

$$\begin{aligned}
& \alpha_1 + \frac{\beta_1}{\sqrt{N_c + \chi_1}} + \alpha_2 + \frac{\beta_2}{\sqrt{N_c + \chi_2}} + \dots + \alpha_N + \frac{\beta_N}{\sqrt{N_c + \chi_N}} \\
&= \alpha_1 + \alpha_2 + \dots + \alpha_N + \frac{1}{\sqrt{N_c}} \left[ \frac{\beta_1}{\sqrt{1 + \chi_1/N_c}} + \frac{\beta_2}{\sqrt{1 + \chi_2/N_c}} + \dots + \frac{\beta_N}{\sqrt{1 + \chi_N/N_c}} \right] \\
&= A + \frac{1}{\sqrt{N_c}} \left[ \beta_1 \left( 1 - \frac{\chi_1}{2N_c} + \frac{3\chi_1^2}{8N_c^2} + \dots \right) + \dots + \beta_N \left( 1 - \frac{\chi_N}{2N_c} + \frac{3\chi_N^2}{8N_c^2} + \dots \right) \right] \\
(53)= & A + \frac{1}{\sqrt{N_c}} \left( B + \frac{C}{N_c} + \frac{D}{N_c^2} + \dots \right)
\end{aligned}$$

where  $1, 2, \dots, N$  represent the atoms in the box. As a consequence, the sequence of the partial sums of the complete series, has got an asymptotic behavior which potentially

converges as  $N^{-\frac{1+2m}{2}}$  with  $m = 0, 1, 2, \dots$ , if the constants  $B, C, \dots$  vanish. The occasional vanishing of these constants corresponds to extremely symmetrical geometries of the point charges, which are not encountered in the present work. The characteristic convergence is therefore  $\propto N_c^{-\frac{1}{2}}$ . This allows us to extrapolate the  $z$  component of the electric field as the free parameter  $\alpha$  of a fitting function of the type reported in Eq. (52). Simultaneously we can also use  $\gamma$  of the fitting function of Fig. 4.2 as a control parameter to verify the validity of this approach. As we expect,  $\gamma$  is typically  $\approx 0.5$  for different test cases.

## CHAPTER 5

# Data processing and analysis

In this Chapter we report the results of our set of simulations performed in the framework of the MD technique discussed in Chapter 3 and Chapter 4. The physical quantities measured and analyzed here are obtained by means of suitable manipulations of the raw trajectories data through dedicated scripts in bash shell, AWK, and Python languages. The trajectories data are generated with the DL\_POLY package in a modified version following the procedure described in Sec. 3.4.

In the first part of this Chapter we analyze some static equilibrium properties of the pure RTIL thin film deposited onto neutral and charged muscovite layers, while in the second part, we focus our attention on the interaction of the film with a probing spherical tip approaching the muscovite surfaces through a step by step lowering (the indentation process).

### 5.1. IL number and charge densities

We analyze the number densities of atoms and of whole molecular ions in the RTIL. We also compute the charge densities to better characterize the film properties in real space. We report the interfacial organization of the RTIL onto the muscovite for the neutral and charged case at temperatures of  $T = 350$  K and  $T = 300$  K obtained from simulations performed according to the protocol established in Sec.3.4. The total simulation time is fixed to 15 ns and is equal for each of the cases we considered. In what follows, the vertical position of the particles is identified by the  $z$  coordinate measured relative to a reference surface corresponding to the topmost  $K^+$  plane in the muscovite slab.

Figures 5.1, 5.2, 5.3, 5.4 show the resulting profiles. First we see that both in the neutral and charged case the number density of atoms  $n_{atom}(z)$  develops some structure close to the surface. A double peak plus a second single peak within a distance of  $\sim 1$  nm above the reference surface are clearly visible. The double peak is essentially symmetric when the surface is neutral, and it acquires a more pronounced asymmetry in the charged case due to the necessity of compensating the unbalanced charge on the muscovite surface with a greater density of cations. Over the range  $1 \text{ nm} \geq z \geq 3 \text{ nm}$ ,  $n_{atom}(z)$  displays low-amplitude spatial oscillations, corresponding to low spatial ordering. At the RTIL free surface there is a peak which we analyze in detail in Sec. 5.1.1 below. The lowering of the temperature  $T$ , and the consequent decrease of the thermal fluctuations, should tend to promote the RTIL organization and the sharpness of the peaks. Despite this, the differences in  $n_{atom}(z)$  between same cases with  $T = 300$  K and  $T = 350$  K are not especially significant.

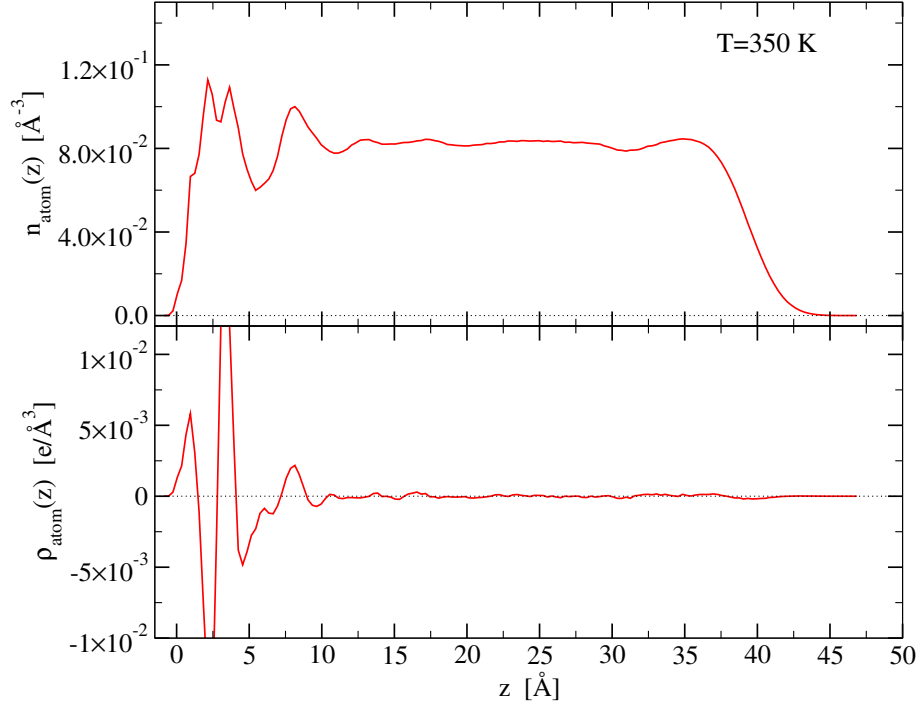


FIGURE 5.1. The RTIL atomic number and charge density profiles in the neutral case at 350 K.

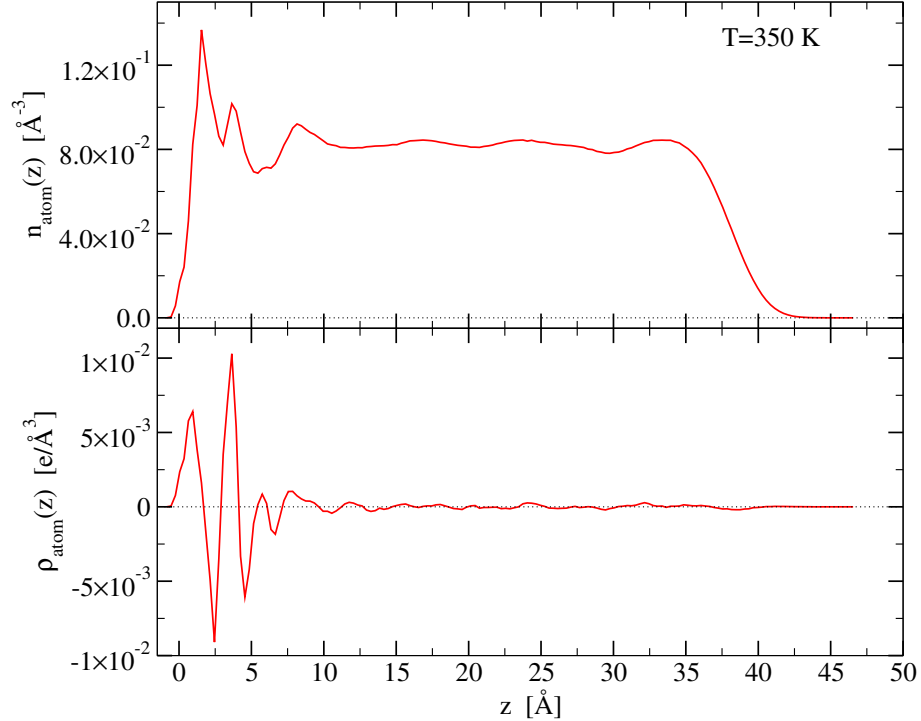


FIGURE 5.2. The RTIL atomic number and charge density profiles in the charged case at 350 K.

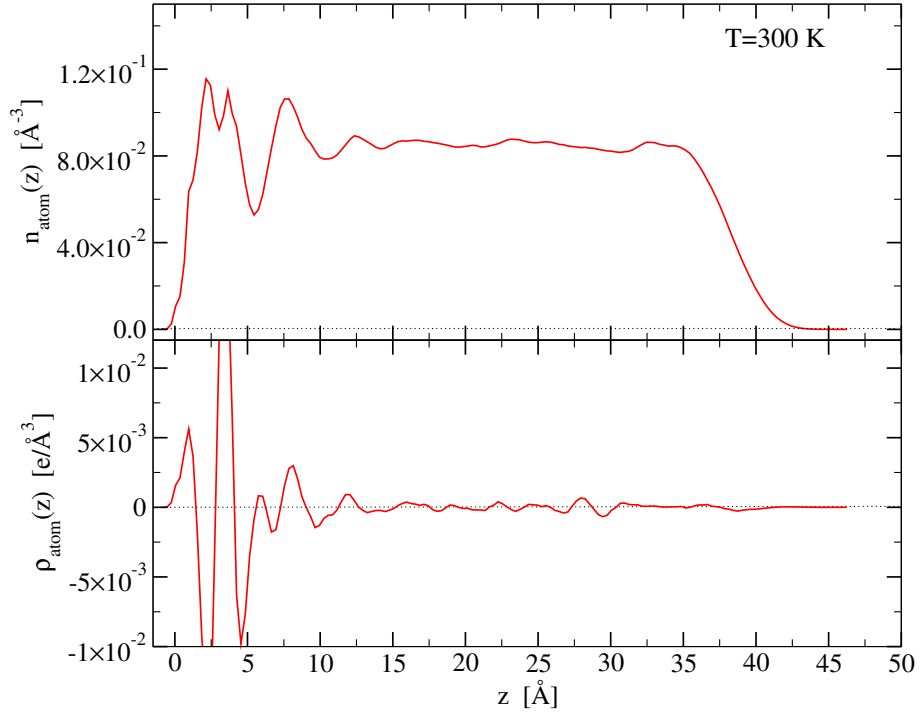


FIGURE 5.3. The RTIL atomic number and charge density profiles in the neutral case at 300 K.

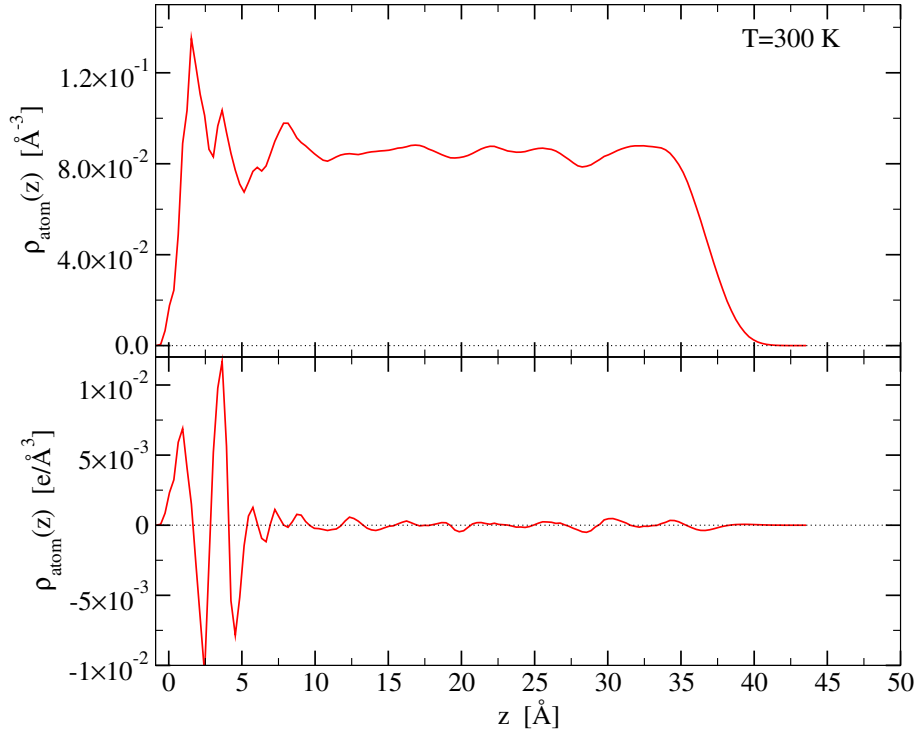


FIGURE 5.4. The RTIL atomic number and charge density profiles in the charged case at 300 K.

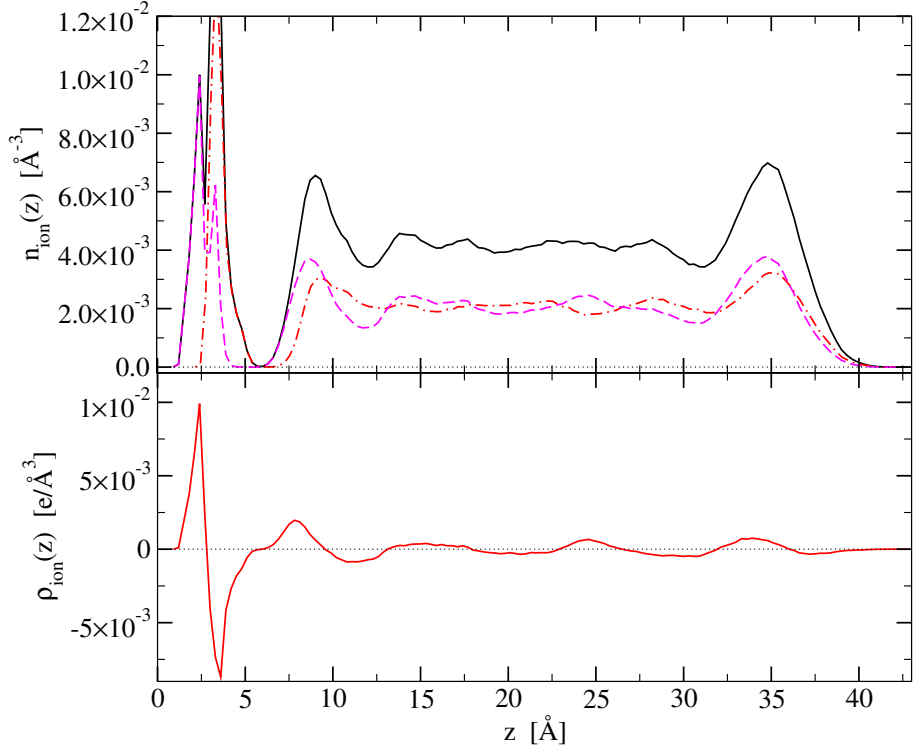


FIGURE 5.5. The ionic number and charge density profiles computed assuming that the charge of anions and cations are concentrated in point charges at the corresponding charge-center in the neutral case at 350 K.

Further information about the structuring of the thin RTIL film comes from the analysis of the number densities  $n_{ion}(z)$  of the ions shown in Fig. 5.5, 5.6, 5.7, 5.8. This density corresponds to the number density of the charge center of the ions. Here we can distinguish the cationic and anionic contribution to the different layers. In all the cases we studied, if we point our attention to the total ionic densities, the first double peak and the second single peak in the first  $\sim 1$  nm above the RTIL-muscovite surface, already visible in the atomic densities, are clearly identified. They confirm the strong layering of the RTIL close to the muscovite surface, and, if we move our attention to the anionic and cationic densities separately, they underline how the cations tend to create a first solvation layer followed by a second balancing anionic layer thus creating a surface electrostatic dipole. This is also supported by the analysis of the ion charge densities displayed in Fig. 5.5, 5.6, 5.7, 5.8. In the charged case the distance between these ionic layers, increased with respect to the neutral case, is a consequence of an inward displacement of the cation peak, and reflects the screening of the unbalanced charge of  $0.5 \text{ e}/\text{nm}^2$  localized onto the muscovite surface. Beyond the first double peak close to the surface there is a small region  $\sim 0.5$  nm wide with relatively few atoms, and nearly no ion charge-centers, which separates the strongly ordered region at close contact with muscovite from the rest of the liquid. This region is followed by a well visible second peak in the total density, while at increased values of  $z$ , we find rapidly damped oscillations in  $n_{ion}(z)$  which is always slightly enhanced by lowering

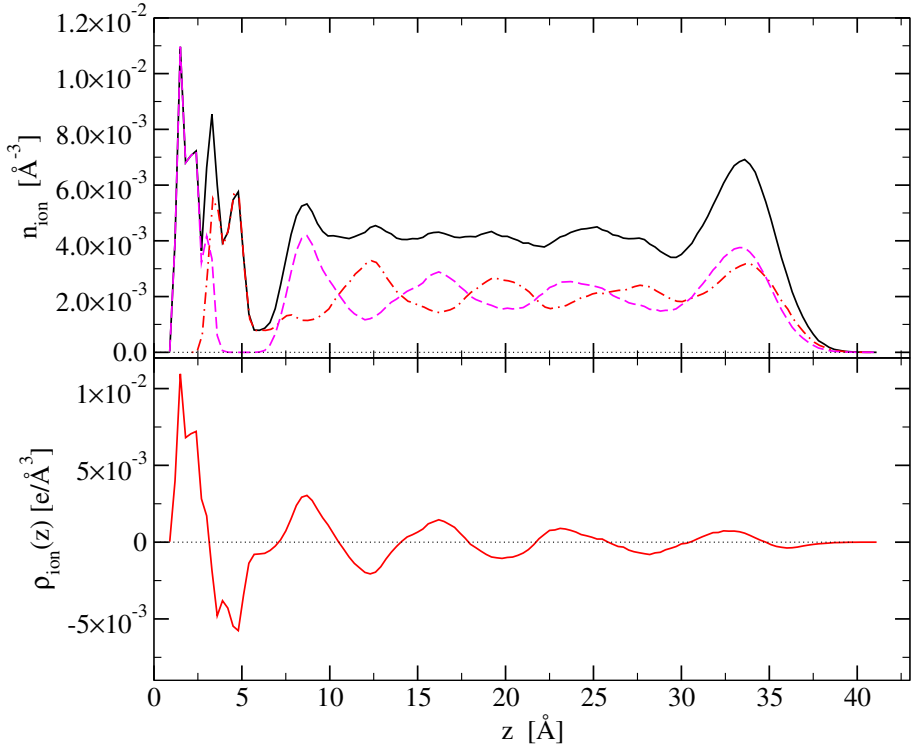


FIGURE 5.6. The ionic number and charge density profiles in the charged case at 350 K.

the temperature. Finally, we find a peak with a smooth tail at the [bmim][Tf<sub>2</sub>N] free surface. This density organization of the neutral case is comparable directly to that reported in Ref. [51] at 300 K and 350 K, and shows similarities in the numeric values for the peak height, even though our profile shows less defined peaks. A probable reason can be attributed to shorter simulated time, as described in Sec. 5.1.2, and different substrate.

We can then notice a significant difference between the neutral and the charged cases. In the neutral case we see a poorly-ordered layering in the total density produced by the summation of the anionic and cationic densities with low coordinated structures (especially at  $T = 300$  K). In the charged case the layering of the total density is only slightly enhanced, but anionic and cationic densities are strictly ordered since they have a regular oscillating behavior with an appropriate phase shift. This is also visible in the ionic charge densities  $\rho_{ion}(z)$  of Figs. 5.5, 5.6, 5.7, 5.8 where we notice a small ( $\sim 10^{-3} e/\text{\AA}^3$ ) and poorly-ordered fluctuation in the neutral case, contrasting with a well defined dampened oscillation in all charged case.

It is interesting to note that both in the charged and the neutral case, the atom-based charge density distributions show a structure less clearly defined than the corresponding quantity based on ionic charge-center positions. The atomistic analysis also discloses details not apparent in the ionic description, which is an averaging approach useful on mesoscopic scales, and misses important details at the local scale.

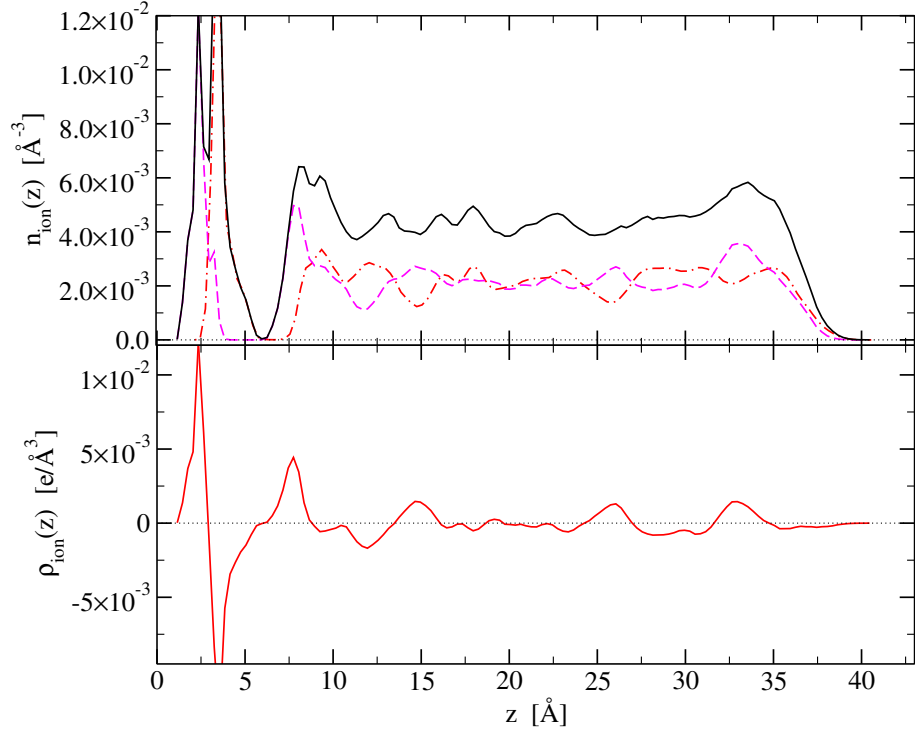


FIGURE 5.7. The ionic number and charge density profiles in the neutral case at 300 K.

For example, we notice in Figs. 5.1, 5.2, 5.3, 5.4 that in the region up to 1 nm above the muscovite surface, the atomic charge densities show more persistent oscillations than the simple dipole seen in the ionic charge densities of Figs. 5.5, 5.6, 5.7, 5.8. In all the cases studied here the atomic charge profile exhibits a four charge-layers structure of alternating charge sign. Moreover, the dominant peak and the dominant valley in the structures of the profiles are placed at  $z$ -heights similar to those of the dipole structure in the ionic charge density, but have opposite signs. This anti-phase in the two mentioned quantities can be explained in term of a particular atomic configuration close to the surface which is completely missing in the ionic description, plus the strong charge localization on few atoms of the  $[\text{Tf}_2\text{N}]$  ions as we see below.

As already said, are the cations rather than the anions which really tend to create a first solvation layer above the muscovite surface. In particular the positive hydrogen atoms of the alkane tails and of the imidazolium ring are positioned close to the surface to balance the negative charge associated to the basal oxygen atoms of the substrate. Obviously this feature is enhanced in the charged case. Since the basal oxygen atoms are placed below the K atoms which define the reference surface, these H atoms tend to penetrate the K layer and to be localized mainly in the spacings among the K atoms; this justifies non zero atomic density even down to negative values of  $z$ . These positively charged atoms, thus give rise to the first positive peak at the surface in the atomic charge profiles. Proceeding outward with  $z$ , we find the other imidazolium atoms plus the lowest anionic atoms. The remaining imidazolium atoms do not create a

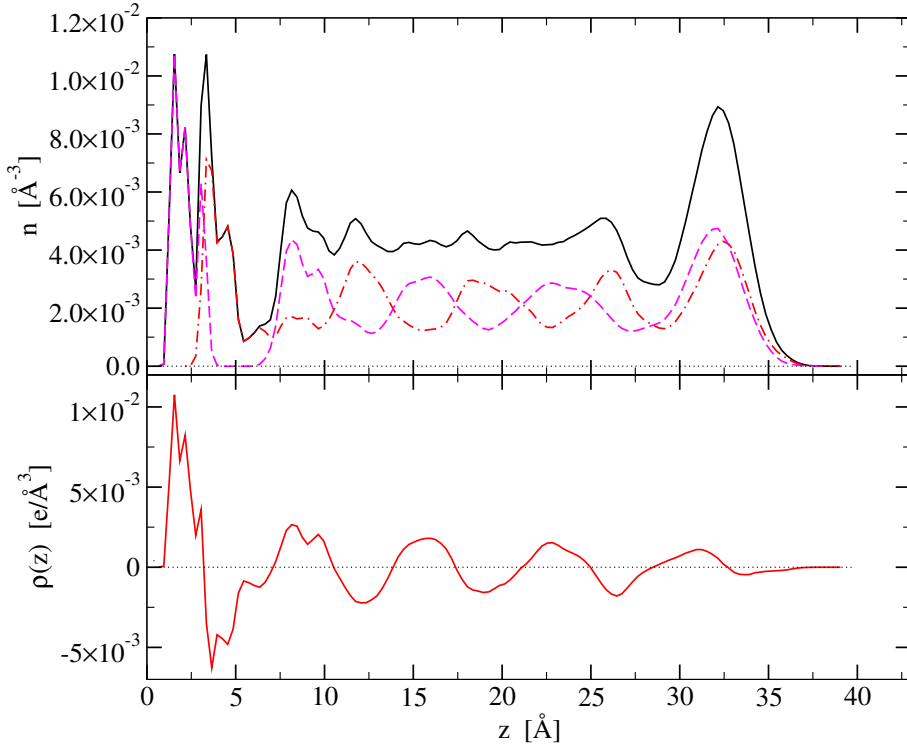


FIGURE 5.8. The ionic number and charge density profiles in the charged case at 300 K.

significantly localized net charge, but the anionic atoms can do that since their atomic partial charges are quite strong as reported in Tab. 3.2. Since it is now necessary to screen the positive K, H atoms a significant concentration of negative charge accumulate in layers. In particular we find the strongly negative O atoms which generate the first deep negative peak in the charge density (see Fig. 5.9). This negative peak is followed immediately by a high positive peak whose main contribution comes from the positively charged S atoms in the  $[\text{Tf}_2\text{N}]^-$ . As the negative nitrogen N atoms of the anions are bonded to S we find another sharp negative peak. It is now clear how this apparently simple dipole solvation layer in the ionic charge densities, is made up of a cationic layer plus a anionic layer which are not simply superimposed at different heights, but strictly entangled with the result of an effective lowering of the surface free energy and a screening of the truncated substrate.

This four-layers structure is then followed by other rapidly damped oscillations in the successive layers.

In the internal region of the film from  $\sim 1$  nm up to  $\sim 3.5$  nm we notice another significant difference between the ionic and the atomic description of the charge density. In the ionic densities an oscillation of the order of  $\sim 1e$  nm is apparent, while in the atomic case this oscillation is much weaker. As expected, with the charged substrate, the RTIL structuring is enhanced relative to the neutral case.

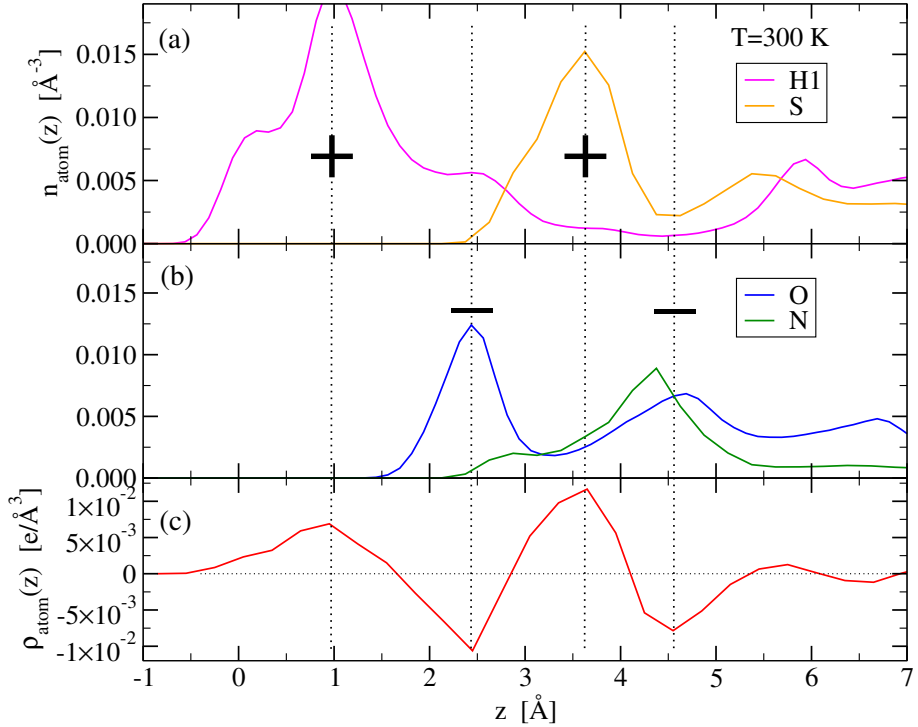


FIGURE 5.9. (a) The number density of the H1, S atoms in the charged case at 300 K up to 0.7 nm. (b) The number density of the O, N atoms in the charged case at 300 K up to 0.7 nm. (c) The atomic charge density of charged sample at 300 K. The dotted lines highlight the  $z$ -position of the positive and the negative density peaks.

**5.1.1. Free [bmim][Tf<sub>2</sub>N] surface.** It is also interesting to verify another relevant feature which has already been observed for the dialkymidazolium based RTIL [53]. Figures 5.5, 5.6, 5.7, 5.8, share a small outward shift in  $z$  of the anionic number density with respect to the cationic one at the free RTIL surface. The atomistic analysis reveals a stronger organization of the layers. Besides their center of charge, which remain lower than those of the topmost anions, the cations prefer to expose their butyl tails toward the vacuum side of the interface, while the methyl groups point toward the lower liquid side, as we can see from Fig. 5.10 (a). It is clearly visible that, on average, the carbon and nitrogen atoms of the imidazolium ring lay between the C1 carbon atoms of the methyl group and the ordered carbon atoms C1, C2, CS, CT of the longer butyl tails. As expected, in the cases under examination, the peaks of the nitrogen NA and carbon of the imidazolium ring CR, CW match well the position of the maximum of the free surface peak in the cationic density, here marked by the vertical dotted line. The atoms of the butyl group represent indeed the topmost atoms of the RTIL in the  $z$  direction, slightly above the atoms composing the anions, Fig. 5.10. This pile-up of cations can be explained with a lowering of the surface energy and increasing entropy, thus optimising the surface tension (surface free energy). Simultaneously, as we can infer from the relative symmetry of the Fig. 5.10 (b) around the dotted line

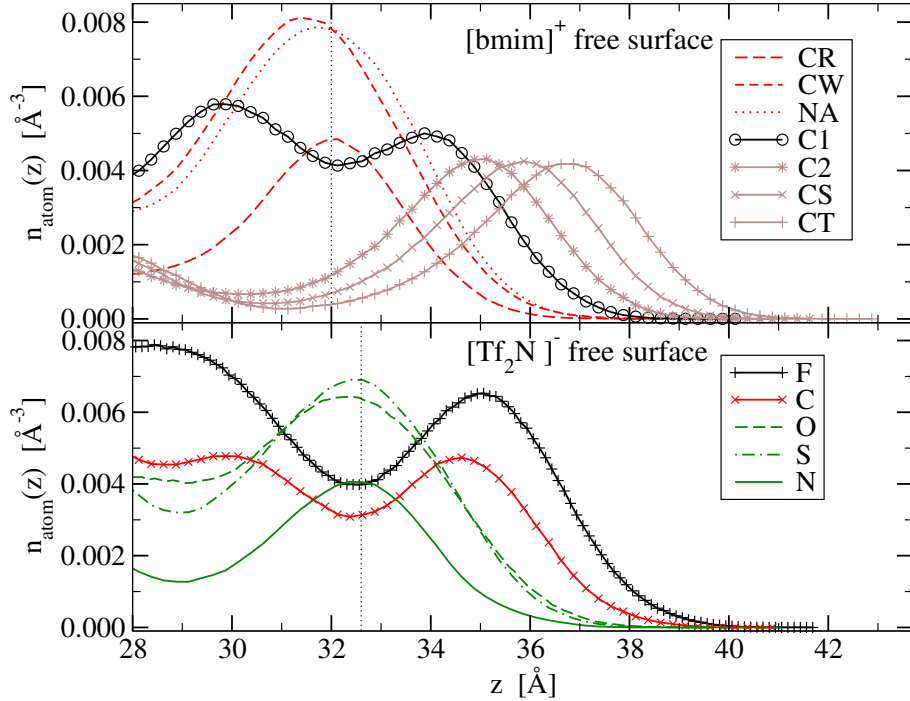


FIGURE 5.10. (a) The number density of the atoms composing the cations in the 300 K charged case at the liquid-vacuum interface. The C2, CS, CT curves indicate that the butyl tails have a marked tendency to spill out into vacuum, well beyond the the average center of charge level of the cations (vertical dotted line) (b) The number density of the anion-forming atoms in the same simulation. The dotted line represents the average center of charge position of the topmost anions.

(marking the peak anion density), the double  $\text{CF}_3$  groups of the anion are shared approximatively equally between the vacuum side and the inner side of the free surface. As expected, the peak position matches well the position of the N, S, O atoms, and, is placed at higher values of  $z$  with respect to the cation dotted line. These features are visible for both the neutral and the charged cases with relatively small differences, such as broadening, due to greater thermal fluctuations at higher  $T$ , and an increased order in the charged case.

**5.1.2. Time broadening.** The simulated time is fixed and equal to 15 ns for all the cases, since it plays an important role in the modification of the density profiles. We have seen, indeed, that a simulation time of at least  $\sim 5\text{-}6$  ns (somewhat less, at higher  $T$ ) is necessary to obtain relatively stable and reproducible density profiles. We consider a profile to be stable when, at different evolved times of a same sample and among different independent samples, its raw behavior is recognizable and the positions of its peaks and valleys remain reasonably well defined and constant. For shorter simulations, the density profiles are subject to unstable fluctuations, which are especially evident in the neutral case at  $T = 300$  K where wiggles inside the liquid film fluctuate rather

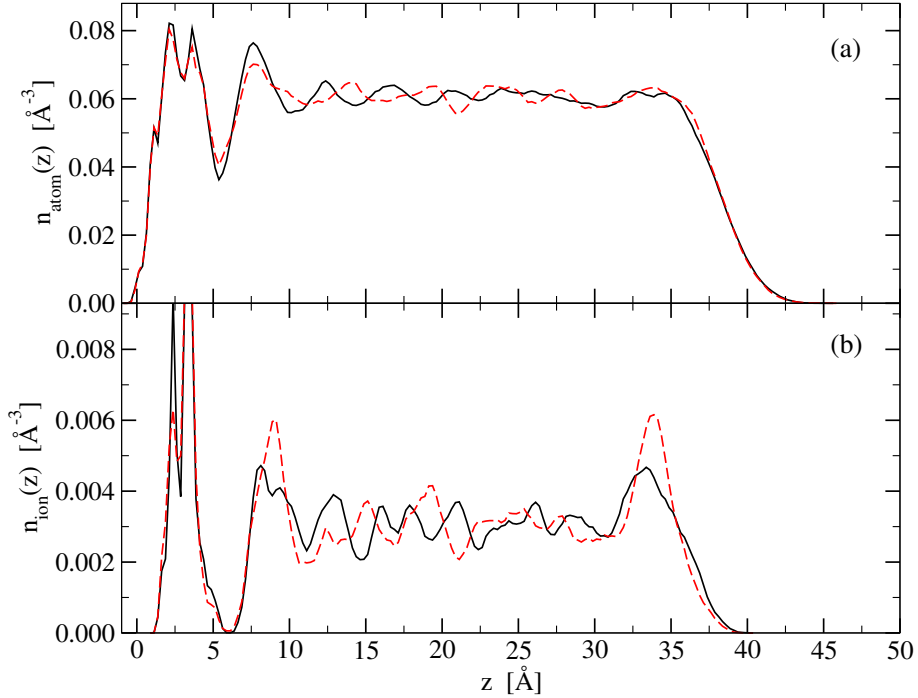


FIGURE 5.11. The number density of the atoms (a) and of the ions (b) obtained from two 2 ns long independent samples at 300 K in the neutral case.

widely, see Fig. 5.11. This particular case however deserves further analysis and might provide further insights, since it seems to be undergoing an equilibration process even during the 15 ns of the production run, pointing to very long relaxation times. This is probably due to the relatively simple annealing protocol used, covering fairly short times. All the cases studied, are subject to a smoothing and broadening process which is illustrated in Figs. 5.12, 5.13. We think that the structures surviving after 15 ns time averaging are fairly stable, and would be present with little changes if we average over longer simulations. In principle, all density structures in a real liquid film could be averaged by long-wavelength fluctuations, except that in a finite simulation box where a wavelength cut-off stabilizes the observed structures to a great extent. Our simulations seem to show evidence of this finite-amplitude structures. We analyze the density standard deviation ( $\text{std}^2$ ) in the interval  $10.5 \leq z \leq 30.5$  nm above the interface for the neutral case at 300 K and the charged case at 350 K as a function of the inverse total simulated time  $1/\Delta t$ , see Fig. 5.14.

Both figures seem to extrapolate to a non zero variance at finite  $\Delta t$ . These simulations indicate a very slow relaxation of this system. It is quite difficult to understand if we are simulating a transient phase or the actual equilibrium state. All statistical quantities (total energy, electrostatic energy, ...) do not show long-term drifts. Near the temperature region of our simulations, the considered RTIL is known to undergo a liquid-solid phase transition and in such a condition, long relaxation times are expected. We thus cannot exclude that longer simulations, or simulations starting from

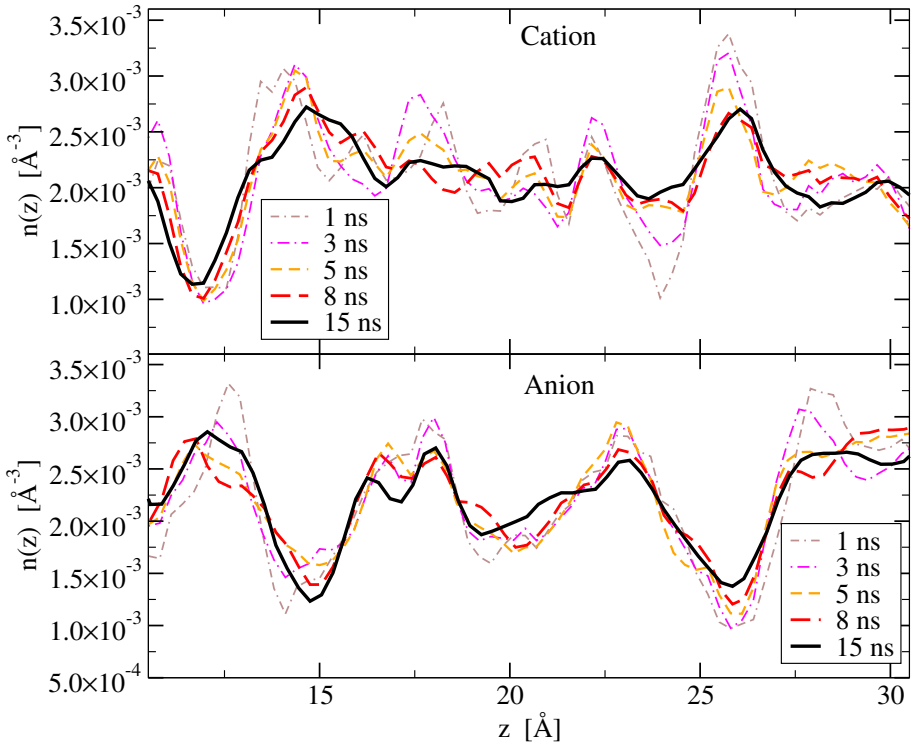


FIGURE 5.12. Progressive broadening and smoothing of the number density for cations and anions obtained with averaging over longer and longer simulations in the neutral case at 300 K.

more ordered configurations, would lead to a different degree of ordering of the RTIL film, and thus to significantly different density profiles. All we can say is that the structures of the atomic and ionic densities seem fairly stable, especially in the charged case, for times of the order of 10 ns.

## 5.2. The macroscopic Electric field

We report the  $z$ -dependency of macroscopic electric field  $E_z(z)$  generated by the average charge density  $\rho_{atom}(z)$  of the RTIL-muscovite system. As reported in Sec.4.2 it is interesting to evaluate the potential drop due to the dipole structure at the interface, and this is done by introducing the condition of a macroscopic  $z$  side for the MD box, thus to let  $D \rightarrow 0$  so that  $\phi(z)$  can take different values on the two sides of the interface. Figure 5.15 illustrates the effects of this modification of the boundary conditions.

Figures 5.16, 5.17, 5.18, 5.19 report the behavior of  $\phi(z)$  and  $E_z(z)$  generated from the neutral and charged systems which are directly visible in Figs. 5.16 and 5.17.

First of all, the strong oscillations in atomic charge densities close to the substrate surface already analyzed in Sec. 5.1 produce, as expected, corresponding successive dipole-like structures in  $\phi(z)$  and  $E_z(z)$ . The potential oscillates with an amplitude of approximately 1 V, corresponding to peak fields in the 10 V/nm range. These structures match the solvation layers found in the number densities.

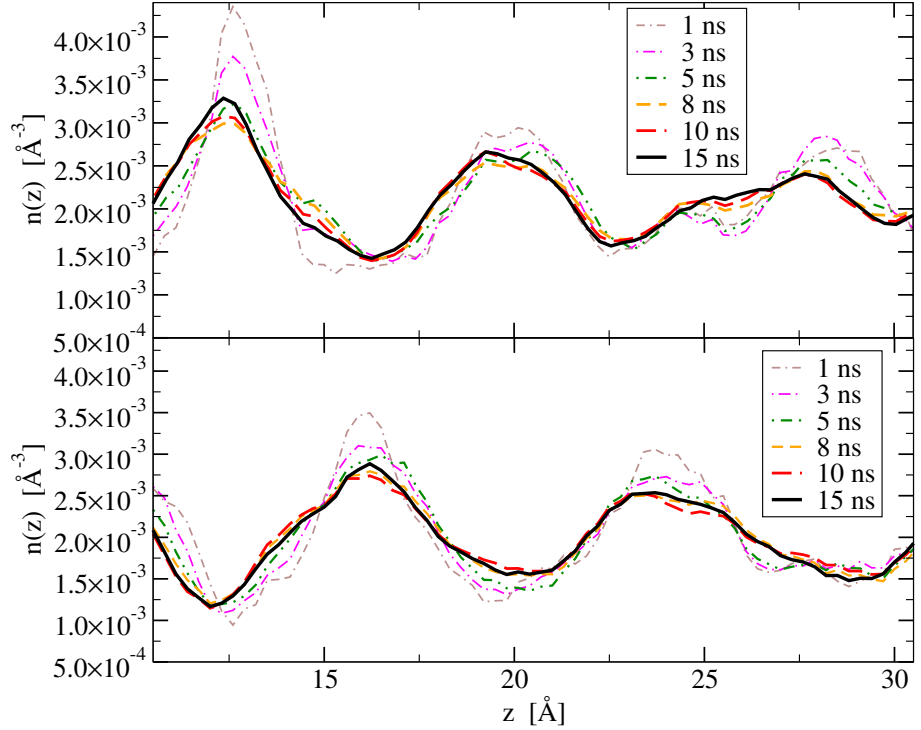


FIGURE 5.13. Progressive broadening and smoothing of the number density for cations and anions obtained with averaging over longer and longer simulations in the charged case at 350 K. Peaks and valleys are more stable than the neutral case.

In the neutral cases we can notice that in the central region of the RTIL the electric potential  $\phi(z)$  is about of 5 V, very close to its asymptotic value outside the film thus indicating that little or no dipole is present at the RTIL/vacuum interface. In this same region,  $E_z(z)$  oscillates in a range of  $\pm V/\text{nm}$  around the zero. In the charged cases in the same region of the RTIL the order of magnitude of  $\phi(z)$  is about of 6 V, and  $E_z(z)$  oscillates in the same range as the neutral case. The 300 K profiles show slightly more complex structures. Especially in the charged cases, even if the atomic and ionic charge densities seem very different, we see that the oscillating behavior of the electric potential generated from the atomic charges, clearly recalls the oscillations visible in the ionic charge densities. Indeed, we find higher potential values near the peaks of  $\rho_{ion}(z)$  and lower potential at the valleys of  $\rho_{ion}(z)$ . This fact demonstrates how, in the present work, the study of the ionic charge center distribution gives a good approximated idea of electrostatic properties in the central RTIL region. Moreover it can be considered as a good check for the self-consistency of our calculations.

### 5.3. The AFM tip nanoindentation

We come now to the main simulations of the present thesis: we insert an AFM tip, described as a rigid sphere of infinite mass and of radius  $\sigma = 1.6 \text{ nm}$  progressively descending into the RTIL film. We aim at computing the forces acting on the tip

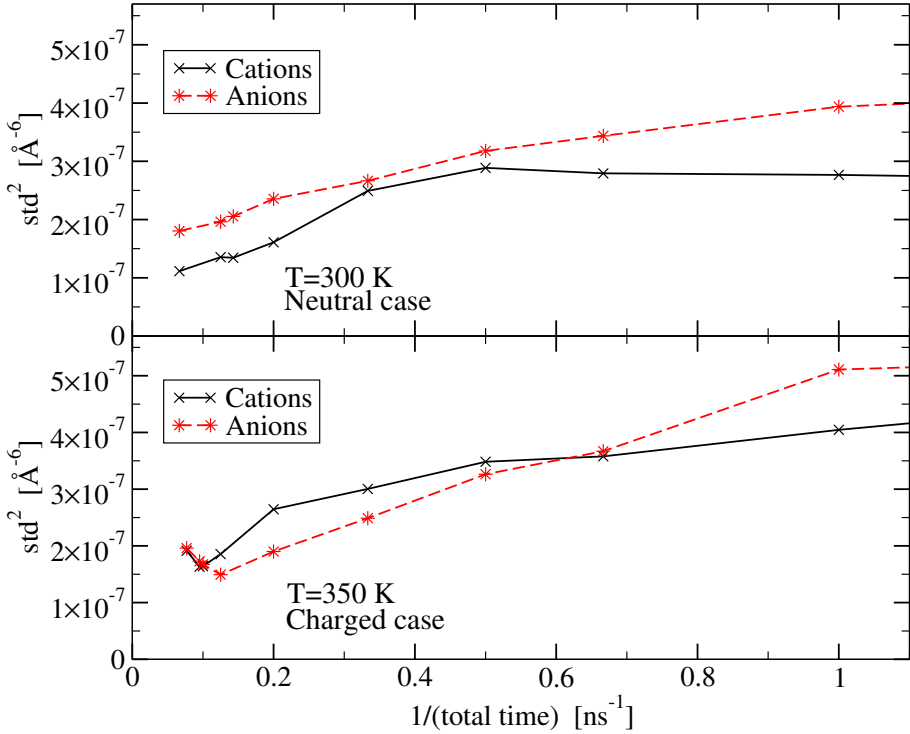


FIGURE 5.14. The squared standard deviation of the number density of cations and anion as a function of the inverse total simulation time.

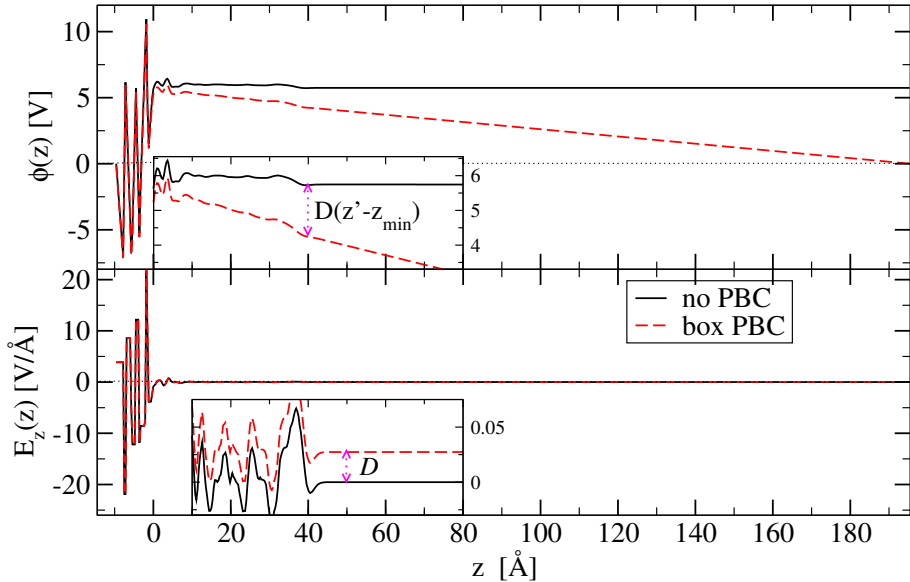


FIGURE 5.15. Effect of the removal of the  $z$ -PBC on the electric potential  $\phi(z)$  and field  $E_z(z)$  in the charged case at 350 K.

## 5. DATA PROCESSING AND ANALYSIS

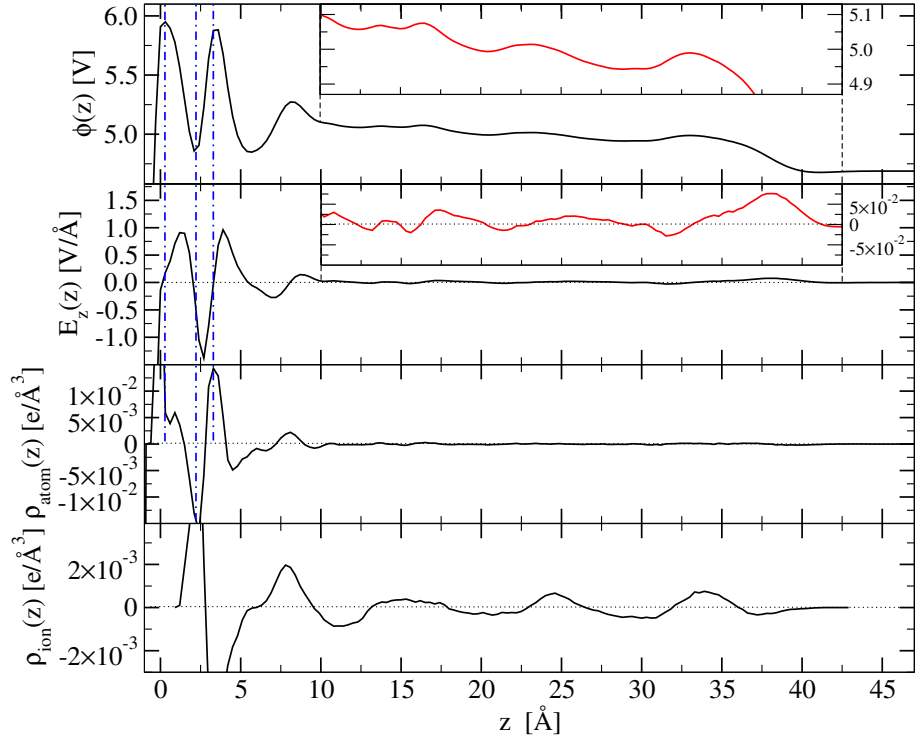


FIGURE 5.16. Comparison of the electric potential, the  $z$  component of the electric field, the atomic charge density and ionic charge density in the neutral case at 350 K.

Sample name	$T$ [K]	interfacial $K^+$ %	$v$ [mm/s]	annealing time [ns]
s_T300_K100_v250_1	300	100%	250	12
s_T300_K100_v250_2	300	100%	250	20 <sup>(a)</sup>
s_T300_K100_v250_3	300	100%	250	30
s_T300_K100_v125	300	100%	125	20 <sup>(a)</sup>
s_T350_K100_v250	350	100%	250	13
s_T300_K75_v250_1	300	75.76%	250	25 <sup>(b)</sup>
s_T300_K75_v250_2	300	75.76%	250	35 <sup>(c)</sup>
s_T300_K75_v125_1	300	75.76%	125	25 <sup>(b)</sup>
s_T300_K75_v125_2	300	75.76%	125	35 <sup>(c)</sup>
s_T350_K75_v250	350	75.76%	250	25

TABLE 5.1. All numerical simulations of the tip indentation performed at varied temperature, velocity and with a complete/reduced layer of potassium cations at the muscovite-IL interface neutral/charged. The letters in the last column connect those systems which share an identical starting configuration.

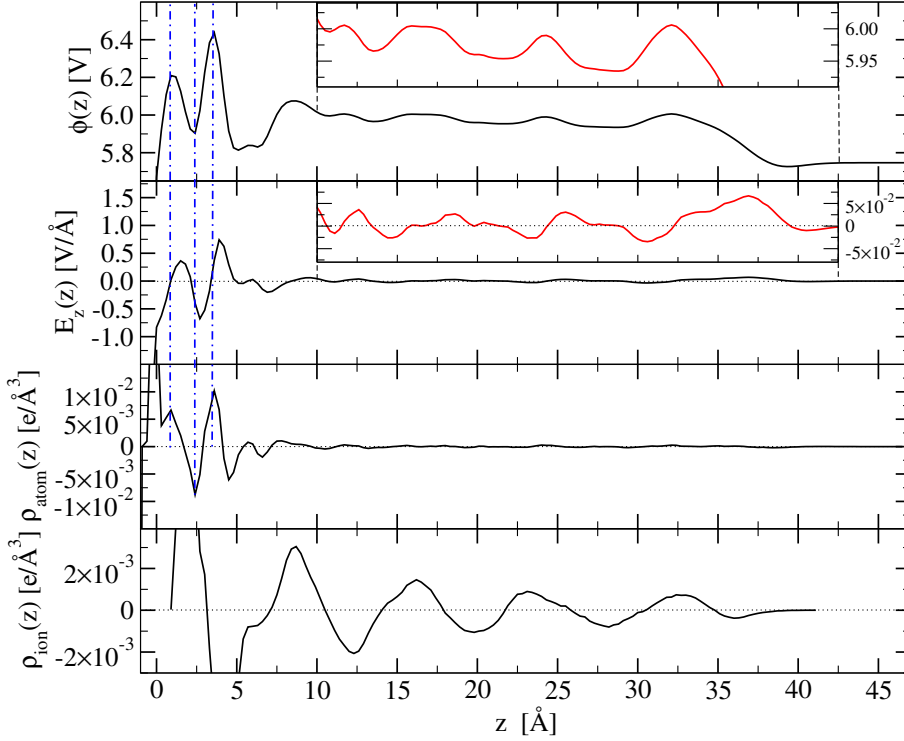


FIGURE 5.17. Like Fig. 5.16 in the charged case at 350 K.

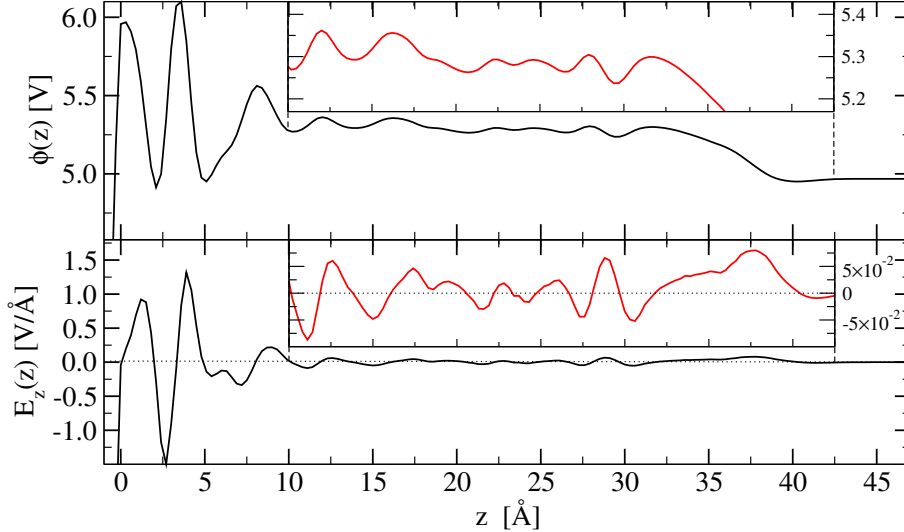


FIGURE 5.18. Comparison of the electric potential, the  $z$  component of the electric field, in the neutral case at 300 K.

itself, as produced by the molecular ions of the RTIL during this indentation process. In what follows, the position of the meso-sphere is identified by the  $z$  coordinate of its center, measured relative to the topmost K plane in the muscovite slab, as in the previous sections. Since the in-plane periodicity of the (001) muscovite surface can not

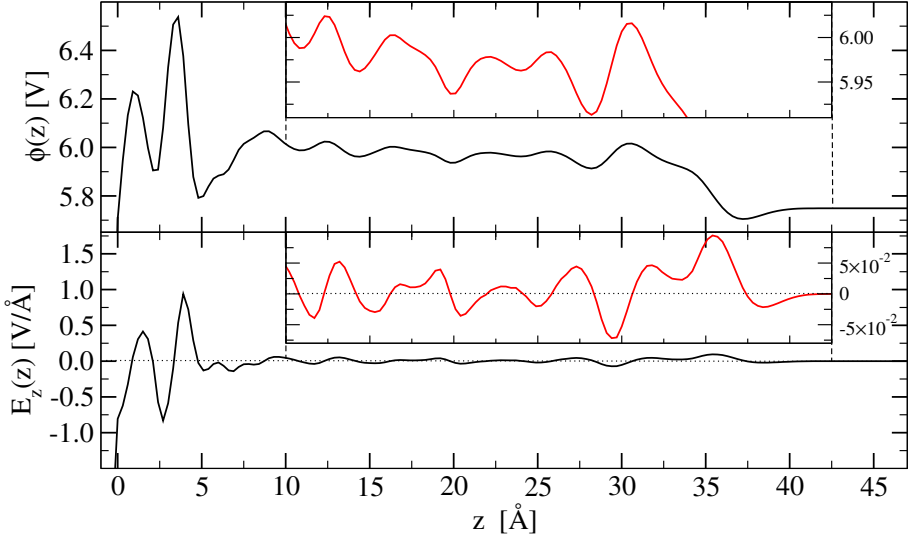


FIGURE 5.19. Like Fig. 5.18 charged case at 300 K.

be strictly considered much shorter than the tip diameter, the precise location of the contact point in the  $xy$  plane is not irrelevant, especially for short  $z$  distances. We have chosen to perform all our simulations with the  $x$ ,  $y$  coordinates of the tip center fixed at the point ( $x_c = 57.1098$ ,  $y_c = 27.0459$ ), i.e. approximately near a topmost  $K^+$ , as visible from Fig. 5.20. For reasons of time we did not explore other indentation points.

Each simulation of an indentation event starts with the tip far enough above the free RTIL surface so that the interactions are practically null. Afterwards the relative distance between the tip and the muscovite surface is progressively reduced in discontinuous steps of regular amplitude. For each trajectory, the  $16 \leq z \leq 64.5$  Å range is covered in steps 0.5 Å or 0.25 Å wide, relaxing the system at each step for 0.1 ns, and collecting statistics during the following 0.1 ns simulation. Each simulation of the film indentation covers 19.5 or 39 ns for the two steps, thus corresponding to approaching velocities of 250 mm/s and 125 mm/s, respectively. The approaching velocity plays an important role since the tip, which moves in a fluid, experiences a friction term depending on  $v$  itself [51]. Our force profiles are therefore affected by this friction contribution. The simulation requires approximatively 10 and 20 days running in parallel for the 0.5 Å and the 0.25 Å step respectively.

In addition to the two different descent velocities, we generate and study a few trajectories with two values of temperature, and different independent starting configurations. The forces  $F_x$ ,  $F_y$ ,  $F_z$  acting on the tip are evaluated as averages over time of the acquisition data simulation and, where available, over those trajectories obtained with same working conditions but different starting independent configurations. Table 5.1 summarizes the individual simulations we have done. The dependence of the forces on the distance  $z$ , is shown in Figs. (5.21, 5.22, 5.23, 5.24).

At the beginning of the nanoindentation process ( $z \geq 5.5$  nm), in all the trajectories, the vertical force  $F_z$  is attractive, with the tip being pulled down toward the liquid, as in non-contact AFM. The attractive region ends near  $z \simeq 5.5$  nm, roughly

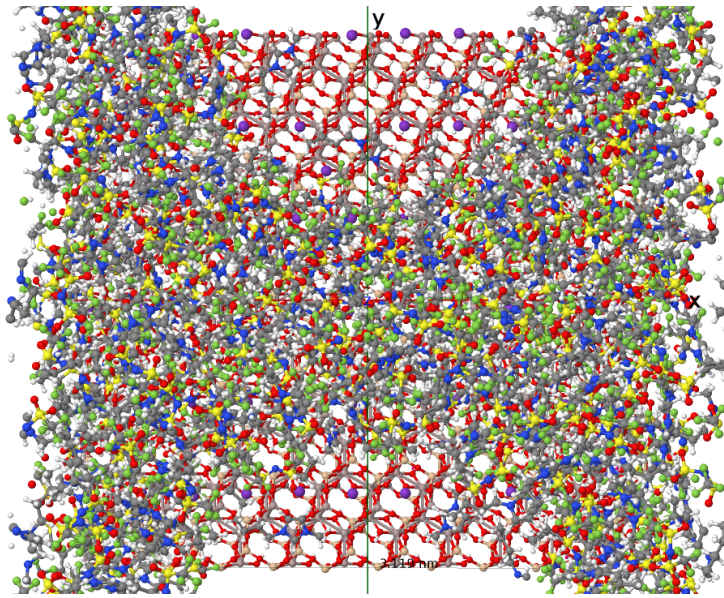


FIGURE 5.20. A snapshot of the hole produced by the tip immersed into the RTIL at the height  $z = 18 \text{ \AA}$ . The tip is recognizable from the two semi-spherical shapes centered at the opposite edges of the MD box which show the mica-substrate. The hole appears as split in two halves due to the particular center position and due to the PBCs.

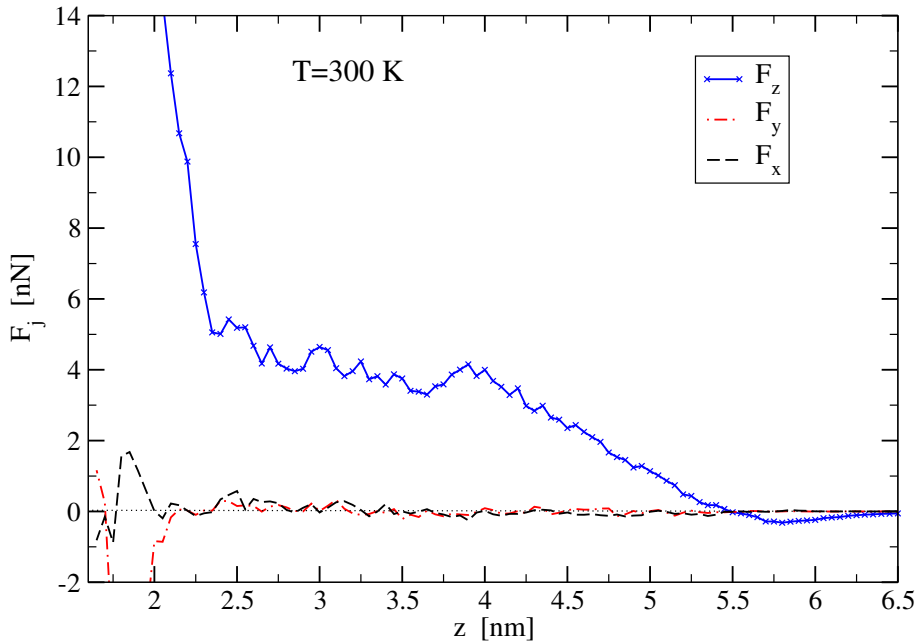


FIGURE 5.21. The  $x$ ,  $y$ ,  $z$  components of the force acting on the tip advancing at 250 nm/s, in the neutral case at 300 K (samples s\_T300\_K100\_v250\_1, s\_T300\_K100\_v250\_2, s\_T300\_K100\_v250\_3).

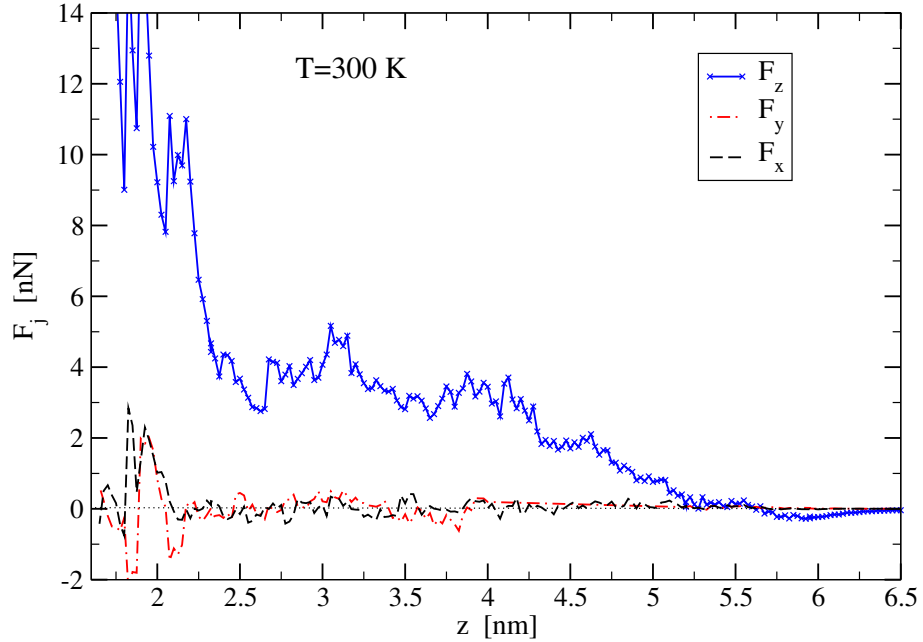


FIGURE 5.22. The  $x$ ,  $y$ ,  $z$  components of the force acting on the tip advancing at 125 mm/s, in the neutral case at 300 K (sample s\_T300\_K100\_v125).

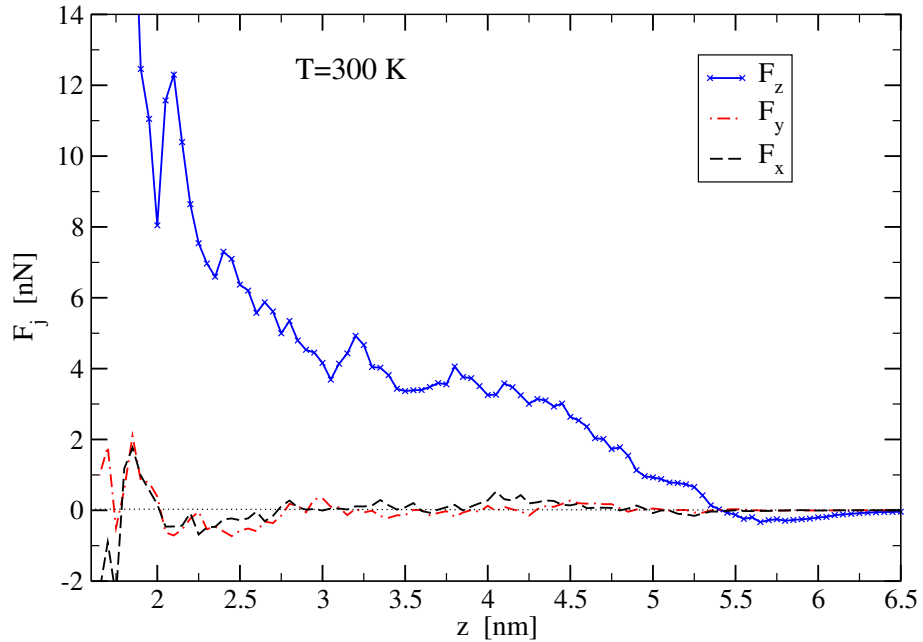


FIGURE 5.23. The  $x$ ,  $y$ ,  $z$  components of the force acting on the tip advancing at 250 mm/s, in the charged case at 300 K (samples\_T300\_K75\_v250\_1, s\_T300\_K75\_v250\_2).

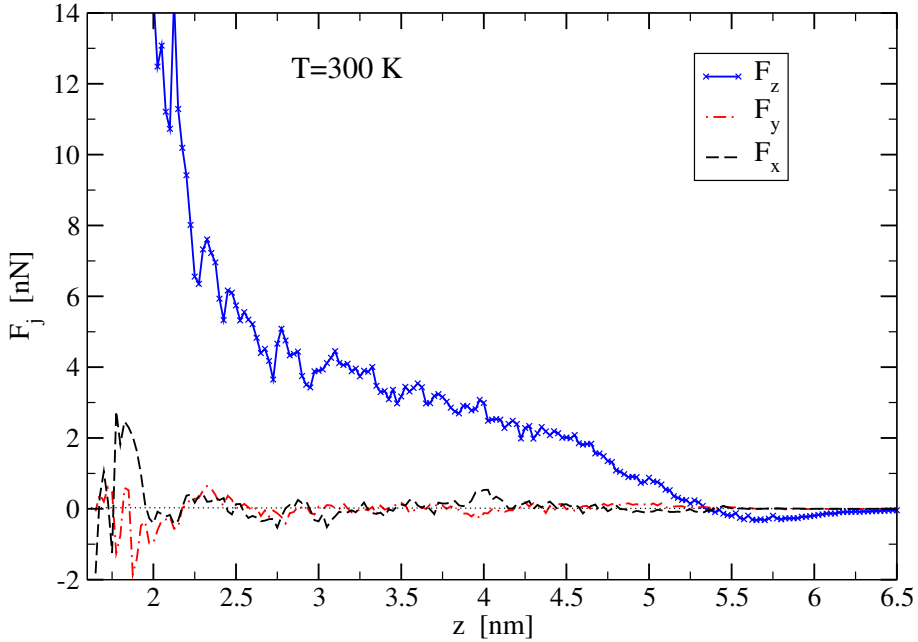


FIGURE 5.24. The  $x$ ,  $y$ ,  $z$  components of the force acting on the tip advancing at 125 mm/s, in the charged case at 300 K (samples s\_T300\_K75\_v125\_1, s\_T300\_K75\_v125\_2).

equal to the film thickness plus the sphere radius, marking the beginning of the contact regime for our simulated AFM measurement. For lower  $z$  values, while  $F_x$ , and  $F_y$  remain very close to zero on average,  $F_z$ , instead, tends to increase. This increase is however not monotonic, but displays localized irregularities, plus occasional oscillations of longer wavelength and rather small amplitude. The long-wavelength oscillations map any kind of layering in the film number density, while local irregularities are due to activated molecular displacements representing rare events on the rather short time scale of our simulations. The role of these events could be mitigated by increasing the number of independent trajectories over which  $F_z$  is averaged. Interestingly, we can notice that the case which shows the clearest long-wavelength structures is the one reported in Fig. 5.22. This profile seems to have two long-wavelength structures peaking at  $z \approx 40$  Å,  $z \approx 30$  Å plus two other peaks at smaller  $z$  values, i.e. closer to the substrate. Compared to Fig. 5.21, this trajectory has little statistical meaning, since it is obtained from a single starting configuration. This case, therefore, deserves further analysis. The indentation at the same working conditions but at a higher velocity of 250 mm/s, which is more statistical significant, shows noisier structures, see Fig. 5.21. Despite the clear nature of its equilibrium ionic structures, with respect to the neutral case (see Sec. 5.1), the charged case does not show increased organization in the  $F_z$  dependence on  $z$ , see Figs. 5.23, 5.24. Moreover, in contrast with the neutral case at 300 K, the charged case at the same temperature shows a hint of long-wavelength structures for the trajectory with a approaching velocity of 250 mm/s, while those structures are less visible in the trajectory with a descent velocity of 125 mm/s.

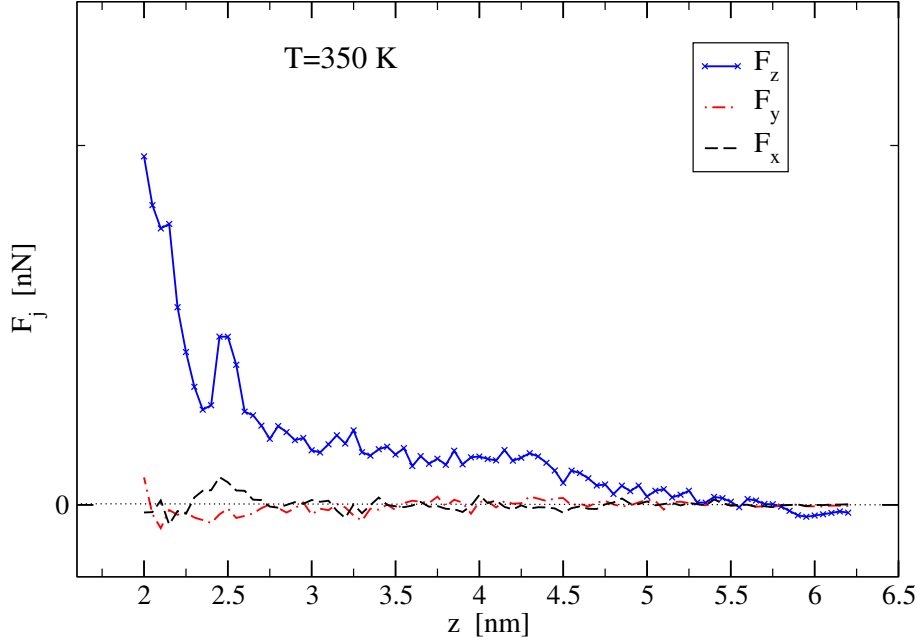


FIGURE 5.25. The  $x$ ,  $y$ ,  $z$  components of the force acting on the tip advancing at 250 mm/s, in the neutral case at 350 K (sample s\_T350\_K100\_v250).

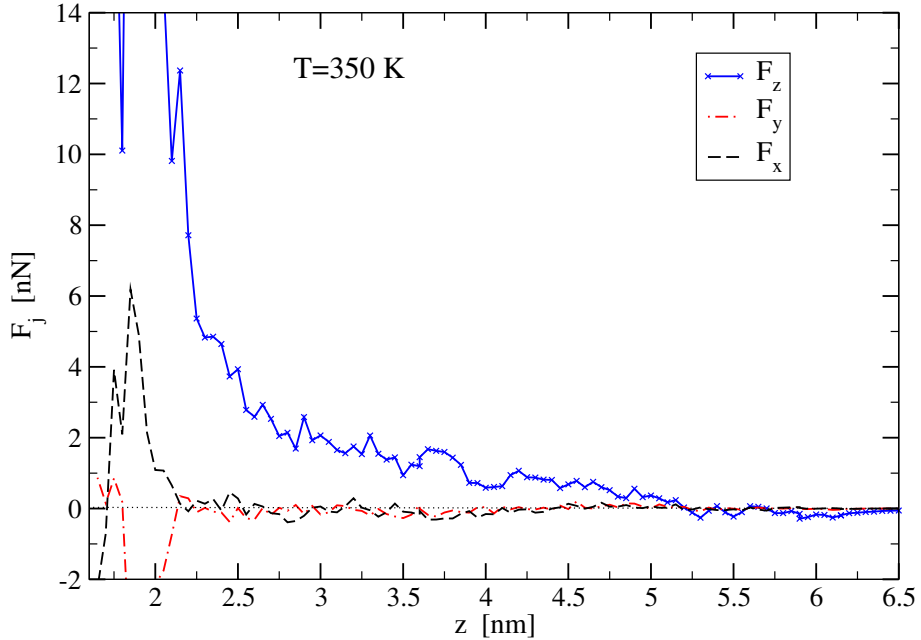


FIGURE 5.26. The  $x$ ,  $y$ ,  $z$  components of the force acting on the tip advancing at 250 mm/s, in the charged case at 350 K (sample s\_T350\_K75\_v250).

Figures (5.25, 5.26) display the outcome of simulations at  $T = 350$  K which allow us to assess, in first approximation, the effect of temperature for the neutral and charged cases. Care must be taken since each of these graphs is obtained from a single trajectory;

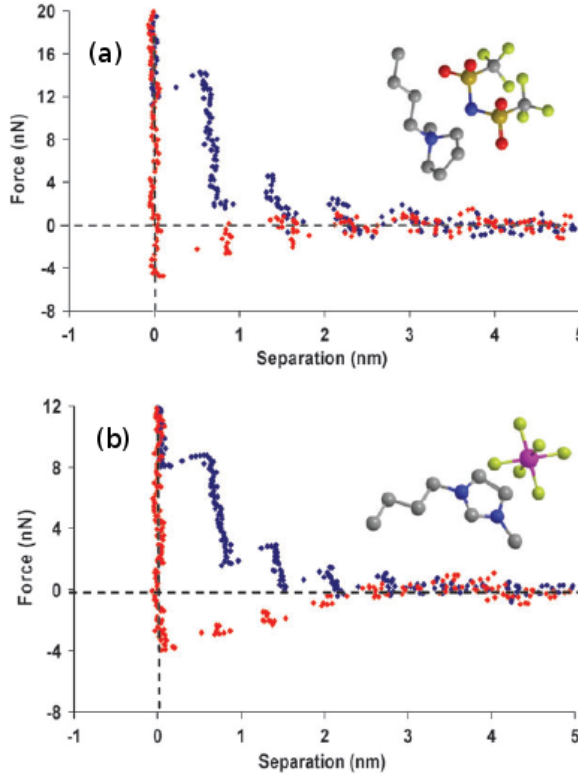


FIGURE 5.27. The experimental  $z$  force profiles acting on a real AFM tip approaching (blue) and retracting (red) from a mica surface as a function of their relative distance. (a)  $[\text{bmp}]^+[\text{Tf}_2\text{N}]^-$ , (b)  $[\text{bmim}]^+[\text{PF}_6]^-$ .

however, a comparison with the data at  $T = 300$  K at the same approach velocity shows that the film resistance to penetration decreases rapidly with increasing  $T$ .

These results show similarities with those reported in Ref. [51] for the numeric values of  $F_z$  in the neutral case at  $T = 300$  K both for an approach velocity of 250 mm/s and of 125 mm/s. Here the long-wavelength structures seem however less distinguishable.

More significant differences are visible with respect the results obtained in previous experimental work [49]. Comparison of our figures at 300 K and the measurements made for the  $[\text{bmim}]^+[\text{PF}_6]^-$ , and the  $[\text{bmp}]^+[\text{Tf}_2\text{N}]^-$  (see Fig. 5.27) on mica shows an important qualitative difference. While in the experimental data, an ordered sharp increase in the forces close to the substrate is clearly visible, in our data we have a progressive increase, more similar to the measurements obtained in the same work from a silica surface. Moreover, the sharp structures of Ref. [49] are positioned closer to the surface and decay with  $z$  more rapidly than the  $F_z$  acquired from our simulations. Due to this strong qualitative differences a quantitative comparison is quite difficult, even if the range of force is directly comparable. Even this fact is probably fortuitous, since these forces are measured on tips of significantly different radius, i.e., 1.6 nm in our simulations, and 20 nm in experiment. The pressure under the tip, therefore, is larger in simulation ( $\sim 20$  kbar) than in experiment ( $\sim 0.1$  kbar). This can be due to

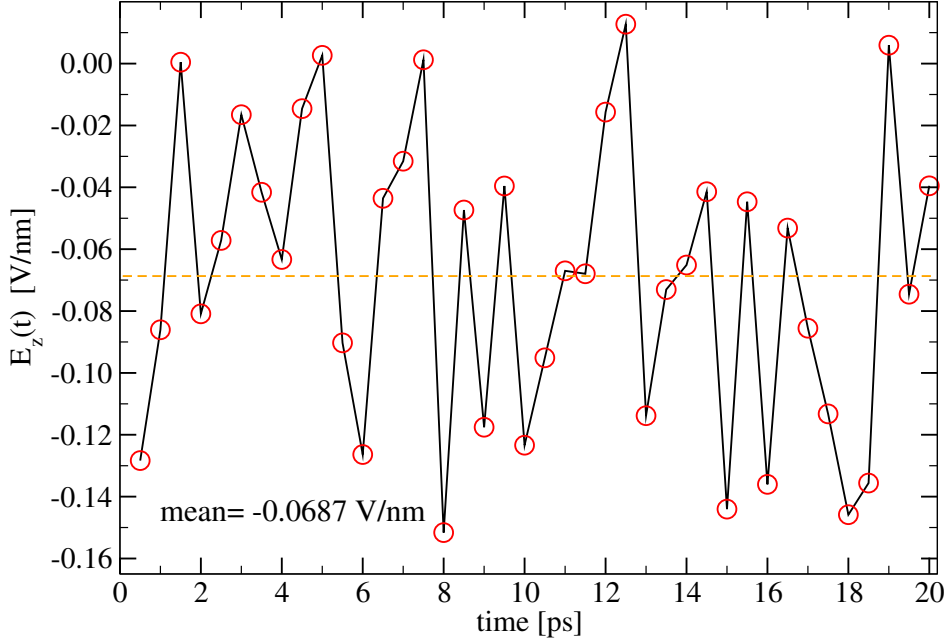


FIGURE 5.28. The time dependence of the local electrostatic field in the neutral case at 300 K evaluated at  $z = 2.75$  nm.

the several reasons, such as the different ionic liquids considered, the different thickness of the RTIL film (which in the experimental case is a thicker more bulk-like film), the neglected bulk elasticity of the muscovite substrate (in simulations only the first atomic layers are free to move), and a different quality and purity of the muscovite substrate, including  $\text{K}^+ - \text{OH}_3^+$  substitutions or water solvation. The main reason for the large computed forces is to be attributed to the very low mobility of the ions, which affects our simulations at  $T = 300$  K and do not allow an appropriate equilibration on the rather short time scale of the force data acquisition. Our simulated RTIL is extremely viscous, significantly more than its real counterpart. Accordingly, the tip finds large viscous forces binding its motion.

#### 5.4. Local Electric field

In Sec. 5.2 we have analyzed the macroscopic electric potential and field at equilibrium. These fields would be significantly perturbed by the introduction of the tip-sphere. If the tip was electrically charged, such fields would act on it, thus producing additional force components, which could in principle even exceed the wall-potential forces of Sec. 3.3.5.

We compute the local electric field at the center of the tip, where one could assume that the tip charge would be positioned, with the protocol described in Sec. 4.3. The local electric field strongly depends on the atomic displacements and on detailed configurational variations; this is visible from the strong and rapid time fluctuations reported in Figs. 5.28, 5.29 for the neutral and charged cases. For this reason, the local electric field is averaged over all available configurations for each fixed position of

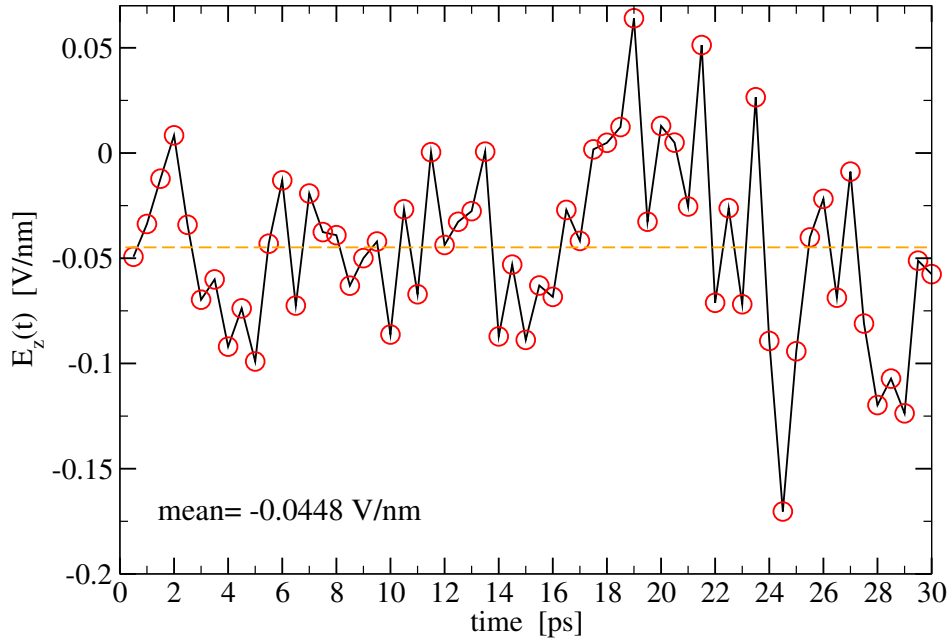


FIGURE 5.29. Same as Fig. 5.28, but for the charged substrate.

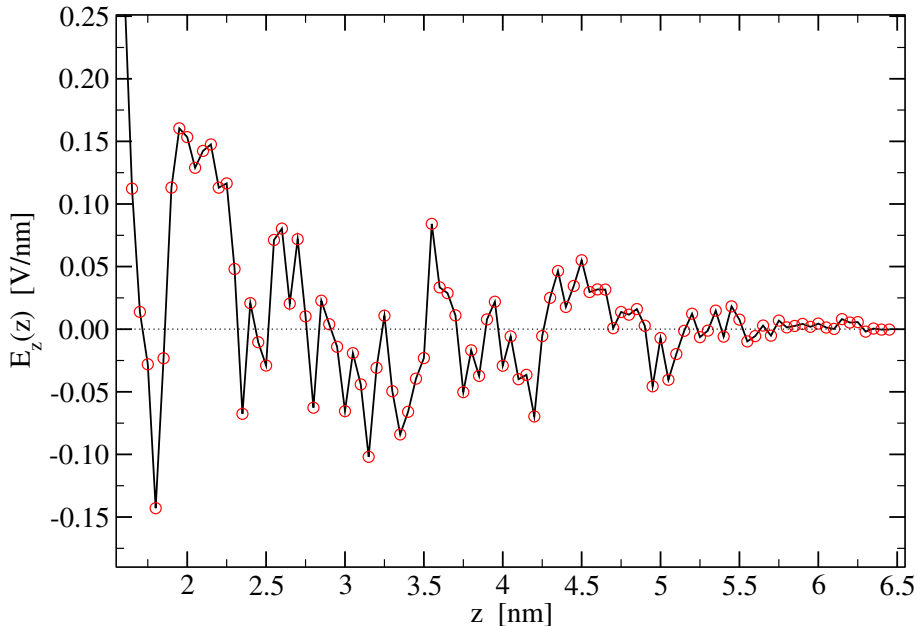


FIGURE 5.30. The local  $z$  dependence of the electrostatic field at the center of the descending spherical tip in the charged case at  $T=300$  K and approach velocity of 250 mm/s (sample s\_T300\_K75\_v250\_1).

the tip center. This consists in an averaging process over the same 50 configurations (100 ps with a time-step of 2 ps) used for the  $F_z$  analysis.

Figure 5.30 reports the  $z$  dependence of the local field  $E_z$  evaluated at the tip center during the indentation process for the charged case, at  $T=300$  K, and approach

velocity of 250 mm/s.  $E_z$  is rather small when the tip is well outside the liquid, while inside it displays both localized irregular jumps and relatively longer-wavelength oscillations. The longer wavelength oscillations might reflect a degree of ionic charge layering in the film. Five peak and five valley structures can be recognized even though with strong irregularities. A direct comparison with the macroscopic field is very difficult since the presence of the tip in the film heavily modifies the equilibrium structures observed in Sec. 5.1. Despite this, we can recognize a first positive long wavelength structure around  $z \simeq 46$  Å which, can be put in relation with the first positive ionic charge density peak near the free RTIL surface. In this region, indeed, the density structures are still not strongly modified since the tip is only touching the film surface.

The irregular jumps, instead, could be related again to the activated molecular displacements representing rare events on the short time scale of our simulations. These displacements are induced by the discrete downward steps of the tip. Moreover, these displacements can create a local charge unbalance or, more in general, quite strong configurational modifications near the tip, which would require relatively long equilibration time with respect to the one used in our simulations. For these reasons, it is possible that for two subsequent  $z$  heights of the tip, the strong differences in local configurations of the charges near the tip generates these jump-irregularities in  $E_z$ . However, this is only a hypothesis which would deserve further insights.

The computed values of the field in Fig. 5.30 show that the electrostatic contribution to the total force acting on a charged tip with the simple configuration adopted in the present work, can be neglected unless the charge  $q$  on the tip exceeds several hundred elementary charges  $e$ . At such a level of charging the perturbative approach of neglecting the effect of the tip field on the moving ions would of course make little sense.

## CHAPTER 6

### Discussion and Conclusion

In the present work we investigate the interfacial organization of a  $[bmim]^+$   $[\text{Tf}_2\text{N}]^-$  film  $\sim 4$  nm thick deposited onto a bulk-terminated (001) mica-surface. We represent this film with a repeated super-cell of  $xy$ -area  $5.7 \times 5.41$  nm $^2$  within a classical MD framework by means of an NVT ensemble obtained by means of Nosé-Hoover thermostat. For the mica substrate, we have considered two different numbers of surface K $^+$  cations, representing a neutral substrate and a charged one, with approximately 0.5 e/nm $^2$ . The charge unbalance is compensated by varying the number of RTIL anions, in order to deal with globally neutral systems. A detailed analysis of the atomic and ionic number densities of RTIL has been carried out at temperatures of  $T = 350$  K and  $T = 300$  K.

The main difficulty encountered in the simulation was reaching a time scale sufficiently long to allow a good equilibration of the system in each of the cases analyzed. The annealing procedure used in the “charged” case turned out as more efficient than in the “neutral” case, where space and time-dependence of the average number density profiles of atoms and ions at  $T = 300$  K probably indicates a slow transient condition toward equilibrium. The 15 ns of production runs do not allow us to extract reliable informations about equilibration within much longer time scale. We indeed cannot exclude the presence of a long-term drift undetectable by our statistical analysis. For these reasons, even after few tens of ns simulation, doubts remain about the real equilibrium nature of the samples studied and, therefore, about the correct identification of the thermodynamic state of the RTIL thin film. It is quite possible that a slow ordering process is taking place, which would lead to some degree of order in the actual equilibrium state. This “solidification” process would however proceed extremely slowly, due to the high viscosity of the simulated RTIL at 300 K, leading to a substantially glassy state.

Despite these doubts, after 15 ns of data acquisition, the number densities show a stable adsorbed double ionic layer close to the mica surface followed by a weak layering whose amplitude decreases quickly moving away from the substrate. The charge on the substrate of the “charged” case tends to promote ionic charge oscillations which, however, do not result in a particularly structured total number ionic density. This is due to a mutual cancellation of out-of-phase oscillations of the anion and cation number density profiles. Low temperatures tend to promote structuring, but no sharp peaks characteristic of a well ordered layering such as in Fig.5 of Ref. [54] are visible at  $T = 300$  K, neither for the neutral nor for charged substrate. A comparison with the neutral case at  $T = 300$  K is however prevented by the probable lack of an appropriate relaxation of our sample.

In addition to the analysis of the equilibrium properties, we have investigated the force profiles experienced by an AFM probing tip thus to make a direct comparison between theory and experiment. Strong qualitative differences, and quite important quantitative differences, are observed with respect to the experimental force profiles of Fig. 5.27 obtained from Ref. [49], where discrete sharp profiles for  $F_z$  are reported for  $[\text{bmp}]^+[\text{Tf}_2\text{N}]^-$  and  $[\text{bmim}]^+[\text{PF}_6]^-$  on mica surface. Despite the quantitative differences, it is interesting to notice that the order of magnitude obtained for  $F_z$  in the two works is comparable. This is however not meaningful since it corresponds to a difference in pressure under the tip of about two orders of magnitude, because of the differences in tip size. Firstly, these differences can be attributed to different RTILs and different configurations used. The authors of Ref. [49] have carried out their measurements with an actual AFM tip whose radius of curvature is approximatively one order of magnitude larger than our own. Moreover, in experiment films are thick, and the tip remains completely immersed in the RTIL film. We have instead penetrated the nanometric film with an idealized sharper tip starting well outside the free surface. The differences could be attributed also to the high approach velocity (250–125 mm/s), and the lack of an appropriate relaxation to equilibrium in simulation. At such high speed viscous effects become important, especially since the simulated RTIL is particularly viscous and glass-like. Also local heating effects in the penetration region are rapidly suppressed by the Nosé-Hoover thermostat ( $\tau_T$  of Sec. 3.2.2 here fixed at 0.1 ps), possibly faster than occur in reality.

Finally, our calculation rules out important effect of the ionic charges in the RTIL, unless a huge charge accumulates on the tip itself.

Possible further lines of investigation include: (i) simulations carried out with different RTILs, in particular those used in experiments. (ii) a starting configuration derived from the solid state of the appropriate RTIL, for which the experimental structure may be available. (iii) a systematic investigation of the tip-size dependency of the friction force experienced by the AFM tip as it advances at fixed speed inside a liquid, down to the nanometric size.

### 6.1. Acknowledgment

This work has been supported by Regione Lombardia and CILEA Consortium through a LISA Initiative (Laboratory for Interdisciplinary Advanced Simulation) 2010 grant <http://lisa.cilea.it>.

## APPENDIX A

### Computer and parallel implementation

We have performed our simulations using the software DL-POLY ver. 2.20 from Daresbury laboratories [43]. We have run our calculations on the dedicated Lagrange cluster-machines available on LISAs project at CILEA in Segrate-MI [55], a 336 node cluster, each node composed of twin 4-core X5460 at 3.16 GHz or X5660 6-core at 2.80 GHz CPUs with Intel(R) Xeon(R) processors. Each node is equipped with at least 16 GB of RAM. Before starting with real simulations we have tested the system and the parallel implementation through a scaling analysis. Scaling test consists in choosing the best region of the number of available CPUs which we have to use during a single parallel simulation, to improve the velocity and optimize our total available simulation-time. This analysis, and the choice of the best CPUs number, can be done by comparing the informations coming from the minimization processes of the effective wall time and the total CPU time of a set repetitions of the same simulation performed with a different number of CPUs. The effective wall time consists in the actual time elapsed from start to end of a single simulation. The total time consists in the product of the effective time times the number of processors used in a same simulation.

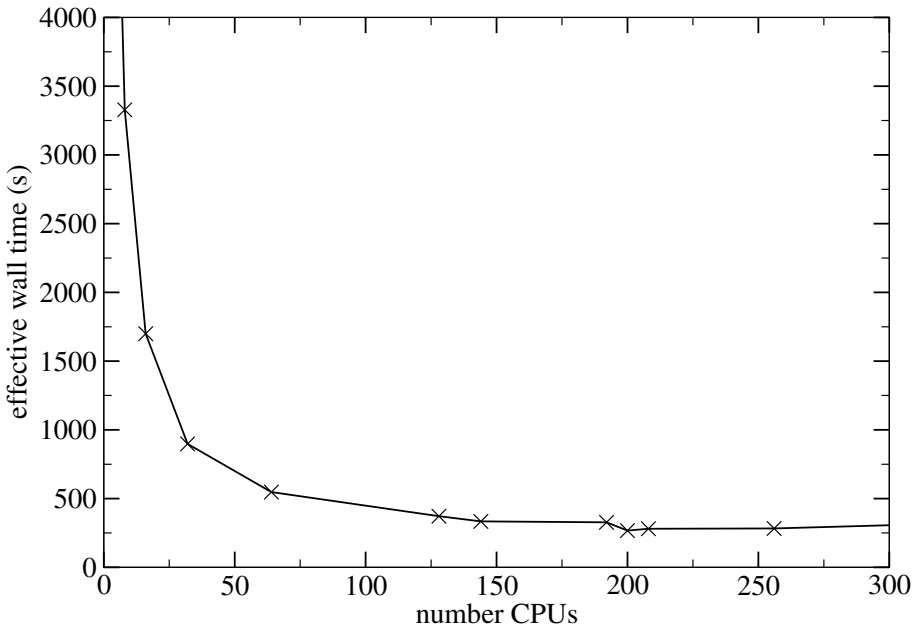


FIGURE A.1. Effective wall time as a function of the number of CPUs. The test simulation refers to 10 ps time calculation (with a time-step of 1 fs) of a RTIL relaxation onto a muscovite substrate.

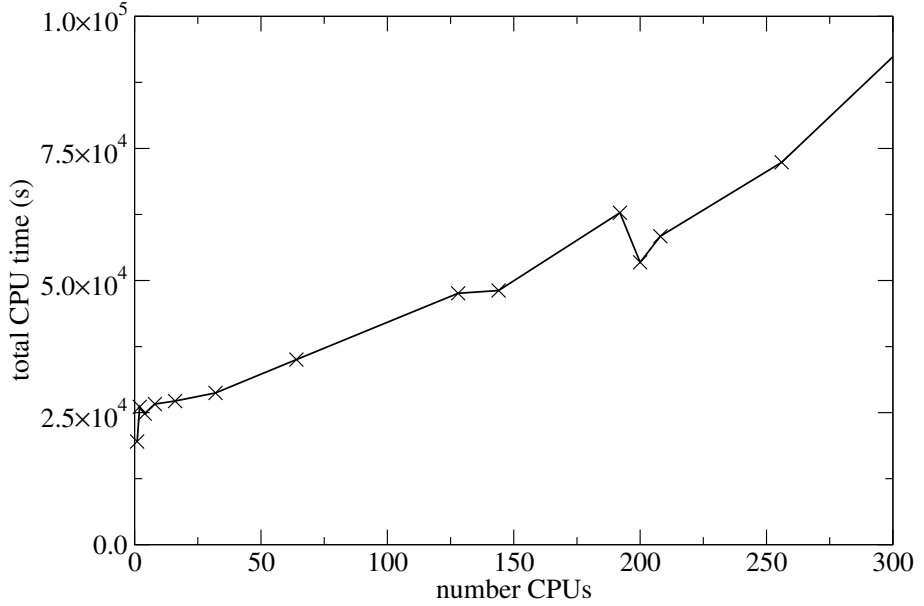


FIGURE A.2. Total time as a function of the number of CPUs. Same simulation as in Fig. A.1

We report the effective wall time and the total simulation time for a given test simulation in Figs. A.1 and A.2. It is convenient to reduce the total simulation time when performing a single simulation or a set of sequential simulations (such as the initial thermalization of our RTIL film), even though a certain amount of time is wasted in inter-node communication. It is instead better to optimize the total CPU time when performing a set of different simulations in parallel. By considering the times of Fig. A.1 and A.2, we have decided to adopt 128 CPUs for initial serial simulations such as thermalization, and 42 or 64 CPUs for most other parallel computations in order to optimize our filling of the computer and to make the most efficient use of our CPU-time budget of 315,000 h. Eventually we exceeded our budget and consumed a total 441,282 h, approximately 50 years.

## Bibliography

- [1] A. Bösmann, L. Datsevich, A. Jess, A. Lauter, C. Schmitz, and P. Wesserscheid, *Chem. Commun.*, 2494 (2001).
- [2] J. D. Holbray, I. López-Martin, G. Rothenberg, K. R. Seddon, G. Silvero, and X. Zheng, *Green Chem.* **10**, 87 (2008).
- [3] J. L. Anthony, E. J. Maginn, and J. F. Brennecke, *J. Phys. Chem. B* **106**, 7315 (2002).
- [4] S. G. Cull, J. D. Holbrey, V. Vargas-Mora, K. R. Seddon, and G. J. Lye, *Biotechnology and Bioengineering* **69**, 227 (2000).
- [5] S. Zein El Abedin, E. M. Moustafa, R. Hempelmann, H. Natter, and F. Endres *ChemPhysChem* **7**, 1534 (2006).
- [6] W. M. Liu , C. F. Ye, Q. Y. Gong, H. Z. Wang, and P. Wang, *Tribol. Lett.* **13**, 81 (2002).
- [7] J. J. Nainaparampil, K. C. Eapen, J. H. Sanders, and A. A. Voevodin, *J. Microelectromech. Syst.* **16**, 836 (2007).
- [8] C. Ye, W. Liu, Y. Chen and L. Yu, *Chem. Commun.* 2244 (2001).
- [9] E. Frackowiak, *J. Braz. Chem. Soc.* **17**, 1074 (2006).
- [10] A. Balducci, F. Soavi, M. Mastragostino, *Appl. Phys. A* **82**, 627 (2006).
- [11] V. L. Pushparaj, M. M. Shaijumon, A. Kumar, S. Murugesan, L. Ci, R. Vajtai, R. J. Linhardt, O. Nalamasu, and P. M. Ajayan, *Proc. Natl. Acad. Sci. USA* **104**, 13574 (2007).
- [12] M. Freemantle, *Chem. Eng. News* **81**, 9 (2003).
- [13] T. Welton, *Chem. Rev.* **99**, 2071 (1999).
- [14] B. Jastorff, R. Störmann, J. Ranke, K. Möller, F. Stock, B. Oberheitmann, W. Hoffmann, J. Hoffmann, M. Nüchter, B. Ondruschka, and J. Filser, *Green Chem.* **5**, 136 (2003).
- [15] T. Welton, *Green. Chem.* **10**, 483 (2008).
- [16] K. R. Seddon, *Kinet. Catal* **37**, 639 (1996).
- [17] R. A. Sheldon, R. M. Lau, M. J. Sorgedrager, F. van Rantwijk, and K. R. Seddon, *Green Chem.* **4**, 147 (2002).
- [18] R. A. Sheldon, *Chem. Commun.* , 2399 (2001).
- [19] V. I. Pârvulescu and C. Hardacre, *Chem. Rev.* **107**, 2615 (2007).
- [20] M. Gräetzel, *J. Photochem. Photobiol. C* **4**, 145 (2003).
- [21] M. Gräetzel, *Nature* **414**, 338 (2001).
- [22] J. D. Holbrey and K. R. Seddon, *Clean Products and Processes* **1**, 223 (1999).
- [23] K. R. Seddon, *J. Chem. Tech. Biotechnol.* **68**, 351 (1997).
- [24] G. Fitzwater, W. Geissler, R. Moulton, N. V. Plechkova, A. Robertson, K. R. Seddon, J. Swindall, and K. Wan Joo, *Ionic Liquids: Sources of Innovation*, Report Q002, January 2005, QUILL, Belfast. <http://quill.qub.ac.uk/sources>.
- [25] A. F. Kapustinskii, *Quart. Rev.* **10**, 283 (1956).
- [26] R. J. Gale, B. Gilbert, and R. A. Osteryoung, *Inorg. Chem.* **17**, 2728 (1978).
- [27] J. Robinson and R. A. Osteryoung, *J. Am. Chem. Soc.* **101**, 323 (1979).
- [28] J. S. Wilkes, J. A. Levinsky, R. A. Wilson, and C. L. Hussey *Inorg. Chem.* **21**, 1263 (1982).
- [29] J. R. Sanders, E. H. Ward, and C. L. Hussey, *J. Electrochem. Soc.* **133**, 325 (1986).
- [30] C. L. Hussey, *Pure Appl. Chem.* **60**, 1763 (1988).
- [31] J. N. Canongia Lopes, J. Deschamps and A. A. H. Pádua, *J. Phys. Chem. B* **108**, 2038 (2004).
- [32] T. R. Allington, *Method of making a thick-film hybrid circuit*, United states patent 3,669,733 (1972).

- [33] M. E. Fleet, *Sheet silicates: micas, Volume 3A* (Alden Press, Oxford, 2003).
- [34] Bilbao crystallographic server <http://www.cryst.ehu.es/>.
- [35] M. Odelius, M. Bernasconi, and M. Parrinello, *Phys. Rev. Lett.* **78**, 2855 (1997).
- [36] R. Atkin and G. G. Warr, *J. Phys. Chem.* **111**, 5162 (2007).
- [37] N. W. Ashcroft and N. D. Mermin, *Solid state Physics* (Thomson Learning, 1976).
- [38] F. Ercolessi, *A molecular dynamic primer*, Trieste (1997), <http://www.sissa.it/furio/>.
- [39] M. P. Allen and D. J. Tildesley, *Computer simulation of liquids* (Clarendon Press, Oxford, 1987).
- [40] R. P. Feynman, R. B. Leighton and M. Sands, *The Feynman Lectures on Physics*, Vol. 1 (Addison-Wesley, 1963, Chapter 9).
- [41] Daan Frenkel and Berend Smit, *Understanding molecular simulation: from algorithms to applications* (Academic Press, San Diego, 1996).
- [42] L. Verlet, *Phys. Rev.* **159**, 98 (1967); *Phys. Rev.* **165**, 201 (1967).
- [43] W. Smith, T. R. Forester and I. T. Torodov, *The DL\_POLY\_2 User Manual*, Version 2.20 (Daresbury Labs., Warrington, UK, 2009).
- [44] W. G. Hoover, *Phys. Rev. A* **31**, 1695 (1985).
- [45] D. Nicholson and N. G. Parsonage, *Computer simulation and the Statistical Mechanics of Adsorption* (Academic Press, New York, 1982).
- [46] J. N. Canongia Lopes and A. A. H. Pádua, *J. Phys. Chem. B* **110**, 3330 (2006).
- [47] W. L. Jorgensen, D. S. Maxwell, and J. Tirado-Rives, *J. Am. Chem. Soc.* **118**, 11225 (1996).
- [48] R. T. Cygan, Jian-Jie Liang, and A. G. Kalinichev, *Phys. Chem. B* **108**, 1255 (2004).
- [49] R. Hayes, G. G. Warr, and R. Atkin, *Phys. Chem. Chem. Phys.* **12**, 1709 (2010).
- [50] S. Bovio, A. Podestà, C. Lenardi, and P. Milani, *J. Phys. Chem. B* **113**, 6600 (2009).
- [51] P. Ballone, M. G. Del Pópolo, S. Bovio, A. Podestà, P. Milani, and N. Manini, arXiv/1101.5424.
- [52] M. Cesaratto, *Molecular-Dynamics simulations of adsorbed ionic-liquid films*. Diploma thesis “Tesi di laurea magistrale in fisica”. Advisor: N. Manini, Co-advisors: G. Onida, M. G. Del Pópolo (Università degli Studi di Milano 2008).
- [53] R. M. Lynden-Bell and M. G. Del Pópolo, *Phys. Chem. Chem. Phys.* **8**, 949 (2006).
- [54] S. Bovio, A. Podestà, P. Milani, P. Ballone and M. G. Del Pópolo *J. Phys.: Condens. Matter* **21**, 424118 (2009).
- [55] Cilea supercomputing center, Segrate, Italy <http://www.cilea.it/>.